9-12-2014

Spectroscopic Studies of Conjugated Polymer Nanostructures and Polymer/Acceptor Blends

Jian Gao

Jian Gao
Candidate

Department of Chemistry and Chemical Biology
Department

This dissertation is approved, and it is acceptable in quality and form for publication:

Approved by the Dissertation Committee:

Dr. John K. Grey Chairperson

Dr. Yang Qin

Dr. Terefe Habteyes

Dr. David Dunlap

Spectroscopic Studies of Conjugated Polymer Nanostructures and Polymer/Acceptor Blends

By

Jian Gao

B.S., Chemistry

Shandong University, P. R. China, 2009

DISSERTATION Submitted in Partial Fulfillment of the

Requirements for the Degree of

Doctor of Philosophy

Chemistry

The University of New Mexico

Albuquerque, New Mexico

July, 2014

DEDICATION

To my deeply beloved family, my parents, my elder sister, my brother-in-law, my niece, who stood by with me and helped me to get through hard times. Without the support and encouragement, I would have been lost and had no chance to present this work.

ACKNOWLEDGMENTS

First, I want to give my deep appreciation and gratitude to my advisor, Professor John K. Grey. He is smart, very knowledgeable, enthusiastic and has great passion for science. Without his continuous encouragement and helpful advising, I cannot realize my strength and find confidence to move my research forward. In addition to being expertly knowledgeable in his field, John's ability to communicate and relate to others is contagious. The professional training I received these years and the style I learned will benefit me in my future career.

I would also like to recognize and thank my RP committee members, Dr. Hua Guo, Dr. Yang Qin, Dr. David Dunlap and Dr. Terefe Habtayes for their valuable suggestions and assistance during my time as a graduate student. Thank you for taking time out of their busy schedules to assist me in completing my degree. To all the instructors who taught the courses, I want to say thank you and what I learned is really helpful.

To all my lab mates and people who trained me for all related instruments, thank you. First, Yongqian Gao, for all his help and guidance for me to familiarize our homebuilt laser systems and operation details. Then, to Eric Martin, Adam Wise, Alan Thomas, Tom Martin, Cody Aldaz, Jose Antonio Garcia Galvez, for their advice and help in the daily contemplations of physical chemistry. To Dr. Kirk and members of his group, I would like to acknowledge my appreciation for their help with NIR absorptions and EPR measurements. To Dr. Hua Guo and his students, Yongle Li and Ryan Johnson, thank you for your guidance and help with DFT calculations. Thank Fred Fuchs for his

help fixing the day to day problems in the labs. And also to CRLS for their help with N_2 fills and other lab supplies. Thank you all and your help are greatly appreciated.

To all my friends, thank you for being with me. Last but not least, I wish to thank my parents, my elder sister, my brother-in-law and my niece, I want them to know how much I love them and I deeply appreciate their support throughout my life.

Spectroscopic Studies of Conjugated Polymer Nanostructures and Polymer/Acceptor Blends

BY

Jian Gao

B.S., Chemistry, Shandong University, P. R. China, 2009

Ph.D., Chemistry, University of New Mexico, 2014

ABSTRACT

This dissertation presents the results of investigations into organic semiconducting systems at the nano- to mesoscales through spectroscopic and electrical imaging techniques. Particular emphasis was put on capturing the role of conformation and morphology on electronic properties and processes. The combination of experimental methods and data analysis techniques used in this work reveals useful insights into the correlations between polymer structures and their photovoltaic device performance, and provide clues to developing better performing organic solar cells.

The main approach of this work is using prototypical conjugated polymer systems, either ensemble or in their nanostructures, to study the solar cell active layer morphologies and chemical doping interactions. The first half of this work focuses on studying the active layer morphologies by self-assembled nanostructures, such as nanoparticles, nanofibers and intercalated bimolecular crystals, and their impact on electronic processes and solar cell device efficiencies. Firstly, nanoparticles of poly(9,9-

dioctylfluorene-co-bis-N,N-(4-butylphenyl)-bis-N,N-phenyl-1,4-phenylenediamine) (PFB) and poly(9,9-dioctylfluorene-co-benzothiadiazole) (F8BT) were fabricated and used to study the interface characteristics of donor/acceptor. Efficient energy transfer from PFB to F8BT was observed instead of charge transfer states typically seen in well mixed F8BT/PFB films.

Poly(3-hexylthiophene) (P3HT) nanofibers (NFs) were next fabricated to study the pure polymer aggregates and examine the delicate interplay between intra- and inter-chain exciton couplings in π-stacked polymer aggregates. J-type aggregate features of P3HT NFs were initially present and preserved after encapsulation. A time-dependent Raman intensity analysis was used to quantitatively estimate vibrational mode-specific excited state structural displacements.

Furthermore, poly(2,5-bis(3-tetradecylthiophen-2-yl)thieno[3,2-b]thiophene) (PBTTT) and [6,6]-phenyl C61 butyric acid methyl ester (PCBM) intercalated systems were used to study the polymer/fullerene intermixed regions. Different PBTTT conformers are identified and their contributions to photocurrent production are also mapped in solar cell devices. The ordered PBTTT chains are most concentrated in PCBM-rich crystallites that exhibit high non-geminate recombination rates and low photocurrent.

The later part of this work focuses on the chemical doping interactions between P3HT and the small molecule electron acceptor, 2,3,5,6-tetrafluoro-7,7,8,8-tetracyanoquinodimethane (F_4-TCNQ). Firstly, we examine the changes in polymer conformation when P3HT comes into contact with F_4-TCNQ. Doping P3HT with F_4-TCNQ appears to planarize the polymer backbone and decrease pristine aggregate

amounts, and increasing F_4-TCNQ loading results in larger P3HT/F_4-TCNQ fibril-like domains.

Next we investigate the effects of P3HT conformation and packing on charge transfer interactions between P3HT and F_4-TCNQ using regioregular (r-Re) and regiorandom (r-Ra) P3HT. R-Re P3HT is seen to produce significantly larger numbers of free charge carriers compared to r-Ra P3HT with similar F_4-TCNQ loadings. This suggests that aggregates are necessary for hole delocalization and efficient doping.

DECLARATION

This dissertation includes eight chapters. Chapter 1 gives a general introduction of this work, and Chapter 2 lists all detailed instrument setups and sample preparations. The main body of the dissertation is written in a form of five papers, which have already been published or submitted, as listed below.

Chapter 3: *Chem. Phys. Lett.* **2012**, *522*, 86-91.

Chapter 4: *Langmuir* **2012**, *28*, 16401-16407.

Chapter 5: Submitted.

Chapter 6: *J. Mater. Chem. C* **2013**, *1*, 5638-5646.

Chapter 7: *J. Phys. Chem. Lett.* **2013**, *4*, 2953-2957.

My research advisor, Professor John K. Grey, supervised all of these publications as the corresponding author. Professor So-Jung Park and Dr. Amanda Kamps participated in the project discussed in Chapter 4 and they are included as co-authors. Professor Adam Moulé, Professor Hua Guo, Dr. John Roehling and Dr. Yongle Li are included in Chapter 6. Chapter 7 includes Dr. Edwards T. Niles for assisting the EPR measurements. In addition, Professor Hua Guo, Dr. Ryan Johnson, and Alan Thomas are involved in Chapter 5 for assisting DFT calculations and device measurements.

TABLE OF CONTENTS

LIST OF FIGURES

LIST OF TABLES

LIST OF ABBREVIATIONS

A	Electron acceptor
AFM	Atomic force microscopy
AM	Air mass
APD	Avalanche photodiode
BCP	Block copolymer
BHJ	Bulk heterojunction
c-AFM	Conductive atomic force microscopy
CB	Chlorobenzene
CCD	Charge coupled detector/device
$CDCl_3$	Deuterated chloroform
CELIV	Charge extraction by linearly increasing voltage
CT	Charge transport
CTC	Charge transfer complex
CS	Charge separate
D	Electron donor
DFT	Density functional theory
DOS	Density of electronic states
ED	Electron diffraction
EELS	Electron energy loss spectroscopy
EPR	Electron paramagnetic resonance
EQE	External quantum efficiency
ET	Energy transfer

ETE	Energy transfer efficiency
eT	Electron transfer
F8BT	Poly-(9,9-dioctylfluorene-co-benzothiadiazole)
F_4-TCNQ	2,3,5,6-tetrafluoro-7,7,8,8-tetracyanoquinodimethane
FET	Field effect transistor
FF	Fill factor
GIF	Gatan imaging filter
GIXRD	Grazing-incidence x-ray diffraction
HFB	Hexafluorobenzene
HOMO	Highest occupied molecular orbital
h	Planck constant
MDMO-PPV	Poly[2-methoxy-5-(3,7-dimethyloctyloxy)-1,4-phenylene-vinylene]
NF	Nanofiber
IMPS	Intensity modulated photocurrent spectroscopy
IPCE	Incident photon to current efficiency
IQE	Internal quantum efficiency
IRF	Instrument Response Function
ISC	Inorganic solar cells
I_{sc}	Short circuit current
ITO	Indium tin oxide
J	Current density
k	Boltzmann constant
LUMO	Lowest unoccupied molecular orbital

ns	Nanosecond
NSOM	Near field scanning optical microscopy
o-DCB	o-dichlorobenzene
OLED	Organic light-emitting diode
OLEFET	Organic light emitting field-effect transistors
OPV	Organic photovaltaic
P3HT	Poly (3-hexylthiophene)
PBTTT	Poly-(2,5-bis(3- tetradecylthiophene-2-yl)thieno[3,2-b]thiophene)
PCBM	[6, 6]-phenyl-C61-butyric acid methyl ester
PCPDTBT	Poly[2,6-(4,4-bis-(2-ethylhexyl)-4H-cyclopenta [2,1-b;3,4-b']dithiophene)-alt-4,7(2,1,3-benzothiadiazole)]
PDI	Polydispersity index
PEDOT: PSS	Poly (3, 4-ethylenedioxythiophene) poly (styrenesulfonate)
PFB	Poly-(9,9-dioctylfluorene-co-bis-N,N-(4-butylphenyl)-bis-N,N-phenyl-1,4-phenylenediamine
PHT_{20}-b-PEG_{108}	Poly(3-hexyl-thiophene)-block-poly(ethylene-glycol)
P_{in}	Input power of photons
PL	Photoluminescence
P_{max}.	Maximum output power
ps	Picosecond
PSC	polymeric solar cells
PTV	Poly(thiophene vinylene)

PVA	Polyvinyl alcohol
r-Ra	Regiorandom
r-Re	Regioregular
SCLC	Space charge limited current
SDS	Sodium dodecyl sulfate
SERS	Surface-enhancement Raman spectroscopy
SMS	Single molecule spectroscopy
STEM	Scanning transmission electron microscopy
TCO	Transparent conductive oxide
TCSPC	Time-correlated single photon counting
TEM	Transmission electron microscopy
TOF	Time of flight
V_{max}	Maximum output voltage
V_{oc}	Open circuit voltage
XRD	X-ray diffraction

Chapter 1

Introduction

1.1 Overview and Motivation

Organic polymer solar cells have attracted widespread interest in both academic and industry communities.[1-7] Although power conversion efficiencies of organic solar cells are currently relatively low in comparison to inorganic solar cells, they still show the potential to be an effective alternative solar cell technology.[8] The focus of industrial and academic studies is needed and the efficiencies of organic solar cells can be further improved in order for this to be feasible.[3,4]

First generation organic solar cells were based on single-layer pristine polymers or small molecule organic crystals sandwiched between two electrodes with different work functions, which resulted in poor photocurrent efficiency because of low charge generation.[7-9] In 1986, Tang and co-workers reported photocurrent generation by using a CuPc/perylene derivative bilayer for an organic solar cell device.[10] Excitons, bound electron-hole pairs formed by photon absorption, can diffuse within the electron donor phase to an interface with electron acceptors, and energy offsets between these donor/acceptor materials drive exciton dissociation.[11,12] However, significant Coulomb attraction (0.1-0.5 eV)[9] will still keep electron/hole bound together. The dissociation of these bound electron-hole pairs will lead to free charge carriers, and then holes can be collected by anode and electrons collected by cathode. The efficiency of this type of donor/acceptor bilayer devices can be limited by exciton diffusion length since excitons can be quenched before reaching donor/acceptor interfaces.[13,14]

In order to overcome this issue in bilayer organic solar cells, the concept of bulk heterojunction (BHJ) as active layers is most commonly used.[9,15,16] A bicontinuous interpenetrating network of electron donors and acceptors can be formed in BHJ active layers by spin-coating donor/acceptor mixed solutions, and donor/acceptor interface area is increased significantly, which permits efficient exciton dissociation and high charge photogeneration.[17,18] In BHJ solar cell systems, conjugated polymers are usually employed as electron donors and fullerene as electron acceptors.[19-21] Figure 1.1 shows a typical structure of organic BHJ photovoltaic devices and a diagram of charge generation and transport processes.[22-25]

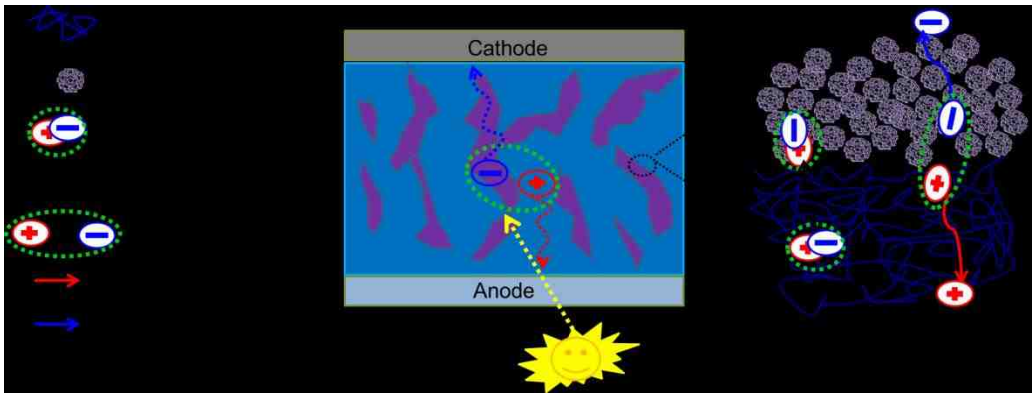

Figure 1.1 Schematic of charge photogeneration and transport processes in a polymer/fullerene bulk heterojunction photovoltaic device.[2,26]

1.1.1 Active Layer Morphology

In order to achieve maximized device performance, all the charge formation processes, such as photon absorption, exciton diffusion, charge separation, charge transport and collection, should occur efficiently.[27,28] Therefore, the improvement of power conversion efficiency can be linked to design new semiconducting materials, and

also get better understanding and control of the active layer morphologies.[29] As shown in Figure 1.2, these active layer nanostructures, such as their size, packing order, phase purity and distribution, can affect current generation processes significantly and govern overall solar cell efficiency.[29-32]

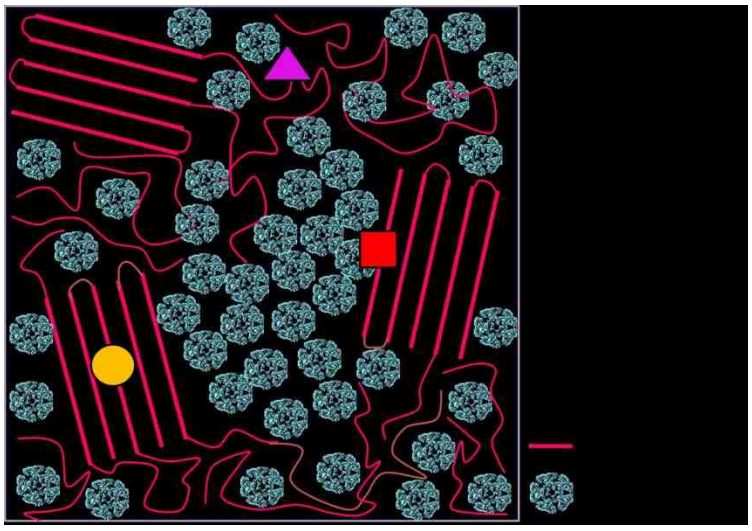

Figure 1.2 The active layer nanostructures of organic solar cell systems. Red square symbol stands for polymer/fullerene interfaces, yellow circle is for pure polymer domains, and purple triangle is for polymer/fullerene intermixed regions.

Depending on the properties of donor/acceptor materials, the features of their active layers might include pure polymer aggregates (yellow circle in Figure 1.2),[33,34] pure fullerene clusters and polymer/fullerene intermixed regions (purple triangular in Figure 1.2).[35,36] Polymer/fullerene interface (red square in Figure 1.2) offers the opportunity for excitons to split into free charge carriers, but meanwhile, the generated charges can be quenched by charge recombination at this interface. Benerji and co-workers reported ultrafast charge generation occurs predominantly in polymer/fullerene intermixed regions,[30] while charges are generated more slowly from excitons in pure

polymer domains since excitons need diffuse to the polymer/fullerene interface for charge separation.[30,37] On the other hand, pure polymer/fullerene domains are helpful to prevent charge recombination, but they must be small enough to overcome exciton quenching.[35] A further understanding of these nanoscale morphologies, polymer/fullerene interfaces, pure domains and their intermixed areas, is needed and will be helpful to develop structure-function relationships of organic semiconducting materials and fabricate photovoltaic devices with better performance.

Therefore, the first half of this dissertation will be focused on the active layer nanostructures using prototypical polymer systems that are shown in Figure 1.3. F8BT and PFB copolymer blend is an ideal system to study the donor/acceptor interfacial processes since this blend can possess an emissive charge transfer state at their interface, which is called exciplex that can be a direct probe for donor/acceptor interface morphology.[38,39] The well-known polymer system, P3HT, will be used to study pure polymer domains since P3HT can easily generate aggregate features even in solutions.[40-42] The high miscibility of PBTTT/PCBM makes this blend as a good model for studying polymer/fullerene intermixed phases since PCBM prefers to intercalate into PBTTT side chains, which cause their bimolecular structure formation.[42-44] The more details of these active layer morphology studies will be discussed in Chapter 3, 4 and 5.

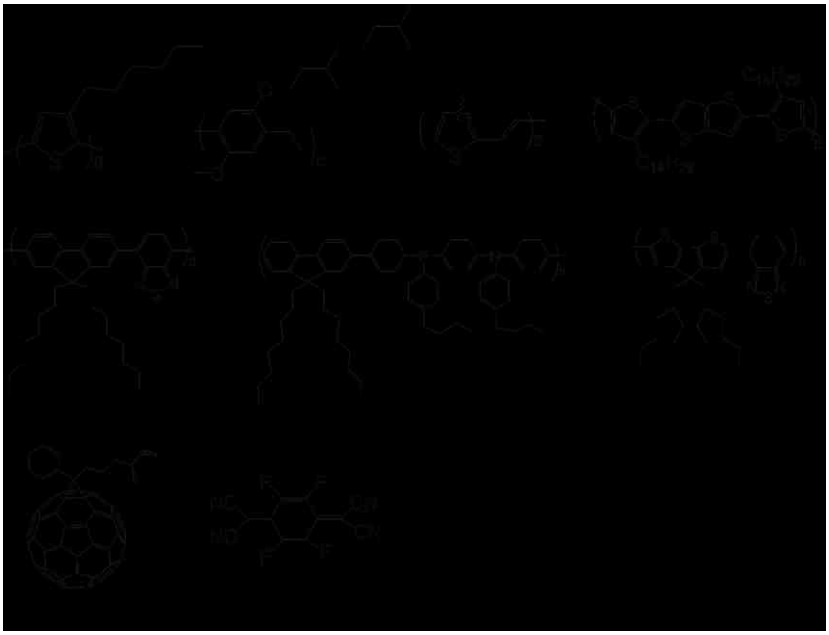

Figure 1.3 Structures of the polymers (and PCBM, F_4-TCNQ) discussed in this dissertation.

1.1.2 Chemical Doping

In addition to getting better control of active layer morphologies, chemical doping method has been proved to be an efficient way to modify materials' optical and electrical properties and therefore benefit the overall device performance.[45-47] Specifically, a charge transfer interaction will happen after adding a small amount of strong electron acceptors into the conjugated polymer systems. The increased carrier density will give rise to improved conductivities of the system,[48-50] which have been shown to exhibit up to 5-8 orders of magnitude higher after doping the active layers with strong electron acceptors.[46,51]

Sufficient energetic offset, which refers to the energy level difference between highest occupied molecular orbital (HOMO) of semiconductors and lowest unoccupied

molecular orbital (LUMO) of dopants, is required for efficient doping. [48,51,52] Current studies have shown the successful doping behaviors in organic solar cell systems, but most of them are proceeded from the materials' electrical properties and mechanistic aspects with chemical doping.[53-55] For example, Sun and coworkers reported power conversion efficiency (PCE) of a classic system, P3HT/PCBM, is improved about 15% after F_4-TCNQ doping.[56] However, there still lacks a general understanding of the doping process and how this interactions affect the polymer conformations and in turn how polymer structures affect this doping behaviors.[48,57] In the second half of this dissertation, I will explore polymer structure changes upon doping and their effects on doping efficiency as well, by studying the model system, P3HT doped with F_4-TCNQ, and the details will be discussed in Chapter 6, 7.

Overall, the work presented in this dissertation is aim to enhance our understanding of the active layer morphologies of organic BHJ solar cells and also explore the mechanisms of chemical doping interactions using prototypical conjugated polymer systems, as discussed above. It covers the studies of donor/acceptor interfaces, polymer domains, polymer/fullerene intermixed regions, and polymer systems with chemical doping as well. These studies will help further develop structure-function relationships of organic semiconducting materials and discover new ways to obtain higher efficiency photovoltaic devices.

1.2 Active Layer Morphology Study

Exciton diffusion and charge separation efficiency is dependent on film morphologies, especially donor/acceptor interface regions.[58] Exciton dissociation as well as charge transport needs to be balanced in order to increase charge generation and decrease charge recombination. If phase separation length scales are much larger than exciton diffusion length, an exciton will be quenched before reaching donor/acceptor interfaces. In other words, charge recombination will dominate if phase separation is too small and also charge transport will be limited.

Morphology in BHJ solar cell system can be modified before and after active layer formations, such as varying donor/acceptor ratios,[59] choosing different solvents,[60] fabricating nanostructured aggregates,[61] adding additives,[62] adjusting donor/acceptor miscibility[63] and thermal/vapor annealing post-processing.[64]

1.2.1 Impact of Solvents

Since the active layers of organic BHJ solar cells are typically formed by spin-coating donor/acceptor mixed solutions, the choice of solvents has significant influences on the film morphologies and thus on device performances.[15,65-67] Specifically, the solubility of semiconducting materials in different solvents determines how donor/acceptors mix in solutions and the solvent evaporation rate determines phase separation scales of donors and acceptors.[68,69]

Normally, the systems using solvents with halogens, such as chloroform (CF), chlorobenzene (CB) and dichlorobenzene (DCB), can achieve higher device efficiencies because of their good solubility for conjugated polymers.[70-73] Shaheen and co-workers

found MDMO-PPV/PCBM system fabricates a threefold better device from CB solution than that from toluene solution,[74] which Shaheen and Hoppe's groups attributed to the higher solubility of MDMO and PCBM in CB and the smaller scale of phase separation.[74-76] Ruderer and co-workers investigated the effect of different solvents on the morphology of P3HT/PCBM system by using CF, toluene, CB, and xylene.[77] Surprisingly, device performance behaves similar for all these solvents, since their phase separation is within exciton diffusion length.[77] In addition, Yu and co-workers observed both absorption and charge mobility of P3HT/PCBM device increased when using high boiling point solvents.[78]

Here we use F8BT/PFB system as an example to study solvent effects on the film morphology and optical characteristics varying in different solutions.[1] F8BT/PFB blend tends to form uniform blend films with nanoscale phase separation as reported previously.[79] Charge photogeneration can be improved when F8BT/PFB blend films have larger phase segregation, which prohibits charge recombination and creates paths for charge transport. Domain sizes in F8BT/PFB can be modified by using different organic solvents.

Figure 1.4 shows F8BT/PFB thin films' topographies that cast from a) p-xylene and b) chloroform solutions, respectively. Due to the high boiling point of p-xylene, well-separated phase domains are generated by spin-coating F8BT/PFB p-xylene solution, while well-mixed features are observed from their chloroform solution due to the fast evaporation rate of chloroform. Large scale phase separations of F8BT/PFB copolymers will limit the amounts of charge transfer states since F8BT/PFB interfaces decrease; but for uniform mixed films, charge transfer states will have a large population, which can be

tracked by exciplex emission intensity.[80] For F8BT/PFB system, the optimum balance between exciton dissociation and charge recombination can be reached when the phase separation fluctuates at ~20 nm scale.[79]

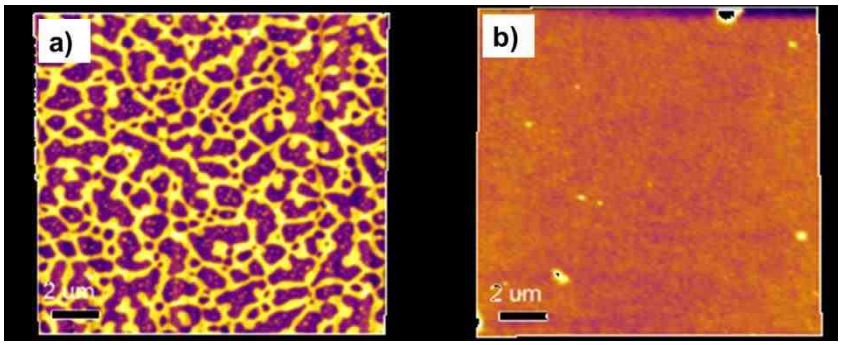

Figure 1.4 AFM images for 1:1 PFB/F8BT bulk films cast from a) p-xylene and b) chloroform solutions.[81]

1.2.2 Self-Assembled Nanostructures

The degree of active layer crystallinity plays an important role on OPV device performance since the high crystallinity can make charge transport process more efficiently while charges will be more easily trapped in the disordered films.[82] In order to get better performing devices, some additional post-processing, like thermal or solvent vapor annealing, is needed to optimize phase separation and donor/acceptor crystallization, and achieve efficient charge separation and transport by large donor/acceptor interfacial areas and their continuous phases.[83] However, post-processing for active layers has its limitations because of the high sensitivity of active layer morphology to annealing conditions and low glass transition temperatures (Tg) of conjugated polymers. Therefore, it is necessary to develop alternative approaches for modifying organic solar cell active layer morphologies.

The bottom-up approaches, self-assembly of donor/acceptor nanostructures, have been approved to be a promising way to adjust donor/acceptor crystallinity and control the active layer morphologies in organic solar cell systems.[84-86] The most-studied materials, P3HT/PCBM, in the world for organic photovoltaic applications, are very sensitive to annealing process since the high crystallinity for this system is crucial to get high PCE. By pre-assembling P3HT into well-ordered nanofibers and mixing them with PCBM is feasible to increase P3HT crystallinity in P3HT/PCBM solar cell systems.[87,88] Figure 1.5 a) and b) show the TEM images of self-assembled P3HT nanofibers from anisole and toluene solutions, respectively. P3HT nanofibers from anisole solutions have averaged width of ~20 nm while for toluene nanofibers, their averaged width is ~40 nm. In some cases, both types of P3HT nanofibers are found in toluene solutions, as shown in Figure 1. 5c. The crystallinity and inner polymer structures of these nanofibers can be adjusted by fabrication conditions, such as solvents, polymer concentrations, and environments. Recently, both Sum and Cacialli research groups demonstrated the improvements of organic solar cell efficiency by using P3HT nanofibers and fullerene blends.[89,90] Interestingly, Sum and co-workers also reported the controllable nanofiber alignments by using an external electric field treatment[90] and this technique could help further modify the charge transport processes in pure polymer domains.

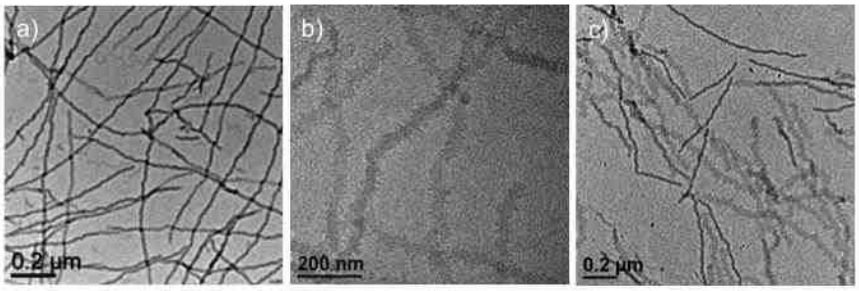

Figure 1.5 TEM images of pristine nanofibers made from a) anisole solutions and b) toluene solutions. c) Mixture of different types of nanofibers that randomly happened in toluene solutions.[91]

1.2.3 Polymer/Fullerene Miscibility

As well as solvents and polymer crystallinity, the active layer nanoscale morphology is highly dependent on polymer/fullerene miscibility. Studies have demonstrated the co-existence of pristine P3HT crystalline, PCBM crystalline and molecularly mixed P3HT/PCBM domains in P3HT/PCBM blend systems.[92] Besides, an amorphous polymer, poly[2-methoxy-5-(3,7-dimethyloctyloxy)-1,4-phenylene-vinylene] (MDMO-PPV), has shown good molecular mixing with PCBM.[93] Polymer/fullerene molecular mixed phases can also emerge through fullerene intercalation into polymer side chains and form polymer/fullerene bimolecular crystals, e.g., poly-(2,5-bis(3-tetradecylthiophene-2-yl)thieno[3,2-b]thiophene) (PBTTT)/PCBM blends, as shown in Figure 1.6.[43,92]

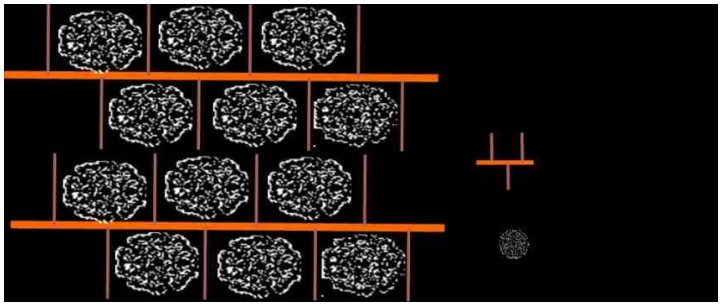

Figure 1.6 Schematic of PBTTT/PCBM intercalated structures.

The efficiency of exciton quenched by charge transfer can be improved by molecular mixing when fullerenes intercalate into polymer side chains. In this type of

polymer/fullerene mixed phase, excitons do not need to diffuse on nanometer length scales before splitting since donor/acceptor interfaces are very close to the initially exciton originating regions (on the scale of angstroms). However, traps can be introduced into this type of intercalated structures and cause high geminate charge recombination rate.[30] In order to prevent geminate charge recombination and meanwhile, create sufficient paths for charge transport, extra content of fullerene is typically needed for the intercalated polymer/fullerene systems. For example, the optimal ratio of both MDMO-PPV/PCBM and PBTTT/PCBM systems is ~1:4 w/w loading for fabricating solar cell devices.[94-96]

Polymer/fullerene miscibility can be relied on varying the combinations of polymers and fullerenes or modifying polymer/fullerene structures. For example, PCBM can easily intercalate into PBTTT side chains while PCBM totally phase separated when blending in poly(benzo[1,2-b:4,5-b']dithiophene-alt-thieno[3,4-c]pyrrole-4,6-dione) (PBDTTPD) system.[30] On the other hand, Chabinyc and coworkers tuned the fullerene miscibility in poly(3-hexylselenophene) (P3HS) systems by attaching two bulky side groups on fullerene and PCE was proved to increase after the fullerene structure modifications.[97] The further details of this type of polymer/fullerene mixed phase will be discussed in Chapter 5.

1.3 Spectroscopic Studies

1.3.1 Overview

In this dissertation, spectroscopic and imaging techniques are commonly performed in most measurements and analysis. A sample's electronic structure and conformation can be inferred by its photon absorption, emission and scattering.[98-101] Figure 1.7 shows a schematic diagram for the simplified relevant processes, such as electronic absorption, emission, resonant and off-resonant Raman scattering.

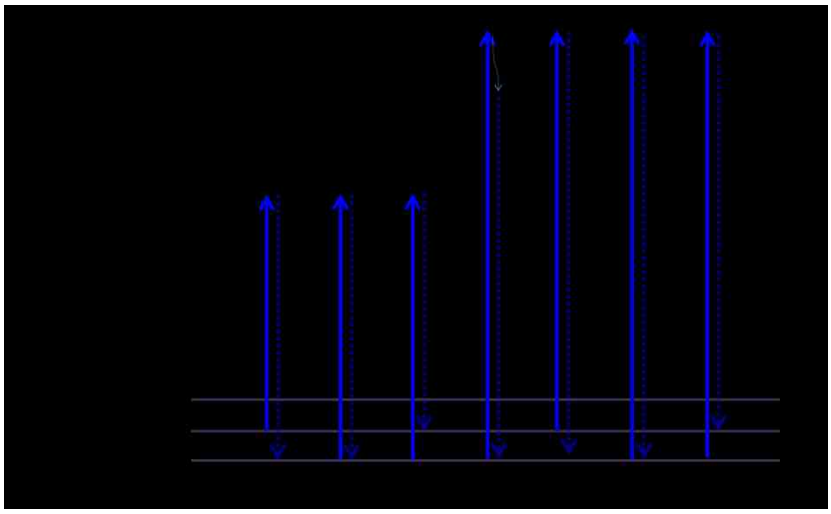

Figure 1.7 Schemes of absorption, fluorescence, Raman and resonance Raman processes.

Absorption spectroscopy here refers to a common spectroscopic technique that measures the absorption intensities of photons as a function of wavelength when photons interact with our samples.[102,103] The absorption, especially in infrared and UV-vis range, is used as an analytical tool to help us qualitatively and quantitatively analyze the samples' constituents, and also further utilized in molecular and atomic physics studies. After the absorption of a photon, an electron in a molecule can be promoted to a higher

energy state, and the excited molecule will undergo a fast relaxation process to the band edge and then decay to a lower energy state by either photon emission or a non-radiative thermal mechanism.[104-106] The emitted photons, as a function of wavelength, can be collected to generate emission spectrum for the specific molecules during this electron transition. Similar as absorption, emission spectroscopy can be used to determine the elemental composition of a sample and also electronic structure by analyzing wavelengths of emitted photons as well.[107-109]

Raman spectroscopy is a technique that has been worldwide used in polymer characterizations to study molecule vibrations in both qualitative and quantitative analysis methods.[110,111] It is based on inelastic scattering, which means the frequency of incident photons changes upon interacting with a sample. These changes provide the information about molecule vibration strength in conjugated polymer systems. Only a very small portion of inelastic scattering (Raman scattering, $1/10^7$) happens,[112,113] while most emitted photons are scattered elastically (Rayleigh scattering). There are two types of Raman scattering, Stokes and anti-Stokes. With respect to the incident photons, the energy of Stokes scattering is one vibrational quantum lower while anti-Stokes scattering energy is one quantum higher. Under room temperature, Stokes scattering is dominant in Raman spectrum. Raman scattering is typically very weak, but it will be enhanced by 10^2-10^6 order of magnitude when exciting a sample on the resonance of its optical transitions.[114-117]

1.3.2 Theoretical Model for H- and J-type Aggregates

An optical lineshape profile can be expressed by a Poisson distribution and for a single phonon mode system, the relative intensities of each vibronic transitions (overtones) only depend on its nuclear displacement after photo excitation and quantum number.[118-120] However, optical spectra for polymers that form aggregates might deviate from a Poissonian distribution due to molecular dipole-dipole coupling interactions which can affect electronic transitions. In other words, polymer aggregates in both solutions and films generally can be recognized by optical spectroscopic methods, such as their absorption and emission.[40]

Based on different electronic and spectroscopic properties, packing of conjugated polymers can be divided into H-type and J-type aggregates.[121-123] Dipole moment transition of a monomer and alignments of molecule dimers can be utilized to study chain packing and interactions in polymer aggregates. Figure 1.8 shows two dipoles interact and result in excited state S_1 splitting into two energy levels, E_1 and E_2, which stand for discrete allowed and forbidden transitions for J-(H-) type aggregates in conjugated polymer systems.

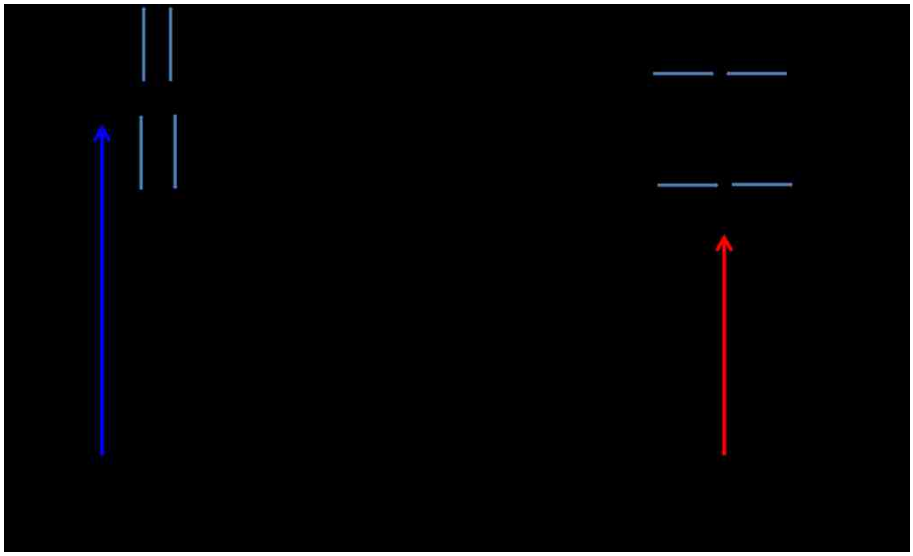

Figure 1.8 The energy diagram of H- and J-type aggregates.

The higher excited energy state E_2 for H-type aggregates depicts face-to-face dipole alignment, which is a transition allowed state and labeled by blue line while for J-type aggregates, interacted dipoles align as head-to-tail, which occupy lower excited energy state E_1. In polymer aggregates, instead of two dipole interactions, there are multiple dipoles interacting with each other and based on transition allowed or forbidden features, optical spectroscopic characteristics can help identify whether H/J-type aggregates dominate in the systems.[121,124,125]

Spano and co-workers have developed a theoretical model of weakly coupled aggregates in order to understand how P3HT absorption and emission transitions are affected by these couplings, such as intermolecular coupling, exciton-phonon coupling.[121,126] This model permits simple lineshapes analyses of optical spectra to acess how polymer aggregation affects exciton coupling. The electronic coupling factor, *J*, is used to analyze the electronic transitions and decreases exponentially with polymer chains distance. The expression for absorption is described in Equation 1-2, where W is the exciton bandwidth that equals to 4*J*, G_m stands for the total possible transitions from n to m ($G_m = \sum_{n \neq m} S^m / n!(n-m)$), Γ is a function of inhomogeneous lineshape, E_{00} is the energy of 0-0 transition, E_p is the vibration energy of C=C symmetric stretch mode.

$$A \propto \sum_{m=0} \left(\frac{S^m \exp(-S)}{m!} \right) \left(1 - \frac{W \exp(-S)}{2E_p} G_m \right)^2 \Gamma\left(\hbar\omega - E_{00} - mE_p\right) \quad (1\text{-}1)$$

The relative intensity of 0-0 and 0-1 transitions is very sensitive to polymer packing and type of aggregations and their intensity ratios can be used to estimate the exciton bandwidth W by Equation1-3:

$$\frac{A_{0-0}}{A_{0-1}} \approx \left(\frac{1 - \frac{0.24W}{E_p}}{1 + \frac{0.73W}{E_p}} \right)^2 \quad . \tag{1-2}$$

The calculated W can help qualify polymer aggregations. It is inversely proportional to the intensity ratios of 0-0/0-1 (<1) transitions in H-aggregates. However, in J-type aggregates, the W values are proportional to the 0-0/0-1 intensity ratios (>1). Therefore, the H-aggregate model can be used to estimate the strength of electronic coupling and analyze the proportion of polymer intra-/inter-chain aggregates from optical spectroscopy.

1.3.3 H- and J-type P3HT Nanofibers

Typically, J-type aggregates appear as a red-shifted narrow absorption peak while H-type aggregates have a blue-shifted absorption feature corresponding to disordered polymer molecules.[121] Niles et al reported nanofibers from P3HT toluene solutions exhibit pronounced intra-chain exciton coupling, which leads to J-type aggregate behavior;[127] and nanofibers from anisole solutions show dominant inter-chain exciton coupling and therefore, H-type aggregate behavior. Figure 1.9A) and B) show typical emission spectra for P3HT nanofibers made from anisole and toluene solutions, respectively. In J-type nanofibers, P3HT chains are much more elongated chains than that in H-type aggregates and show higher intra-chain order.[127,128] Chapter 5 will expand more details on both H- and J-type P3HT nanofibers.

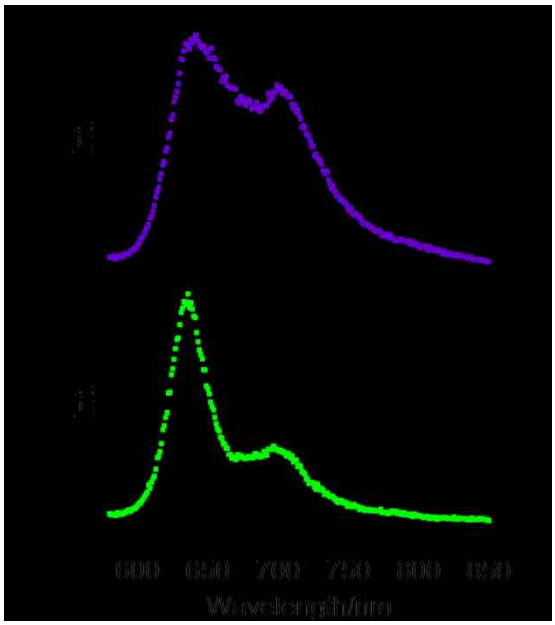

Figure 1.9 Emission spectra of solution dispersions of A) anisole and B) toluene assembled P3HT nanofibers.

1.4 Time Dependent Theory of Spectroscopy

1.4.1 Overview

In this dissertation, I will also use the time-dependent theory of spectroscopy that developed by Heller and co-workers in the late 1970s, to simulate electronic absorption spectra, emission spectra, and resonant Raman scattering, and uncover the changes of excited state geometry and early vibrational dynamics in polymer/fullerene blends. Specifically, a classical or semi-classical picture of the electronically resonant spectroscopies is not that practical when the spectroscopic active system turns to large molecule or some molecule with condensed phase environment, like conjugated polymer system, due to the computational disadvantage of complicated expressions and the lack of dynamic allusions.[129,130] Subsequently, Heller and coworkers introduced the time-dependent theory of electronic and Raman spectroscopy by adding an interpretation in

terms of overlaps of nuclear wavepackets.[130-132] The initial nuclear wave function is a localized wavepacket, which usually is a low lying vibrational state in ground potential surface while the wavepacket on the excited state is moving on Born-Oppenheimer potential energy surfaces after photo-absorption, as shown in Figure 1.10.[130] In order to simplify the calculations, we can assume the potential surface is harmonic and propagation of the wavepacket is only carried out for a few vibrational periods, so the wavepacket can remain constant Guassian lineshape without distortion and dispersion.

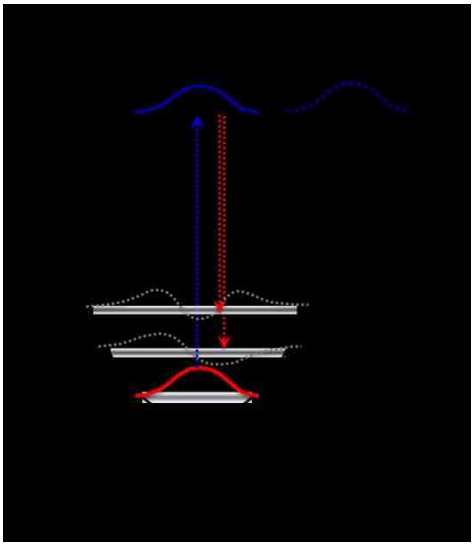

Figure 1.10 Time-dependent picture of electronic absorption and vibronic Raman spectra.

Therefore, the time-dependent overlaps $\langle \varphi | \varphi(t) \rangle$ decide the intensities of electronic absorption and resonance Raman spectrum. Specifically, wavepacket function $\varphi(t)$ stands for the nuclei movement by promoting the potential surface from its ground state to excited state.

1.4.2 Absorption

Absorption spectrum, theoretically, should include all the vibration modes aroused by changed geometry. However, due to homogeneous and inhomogeneous broadening effect, the spectrum is not well resolved in most cases. From Zink and Heller's study,[131,133] the intensity of absorption that includes all the displaced vibrational modes can be given by equations below:

$$A(\omega) = \omega \int_{-\infty}^{\infty} e^{i\omega t} \langle \varphi | \varphi(\mathrm{t}) \rangle \, dt \qquad (1\text{-}3)$$

$$\langle \varphi | \varphi(\mathrm{t}) \rangle = \exp\left\{ \left\{ -\sum_k \frac{\Delta_k^2 \left[1 - \exp(-i\omega_k t) - i\omega_k t \right]}{2} \right\} - \frac{iE_{00}}{\hbar} - \Gamma^2 t^2 \right\} \qquad (1\text{-}4)$$

Where ω is incident photon frequency, Δ_k is the vibrational displacement for mode k, ω_k is the frequency for mode k, E_{00} is the electronic origin energy, Γ is the damping factor. Due to the vertical transition, the initial overlap of $\langle \varphi | \varphi(t) \rangle$ (t=0) for absorption starts from its maximum value one and then reduces as the wavepacket travels away from its Franck-Condon region. Even when it comes back to its originating place, the autocorrelation values are still lower than one because of damping effects.

1.4.3 Raman Scattering

For resonance Raman, Raman mode intensity only depends on the overlap of $\varphi(t)$ and the specific vibrational wavefunction on the ground state. Raman intensity for each mode can also be calculated by time-dependent model and the expression is shown below:

$$I_{i\to f} \propto \omega_I \omega_S^3 \alpha_{fi} * \alpha_{fi} \tag{1-5}$$

$$\alpha_{fi} = \frac{i}{\hbar}\int_0^\infty \langle \phi | \phi(\mathrm{t}) \rangle * \exp\left[it\left(\omega_k + \omega_I - E_{00}\right) - \Gamma t \right] dt \tag{1-6}$$

where ω_I is incident photon frequency, ω_S is scattered photon frequency, ω_k is Raman mode vibrational frequency. The final states in Raman spectroscopy are excited vibrational states at ground potential surface. Normally, the larger the geometry changes of the excited states, the higher the fundamental and overtone intensities. For the systems with well-resolved overtone and combination bands, the autocorrelation function can be expressed as:

$$\langle \varphi | \varphi(t) \rangle = \prod_k \left\{ \exp\left[-\frac{\Delta_k^2}{2}\left(1-\exp\left(-i\omega_k t\right)\right) - \frac{i\omega_k t}{2} \right] * \left(1-\exp\left(-i\omega_k t\right)\right)^{n_k} * \frac{(-1)^{n_k}\,\Delta_k^{n_k}}{\left(2^{n_k} n_k\right)^{\frac{1}{2}}} \right\} \tag{1-7}$$

where n_k is the overtone order. These equations can be used to estimate displacement values of each vibrational mode by fitting the parameters with experimental results. Savin's formula (Equation 1-8) offers a simpler way to get the relative displacement values between different modes by comparing their Raman intensities.[134]

$$\frac{I_k}{I_{k'}} = \frac{\omega_k^2 \Delta_k^2}{\omega_{k'}^2 \Delta_{k'}^2} \tag{1-8}$$

Values for Raman autocorrelation functions start from zero since overlap of the wavepacket and its final vibrational states is zero. And then this value gradually increases and decreases while wavepacket travels back and forth, which causes recurrences in the overlap, as shown in Figure 1.11. For some conjugated polymer systems, like P3HT and

PBTTT, the long overtone progressions are observed, which will be discussed in Chapter 4, 5 and 6.

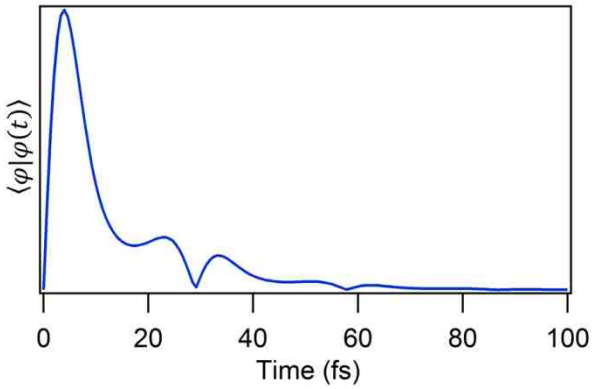

Figure 1.11 Intensity of Raman correlation overlap $\langle \varphi | \varphi(t) \rangle$ varies with time.[129,135]

1.5 Charge Transfer Doping

As discussed in 1.1.2, the performance of optoelectronic devices, such as organic light-emitting diodes (OLEDs), organic light emitting field-effect transistors (OLEFETs), and organic photovoltaic devices (OPV), can be improved with the addition of a small amount of appropriate strong electron acceptors.[48,136-138] Electronic properties of organic semiconductors can be tuned this way, like electrical conductivity has been proved to increase by a couple of order of magnitudes with respect to the pure materials in polymer/dopant systems.[46] Beside the changes of hole mobility and absorption[56], film morphology, excited state lifetime and Fermi level of polymers in active layers are all modified significantly with doping.

P3HT doped with 2,3,5,6-tetrafluoro-7,7,8,8-tetracyanoquinodimethane (F_4-TCNQ) is one model system for studying polymer/dopant interactions and their front orbital energy levels are listed in Figure 1.12.[46,52] P3HT HOMO is ~5.0 eV compared to ~5.24 eV for of F_4-TCNQ LUMO and this sufficient energetic offset meets the requirements for efficient doping.

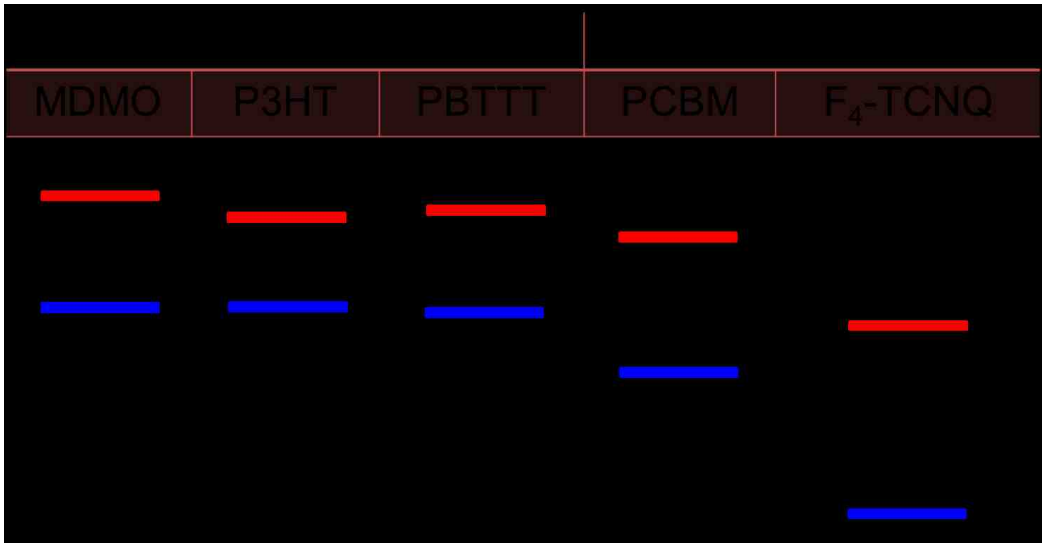

Figure 1.12 HOMO and LUMO energy levels of selected polymers and acceptors.

1.5.1 Two Models for Polymer/Dopant Interactions

In P3HT systems with F_4-TCNQ doping, Pingel and Neher found only about 5% of F_4-TCNQ takes effect on forming free charges by estimating P3HT conductivity and free hole density.[46,51] The doping efficiency is mainly dependent on the ground state charge transfer interactions between polymers and dopants. There are two contradictory models that are usually used to explain this type of polymer/dopant interactions, as shown in Figure 1.13, the integer charge transfer and hybrid charge transfer models. Integer charge transfer model describes a fully ionization between polymer and dopant, which will result in bound polymer/dopant hole-electron pairs or free hole/electron charge carriers.[51,139] Hybrid charge transfer model, as shown in Figure 1.13, presumes orbital hybridization between polymer HOMO and dopant LUMO upon polymer/dopant electronic interactions and forms hybrid orbitals of charge transfer complex (CTC),[140] which makes intermolecular excitation become possible and then generates free charge carriers.[51]

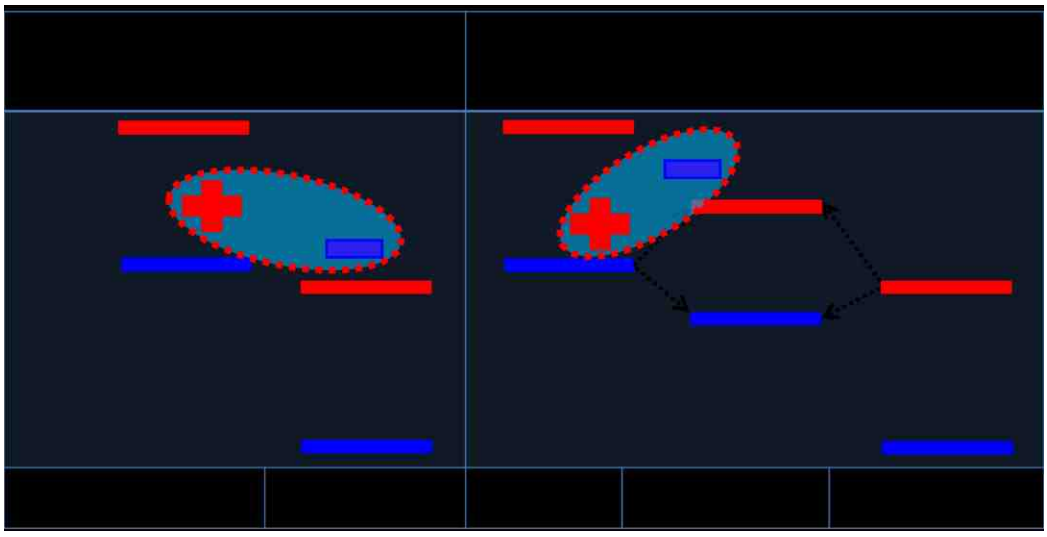

Figure 1.13 Two models for polymer/dopant ground state interactions.

The unexpected low doping efficiency suggests that formed charges remain tightly bound or only partial charge transfer happens in polymer doping systems.[46] Pingel and Neher recently found out most F_4-TCNQ dopants undergo integer charge transfer with P3HT donor, which is confirmed by the fact that the concentration of ionized F_4-TCNQ is only slightly lower than the calculated F_4-TCNQ molecular concentration.[51] The low hole concentration in this doping system is mainly due to tightly bound states of P3HT polarons and F_4-TCNQ anions, which cause low amounts of free charges even charge transfer occurs efficiently after P3HT and F_4-TCNQ contact.

1.5.2 Effect of Polymer Aggregates on Doping Efficiency

In order to stabilize charges on polymer backbones, electron density will redistribute across conjugated polymer chains and further cause molecular lattice relaxation. There are a lot of studies that have already been done to reveal basic mechanisms of P3HT doped with F_4-TCNQ systems while the effect of polymer conformation and aggregation features on doping efficiency is still in need of exploration.[46,51,55,141] Spectroscopic studies of polymer doping systems can help us understand how these ground state charge transfer interactions affect polymer conformations and aggregations. On the other hand, polymer conformation and packing characteristics are supposed to be essentially important for solution processed doping systems since polymer chain packing highly depends on the solvent solute interactions that might play a big role in polymer/dopant interactions. However, in order to verify

whether polymer structures and packing have significant effect on polymer/dopant interactions or not, experiments of different types of polymers with same dopant molecules need to be designed.

It is well-known that regio-regular (r-Re) P3HT has relatively more ordered structures and can form small aggregates even in solution while regio-random (r-Ra) P3HT always exists in amorphous conformation. Therefore, here we will use r-Re and r-Ra P3HT to study the polymer packing effects on polymer/F_4-TCNQ interactions. The relative doping efficiencies in these two types of polymer systems can be predicted by intensities of electron paramagnetic resonance (EPR) signals since unpaired charges will be detected directly by EPR measurements. Based on the integrated EPR signals, which will be further discussed in Chapter 7, doping efficiency for r-Re P3HT/F_4-TCNQ system is much higher than that of r-Ra P3HT. It indicates polymer aggregation is a crucial criterion for charge separation since ordered polymer chains make hole intra-chain delocalization possible while electron-hole pairs stay tightly bound in amorphous polymer systems, as shown in Figure 1.14. In the second part of this work, Chapter 6 and 7, we will discuss more details to uncover how F_4-TCNQ doping affects polymer backbone structures, and how polymer conformations and aggregation characteristics in turn affect polymer/dopant interactions upon doping efficiency.[142,143]

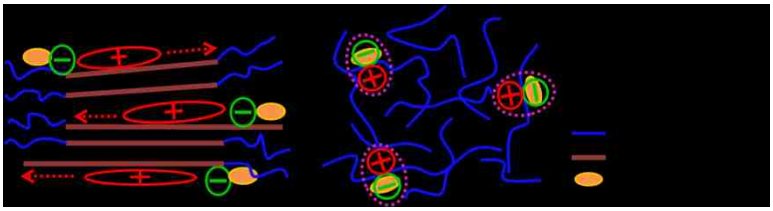

Figure 1.14 Schematic of F_4-TCNQ with r-Re and r-Ra P3HT interaction.[142]

Overall, the spectroscopic methods and data analysis techniques are very useful to enhance our understanding of organic semiconducting systems at the nano- to mesoscales. In the following chapters, relationship between structure and electronic properties and processes will be explored through the investigation of active layer nanostructures and chemical doping interactions. The results of these studies provide insights into the fundamental nature of this relationship and clues to developing better organic photovoltaic devices.

In Chapter 2, the details of instrumentation setups and experiments are presented. Chapter 3-5 present the active layer morphology studies of prototypical conjugated polymer systems from nanostructures to ensemble samples. Chapter 6-7 studied the chemical doping interactions using P3HT/F_4-TCNQ systems and explored how P3HT conformation changes upon interacting with F_4-TCNQ and the effect of P3HT aggregation on doping efficiency.

In Chapter 3, F8BT/PFB nanoparticles were used to study donor/acceptor interface morphology. Instead of charge transfer states, efficient energy transfer is found from PBT to F8BT in these blend nanoparticles with discrete nanodomains.

In Chapter 4, J-type NFs were fabricated to study polymer domains of active layers in organic solar cells. The interplay of intra-/inter-chain exciton couplings in polymer aggregates was also investigated by encapsulating these NFs with BCP.

In Chapter 5, PBTTT/PCBM intercalated structures are studied to further understand polymer/fullerene intermixed regions. Resonance Raman and photocurrent imaging was performed to spatially map different PBTTT conformers and their contributions to the photocurrent efficiency.

In Chapter 6 and 7 present the studies of P3HT/F_4-TCNQ chemical doping interactions by various spectroscopic and chemical mapping techniques. Complexed P3HT chains possess greater backbone planarity after interacting with F_4-TCNQ. Meanwhile, polymer aggregates offer paths for hole charges delocalization and promote doping efficiency.

Chapter 8 presents future research plans. Firstly, PBTTT/F_4-TCNQ interactions will be studied to understand how F_4-TCNQ changes PBTTT conformations and PBTTT/PCBM morphologies by optical, Raman, EPR and imaging spectroscopic methods. Secondly, single PBTTT nanoparticles are used to elucidate the structure and nature of PBTTT that is typically obscured in ensemble spectra.

Chapter 2

Experimental

2.1 Instrumentation

Instrumentation setups will be discussed in this chapter, which include high pressure spectroscopy, single molecule spectroscopy (SMS), time-correlated single photon counting (TCSPC), resonance Raman-photocurrent imaging spectroscopy, and intensity modulated photocurrent spectroscopy (IMPS).

2.1.1 High Pressure Spectroscopy

High hydrostatic pressure can influence polymer properties by squeezing them into new structural states, and make the quest for desirable optoelectronic features more efficient.[144] By applying a high pressure environment, it will create some new states or phase structures, which are usually absent under normal conditions and can be studied by spectroscopic methods to unravel the nature of polymers.[81]

Diamond anvil cell (A63000 uScopeDAC HT(G) by EasyLab) is used in this type of experiment, as shown in Figure 2.1. The pressure inside the cell is controlled by using a gas membrane as the driving force and tracked by the GM controller. Samples can be loaded into a pre-stressed steel gasket along with a methanol/water solution as the pressure-transmitting medium. Incident light is focused on the sample inside the diamond cell by microscope objective and then fluorescence or Raman spectra under a specific pressure are recorded using CCD spectrometer (Andor Newton). For better accuracy, pressures are calibrated using the R1 peak of ruby emission, as reported previously.[145-148]

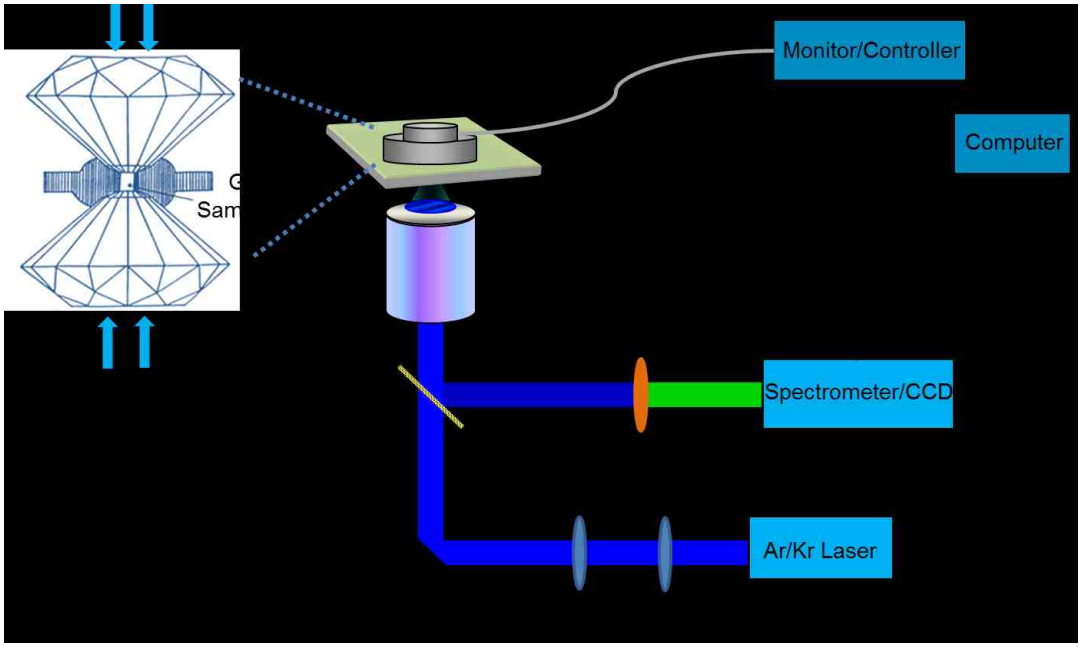

Figure 2.1 Schematic of high pressure experimental setup.

Figure 2.2 shows an example of pressure-dependent fluorescence measurements for P3HT NFs. J-type nanofibers were dispersed into polystyrene matrix first and then transferred to the inner part of steel gaskets. Intra-chain order of P3HT J-type nanofibers was decreased under high pressure and H-type behavior restores. This apparently delicate interplay between intra-chain order and inter-chain coupling is reversible and allows electronic coupling in P3HT aggregates to be reliably tuned between the H- and J-type limits.[149]

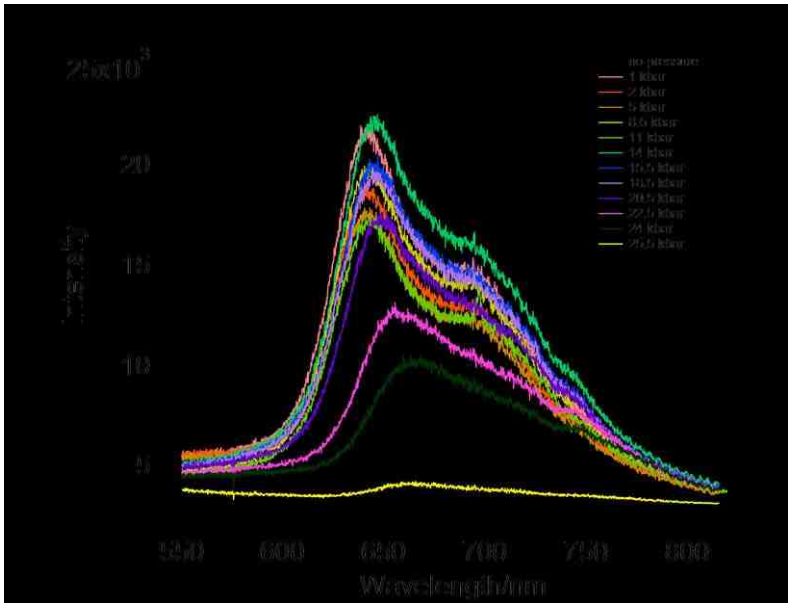

Figure 2.2 PL of J-type NFs under variable high pressures.

A63000 uScopeDAC HT(G) can reach its maximum pressure 22.21 GPa under proper alignments and operations. Due to the soft nature of conjugated polymers, most significant structural changes happen within 10 GPa.

2.1.2 Single Molecule Spectroscopy

Conjugated polymer electronic devices exhibit heterogeneous and extremely complicated dynamics that are very difficult to study from ensemble samples. Single molecule spectroscopy (SMS) has been used for the past two decades to investigate the optical and electronic properties of single conjugated polymer chains.[150,151] The results may be contrasted with measurements from bulk polymer samples, where average characteristics can be observed. The application of SMS on individual polymer chains or nanoparticles reveals the advantage on studying the relationship between chain conformations and their physical properties.

SMS is performed by confocal microscopy and incident light is focused to a very small spot (well below diffraction limit) on a well dispersed sample, which is composed of individual, isolated single molecules or nanoparticles in polystyrene matrix. The sample can be precisely moved with a nanopositioning translation stage (Madcity, Nano-View/M-XY) that is controlled by a LabView program, as shown in Figure 2.3. Emission signal is collected by an avalanche photodiode (APD) and a charge-coupled device (CCD) at the same time through a beam splitter.

As a sample on translation stage moving, APD measures its emission intensity and records it as a function of the position. A monochromator in front of CCD will spread the emission signal with a grating and then the spread light strikes on CCD which produces emission spectrum. Therefore, as shown on the right side of Figure 2.3, fluorescence images and spectra can be acquired simultaneously, and emission transients for individual molecules or nanoparticles can also be measured to study their dynamics.

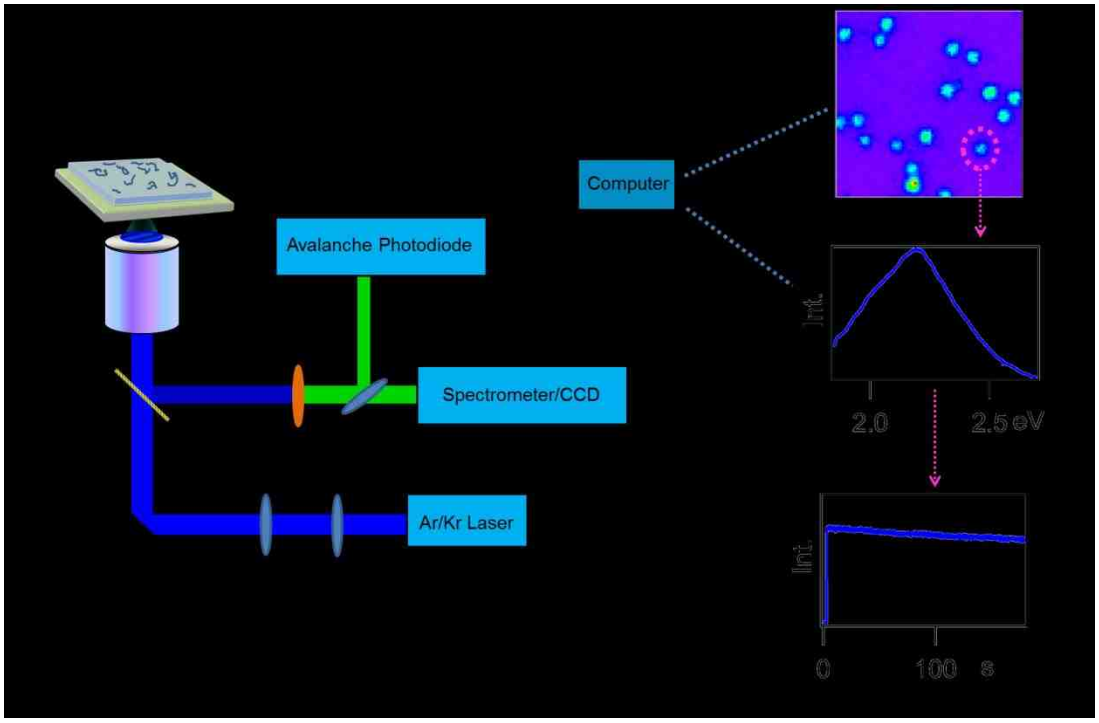

Figure 2.3 Schematic of SMS experimental setup.

2.1.3 Time-Correlated Single Photon Counting

Time correlated single photon counting (TCSPC) is a technique for measuring emission decays in a time frame between nanosecond and microsecond. Due to its high sensitivity and accuracy, TCSPC allows to measure PL decay for molecular monolayer films or polymer nanostructures. This technique is based on single photon detection, which records the arrival time of individual photons emitted by samples relative to excitation pulse. Normally, the probability of one photon being detected in one period is less than one, and in many periods there is no photon detected. A detected photon will be memorized with its relative detection time, and after many signal periods, all detected photons will contribute to a histogram that stands for an emission decay curve of the target sample.

The excited state lifetime can be calculated by fitting the decay curves as an exponential decay function:

$$I(t) = I_0 e^{-t/\tau} \tag{2-1}$$

where I_0 is the initial fluorescence ($t = 0$), $1/\tau$ is the decay rate for all pathways, τ is lifetime. If excitation pulse is wide and detectors or other electronics are not that accurate, the measured decay curves will not be purely exponential. In this case, instrument response function (IRF) needs to be de-convolved from the decay curves.

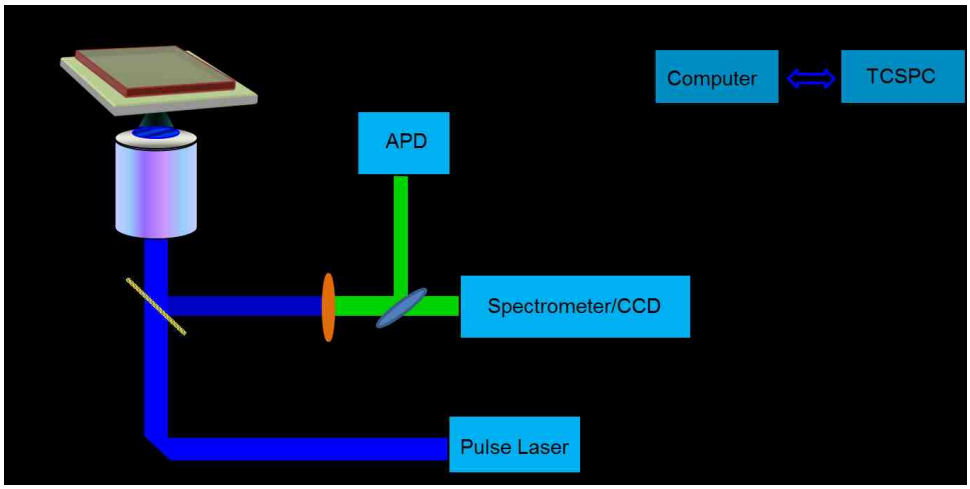

Figure 2.4 Schematic of TCSPC experimental setup.

TCSPC can be combined with SMS techniques to measure the excited state lifetime for individual nanoparticles or NFs, as shown in Figure 2.4. Furthermore, we can track the changes of relative amounts of different polymer species with high pressures by fitting the decay curves with multi-exponential functions, as shown in Figure 2.5. There is a fast (instrument-limited) decay component increasing at high pressures, which is attributed to excited state inter-chain torsional relaxation of NFs.[149]

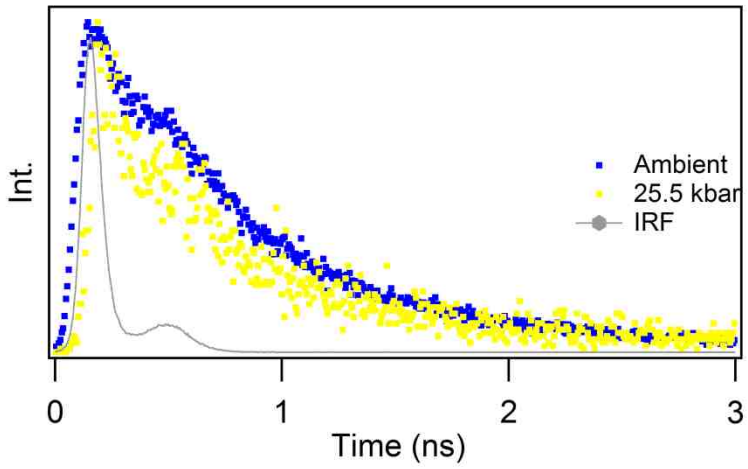

Figure 2.5 PL decay curves of J-aggregate P3HT NFs under different pressures. The grey line stands for IRF curve, which was measured by replacing samples with blank glass substrate.[149]

2.1.4 Raman-Photocurrent Imaging System

Resonance Raman spectroscopy can be used to identify different polymer backbone vibrations and spatially map polymer local structures in high resolution by a home-built instrumental setup.[152] As depicted in Figure 2.6, Raman spectra and imaging are acquired by a microscopy system, which is similar as SMS experiment, but the excitation intensity (~10^5 W/cm^2) is ~10^3 orders of magnitude higher due to the small cross section. Raman images of specific vibrational mode are plotted by integrating its Raman peak areas for each spectrum at each scan point. Lorentzian functions are used to de-convolute the overlapped Raman bands by a least square method.

By exciting solar cell devices with a chopper modulated light source, photocurrent intensities can be measured with a combination of a pre-amplifier (current-to-voltage converter, SR570) and lock-in (Stanford, SR 830) and then recorded by a LabView program.[153] Images can then be generated when collecting the current intensities and moving the translational stage at the same time. As shown on the right side of Figure 2.6, device performance can be correlated with polymer local conformations, which is significantly important for understanding the role of polymer structures and getting a better control of device efficiency.

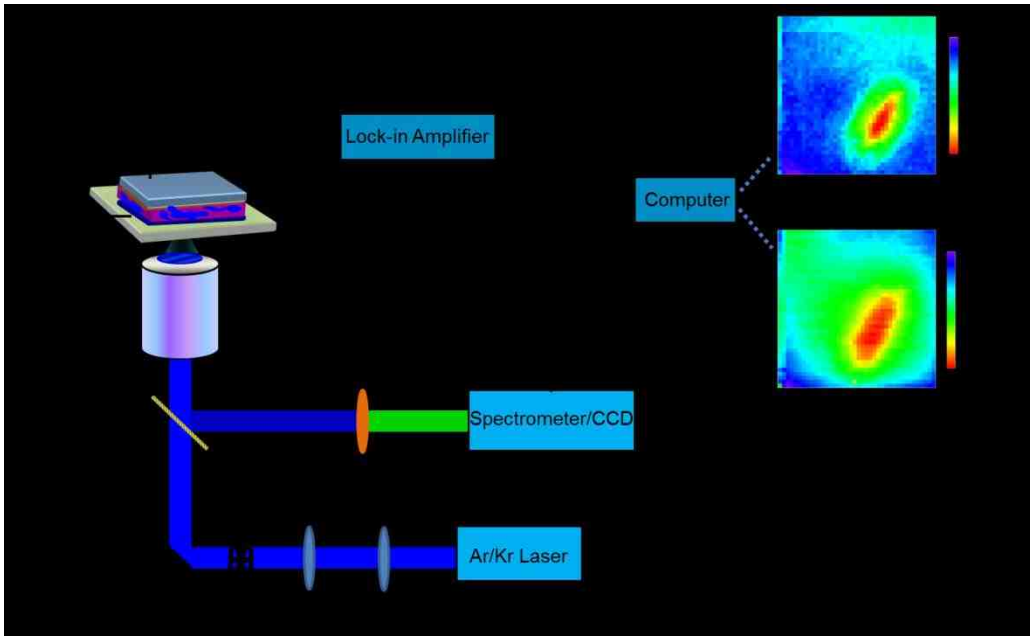

Figure 2.6 Schematic of resonance Raman and photocurrent imaging experimental setup.

2.1.5 Intensity Modulated Photocurrent Spectroscopy

Intensity modulated photocurrent spectroscopy (IMPS) is a technique that was first developed for studying charge transport and recombination dynamics in dye-sensitized solar cells, and some inorganic devices.[154,155] Many scientists have introduced this technique to study the polymer solar cell systems. Seminikhin's group first reported positive phase shift at low modulation frequency, which has been attributed to non-geminate charge recombination.[156] Recently, Luther's group introduced a drift-diffusion model for further explaining this behavior.[157]

In order to address main structural factors for dominant loss of the photocurrent, IMPS is used in this work. A 488 nm diode laser is used as the light source and controlled by LabView software. As illustrated in Figure 2.7, a 10% sinusoidal perturbation is added

on the steady state illumination. The device photocurrent and phase shift responses are modulated across a wide range of sweep frequencies (1 Hz to10 KHz) and measured by a Lock-in amplifier with the modulation frequency as reference. Frequency dependent photocurrent contains two components, real and imaginary, which can be also recorded by the Lock-in amplifier. The complex plot is based on the amplitudes of these two components with the modulated frequencies. IMPS images, which include photocurrent and phase shift images, are generated at some specific modulation frequency and recorded by a LabView program. Meanwhile, Raman imaging can also be performed over the same scan area as IMPS to identify spatial variations of material composition and conformation.

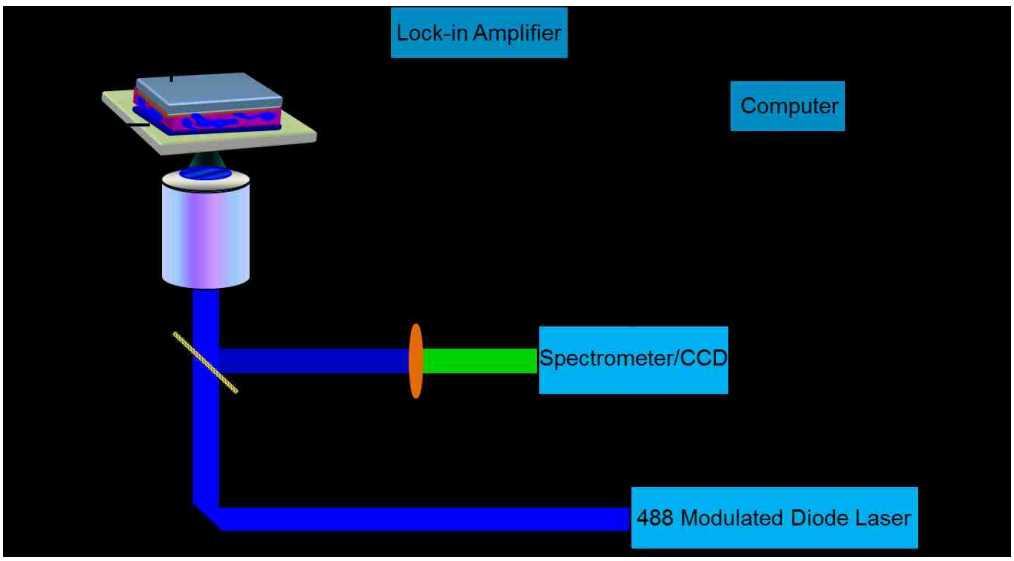

Figure 2.7 Schematic of IMPS and imaging experimental setup.

2.2 Sample Preparation

Sample preparation details for Chapter 3-7 are listed in the following, which include assembling water-soluble nanoparticles and encapsulated nanofibers, fabricating organic solar cell devices, and preparing samples for variable measurements.

2.2.1 Co-Polymer Nanoparticles Preparation

PFB (80–120 kDa) and F8BT (10–30 kDa) were purchased from American Dye Source (Quebec, Canada) and used without further purification. Nanoparticles were prepared using a mini-emulsion procedure described previously.[158] Briefly, polymer samples were dissolved in chloroform and blended in solution in equal amounts (w/w). The nanoparticle size was controlled by the weight fraction of the polymers in solution, i.e., 0.9% and 0.4% w/w for ~100 nm and ~58 nm particles, respectively. The blend solutions were mixed with an aqueous solution of sodium dodecyl sulfate (SDS, Sigma) of 2.4% w/w and stirred for 1 h to prevent agglomeration. The mixtures were then sonicated for 2 min and stirred at 60 ℃ to evaporate the chloroform. The resulting dispersion was then dialyzed to reduce the amount of SDS to ~5% w/w. Nanoparticles of both pure PFB and F8BT were fabricated using a similar procedure as controls. For comparison, PFB/F8BT particles were also fabricated using an aqueous reprecipitation approach but resulted in very large (>1 μm) size particles. Nanoparticles were then dispersed in an aqueous solution of polyvinyl alcohol (PVA, 4% w/w) for single particle spectroscopy studies.

Nanoparticles were characterized by UV/vis absorption, PL spectroscopy and atomic force microscopy (AFM). Ensemble UV/vis and PL spectra were measured from dilute aqueous dispersions (OD<0.1). Fluorescence imaging and spectroscopy of single

nanoparticles were measured, as described in Chapter 2.1.2. Nanoparticles were excited with various laser sources and spectra showed no dependence on excitation polarization. 405 nm light was used to excite both PFB/F8BT components nearly equally whereas 445 nm and 488 nm light were used to preferentially excite the F8BT component. PL images of PFB/F8BT nanoparticles in an argon gas flow cell were measured by raster scanning samples over a diffraction limited laser spot and fluorescence counts are recorded using an APD and multi-channel analyzer. Typical areal densities were ~0.075 particle/μm^2 and no fluorescence intermittency (flickering) was observed over the range of power densities used (~10-100 W/cm^2).

2.2.2 Encapsulated P3HT Nanofibers Preparation

P3HT NF and the block copolymer (BCP) molecules were prepared and characterized according to procedures described in the literature.[127,159-162] In a typical encapsulation experiment with a molar ratio of BCP:P3HT of 173:1, 800 μL of a 5×10^{-5} M stock solution of BCP in chloroform (concentration determined from UV-vis with an extinction coefficient of 4×10^4 M^{-1} cm^{-1}) was first dried under nitrogen. Then, a 10 μL aliquot of a ~10^{-5} M stock solution of P3HT NF's in toluene (concentration estimated from UV-Vis assuming an extinction coefficient of 1×10^4 M^{-1} cm^{-1} per monomer) was added to the dried BCP. After 20 minutes of mixing, either 1000 μL of water or 1000 μL of methanol were added to the solution. The assemblies were mixed for 15 hours and low flow of nitrogen was used to evolve residual toluene in the solution. After dissipation of any residual toluene, either methanol or water was added to the solution

until a final volume of 1 mL of solution was reached. In some cases, the superstructures were purified and concentrated by centrifugation at 1000 rpm for 45 minutes.

The NFs were characterized by transmission electron microscopy (TEM) imaging where the samples were prepared by placing a droplet of the NF solution on TEM grids. Solution dispersions of encapsulated NF structures were also investigated using optical absorption and photoluminescence (PL) spectroscopy. Samples were then drop-casted on clean glass coverslips for confocal spectroscopy and imaging, as described in Chapter 2.1.2.

2.2.3 Intercalated PBTTT/PCBM Thin Films

PBTTT-C_{14} (Mw=46 kDa, Mn=20 kDa, PDI=2.3, measured by GPC), PCBM, o-dichlorobenzene (o-DCB) were purchased from Sigma-Aldrich and used without further purification. All sample preparations were inside a nitrogen circulating glovebox. PBTTT-C_{14} and PCBM were dissolved in anhydrous o-DCB with 5 mg/ml, 20 mg/ml respectively. Solutions were heated for at least 8 hours at 100 ℃ and then filtered by 0.2 um filters (whatman) to remove any particulates. PCBM was added to PBTTT solutions in varying weight/weight fractions, i.e., 1:1 up to 1:8 (PBTTT/PCBM). Thin films of pristine PBTTT and PBTTT/PCBM blends were generated by spin-casting hot solutions at speeds of 600 rpm for 120 s onto rigorously cleaned glass coverslips inside the glovebox. The annealed films for absorption spectra in the formal text were achieved by heating the films under 140 ℃ for 20 min.

PBTTT/PCBM solar cells were fabricated using the optimal loading ratio reported in the literature (1:4 w/w). PEDOT:PSS (Sigma-Aldrich) was deposited onto indium-tin

oxide (ITO) substrates (Metavac) at 2000 rpm for 120 s and heated to 130 ℃ for 30 min to evaporate any residual water. PBTTT/PCBM thin films were next deposited at 600 rpm for 120 s and for annealed devices, thin films were heated on a hot plate under nitrogen at 150 ℃ for 5 min. Aluminum was then deposited under high vacuum by using a shadow mask with ~7 mm^2 for device area and current-voltage (I-V) characterization was carried out in the glove box in the dark and under AM1.5 illumination.

Raman spectra were measured under various excitation lines from argon- and krypton-ion laser sources (λ_{exc}=458, 647 nm; 2.71, 1.92 eV) as well as a NIR laser diode (λ_{exc}=780 nm, 1.60 eV). All spectroscopic measurements were carried out under inert environments and no significant differences indicating photoinduced sample degradation was minimal. Resonance Raman spectroscopic- and photocurrent imaging was next performed on both as-cast and annealed PBTTT/PCBM devices, as described in Chapter 2.1.4. Photocurrent images were generated using substantially lower excitation intensities than Raman images to avoid nonlinear effects, such as exciton-exciton annihilation or other photon-induced processes.

Raman spectra of a model PBTTT monomer were calculated at the B3LYP/SV(d) level of theory using the ORCA computational suite. The long C_{14} side groups were replaced with ethyl (C_2) groups and a fully planar pBTTT-C_2 monomer and a twisted variant in which the center fused ring is rotated with respect to the two thiophene rings by 29 degrees were simulated.[163] Resolution of Identity (RI-J) and Chain of Spheres (COSX)[164] approximations were utilized with the equivalent Def2-TZVP/JK quality auxiliary basis set. Atom pairwise dispersion corrections[165] with Becke-Johnson dampening[166] were employed.

2.2.4 P3HT with Charge Transfer Dopants

Electronic grade, regio-regular P3HT (Mw ≈ 50000-70000 g/mol), PCBM and F_4-TCNQ were purchased from Aldrich and used without further purification. Materials were dissolved in anhydrous chlorobenzene (CB) at a concentration of 10 mg/mL (P3HT, PCBM) and 1 mg/mL (F_4-TCNQ) and stirred for ~12 h in a dry nitrogen environment. Solutions were filtered using a 0.2 μm filter (Whatman) to remove any undissolved solids and spin-cast onto clean glass coverslips. F_4-TCNQ was added to pristine P3HT and P3HT/PCBM blend (1:1 w/w) solutions by addition of F_4-TCNQ solutions to achieve 0, 1, 3, 4.8, 9.1% w/w (dopant to polymer weight ratio) doping concentrations. The largest loading in pristine P3HT samples corresponds to equal amounts of polymer and dopant by weight (i.e., 50%). In PCBM blends, the weight ratio of P3HT and PCBM is kept constant and the amount of F_4-TCNQ is varied up to a maximum value of ~33% (i.e., equal amounts of each component). However, we emphasize lower amounts of dopant more commonly encountered in optoelectronic applications (i.e., <10%). Thermal annealing treatments of thin films were applied by heating samples on a hot plate at 130 ℃ for 20 min in a nitrogen environment. P3HT nanofibers (NFs) displaying H- or J-type aggregate characters were fabricated using self-assembly methods described previously.[127] F_4-TCNQ was added to solution suspensions of NFs to determine the stability of the structures to charge transfer doping.

Thin film samples were placed in an inert gas flow cell to avoid photodegradation and were excited using the 488 nm line of an argon ion laser with excitation intensities of ~10^3 (PL) and ~10^4 (Raman) W/cm^2. Samples were raster scanned during continuous

spectral acquisition and averaged. For the STEM/EELS imaging samples, P3HT of ~40,000 g/mol was used to increase the visibility of fibril-like structures. Solutions of P3HT/PCBM (1:1 w/w) mixed with 0, 0.5, 2, and 5% w/w with F_4-TCNQ in chlorobenzene. These solutions were then cast onto a glass substrate coated with poly(3,4-ethylenedioxythiophene): poly(styrenesulfonate) (PEDOT:PSS) and annealed on a hotplate at 150 ℃ for 5 minutes. The films were then floated off of the substrate and collected with a TEM grid. Images were collected in an aberration corrected JEOL 2100F microscope using a Gatan Imaging Filter (GIF) and the DigitalMicrograph software package. Spectrum images (SI) were obtained using a pixel size of ~ 4.5 nm. Sulfur maps were calculated from the SI using a power-law background subtraction and a 40 eV energy window beginning at 180 eV.

Density functional theory (DFT) calculations on charge transfer complexes were carried out using the hybrid B3LYP functional. A four-member unsubstituted thiophene oligomer, $(thiophene)_4$, was used to model P3HT. For F_4-TCNQ, $(thiophene)_4$, and their complexes, the standard 6-311++G** basis set was used. A sandwich structure involving one $(thiophene)_4$ and two F_4-TCNQ molecules was also simulated at the B3LYP/6-311+G* level that may represent possible complex structures encountered at high dopant loadings. The structures were first optimized, followed by the calculation of the Raman spectra. All calculations were performed using the Gaussian 09 suite.

2.2.5 Doping Efficiency Comparison Between R-Re P3HT and R-Ra P3HT

Electronic grade, r-Re (Mw ≈ 50000-70000 g/mol), r-Ra P3HT (Mw ≈ 50000-90000 g/mol), and F_4-TCNQ were purchased from Aldrich and used without further

purification. P3HT and F_4-TCNQ were dissolved in anhydrous chlorobenzene (CB) separately, at a concentration of 10 mg/mL (P3HT) and 2 mg/mL (F_4-TCNQ) and stirred for ~12 h in a dry nitrogen environment inside a glove box. Both solutions were filtered using a 0.2 μm filter (Whatman) to remove any undissolved solids.

For X-band EPR measurements of solution samples, 0.1 mL of P3HT solution (1 mg/mL) and 0.9 mL of CB were combined to generate the pure P3HT control. CB solutions of F_4-TCNQ (1 mg/mL) were combined with pure CB to obtain dopant loadings varying from 0% to 50.0%. Doped solutions were transferred into 1.5 mm diameter capillary tubes with a height of about 30 mm to ensure the comparable signal strengths for different solutions. For EPR spectra of solids, solutions were placed in EPR tubes and nitrogen was blown over the tube until all the solvent evaporated leaving a film.

For absorption and Raman measurements, P3HT concentration was fixed at 5 mg/mL while varying F_4-TCNQ loadings and samples were placed in quartz micro cuvettes (1 mm pathlength). Thin films for absorption measurements were prepared by spin-casting these solutions onto clean glass coverslips at 600 rpm.

P3HT/ F_4-TCNQ blend samples were also prepared with deuterated chloroform ($CDCl_3$) for ^{19}F NMR measurements keeping F_4-TCNQ concentrations constant at ~1 mg/mL while varying P3HT loading. Room temperature X-band EPR measurements were performed using a Bruker EMX EPR spectrometer. Each EPR spectra represent the average of 4 scans. Other instrument parameters are as follows: $\nu = 9.61396 \pm 0.00519$ GHz (2.1 mW), 1 G field modulation (100 kHz), receiver gain = 6320, time constant = 81.92 ms, conversion time = 20.48 ms.

Optical absorption spectra were recorded on a UV/vis spectrometer (Varian CARY 1C) in a scan range from 250 nm to 1100 nm. Raman spectra were measured by DXR 780 nm SmartRaman spectrometer (Thermo Fisher Scientific). ^{19}F NMR measurements were performed on a Bruker 300 MHz spectrometer. Standard fluorine parameters were used, signal was locked on $CDCl_3$ and spectra were attained from the average of 64 scans. The chemical shift was set with external standard, hexafluorobenzene (HFB).

Chapter 3

Spectroscopic Studies of Energy Transfer in Fluorene co-Polymer Blend Nanoparticles

(This chapter is based on the previously published article, Chemical Physics Letters, 2012, 522, 86-91.)

3.1 Introduction

The interface morphologies of donor/acceptor (D/A) conjugated polymer blends used in various thin film optoelectronic applications have a profound influence on the outcomes of photophysical processes that affect device performance.[39,167-173] For example, excited state charge and energy transfer rates and yields resulting in photocurrent generation in D/A blends can be tuned over a large range simply by varying the processing conditions of a blend thin film.[169,171] This tunability originates chiefly from minor fluctuations of the D/A interface structure (i.e., material miscibility, conformation and packing). However, most experimental studies of interface morphologies lack the ability to resolve features on the sub-100 nm size scale.

Here we study D/A polymer blend nanoparticles of poly(9,9-dioctylfluorene-co-bis-N,N-(4-butylphenyl)-bis-N,N-phenyl-1,4-phenylenediamine) (PFB) and poly(9,9-dioctylfluorene-co-benzothiadiazole) (F8BT) with nominal sizes of ~58 and ~100 nm using scanned probe and single particle spectroscopy techniques. Polymer nanoparticles are excellent model systems for understanding bulk heterojunction interface

characteristics and have also demonstrated promise for optoelectronic and sensing applications.[158,174-177] PFB/F8BT blend thin films have already seen extensive use as D/A polymer solar cell prototype systems that, while having relatively poor device performance, provide a useful platform for understanding morphology-dependent electronic processes, such as charge and energy transfer. The photoluminescence (PL) lineshapes and dynamics of PFB/F8BT blend thin films reveal useful insights into the interplay between interface morphology and the outcomes of these processes. For example, PFB/F8BT films cast from low boiling point solvents, such as chloroform, result in an intimately mixed phase with small scale phase separation (<100 nm). PL spectra and lifetime measurements of these films reveal a low energy, long-lived transition from an exciplex state that results from the recombination of polaron pairs following exciton dissociation.[39,171,173,178] On the other hand, deposition of PFB/F8BT films from high boiling point solvents, such as p-xylene, results in significant phase separation with clearly resolved domains on micron size scales and relatively high phase purity. PL spectra of p-xylene cast films lack emission from an exciplex state and are usually dominated by F8BT exciton emission due to efficient excitation energy transfer from the PFB component. From these ensemble PL trends, detailed correlations between local blend film interface morphology and material performance in device settings have been sought using scanned probe-based spectroscopic imaging techniques.[79,170,179,180] However, fundamental spatial resolution and chemical sensitivity limitations have made investigations of interface structure-function relationships on the sub-100 nm scale difficult.

Single particle spectroscopy of polymer blend nanoparticles can potentially offer new and unique insights into blend nanomorphologies by studying one particle at a time. Moreover, these studies will aid in determining the viability of these new functional polymer forms in various optoelectronic applications. For example, size dependent energy transfer[181] and electrochemical charging/discharging[182] have been reported in these nanostructure polymer forms which help bridge the gap in understanding of conformation-morphology dependent processes between single molecules and bulk films. For this purpose, we prepared PFB/F8BT nanoparticles using a mini-emulsion technique which allows for greater control of particle size unlike the more common reprecipitation method.[177,181,183,184] The mini-emulsion approach affords better size control of particles by use of surfactants that help arrest particle growth and prevent agglomeration. Because of the stochastic nature of the fabrication of PFB/F8BT nanoparticles, there are several candidate particle nanomorphologies that are proposed to exist as shown in Figure 1.1.

If particle formation kinetics are fast, then a uniform particle nanomorphology (i.e., small scale phase separation, ~10 nm) should result and PL spectra should exhibit an exciplex component. On the other hand, if solvent evolution is slow then both components can phase separate which should yield morphologies that are either partially or completely phase segregated. In this case, PL spectra should more closely resemble p-xylene films with only exciton emission from each polymer component. Single particle spectroscopy also allows for the determination of morphological heterogeneity by measuring PL spectra and decays from many particles.

The goal of this paper is to assess interface nanomorphology characteristics in PFB/F8BT blend nanoparticles and their impact on electronic processes such as charge

and energy transfer. Nanoparticle sizes were first determined by AFM followed by optical spectroscopy and single particle spectroscopy. "Small" particles have an average diameter of ~58 nm and "large" particles are ~100 nm. PL spectroscopy of PFB/F8BT particles reveals transitions from both PFB and F8BT components, the latter being much larger due to efficient energy transfer from the former. PL spectra and lifetimes were similar for both sizes of particles and no discernible exciplex component was observed. Lastly, pressure-dependent PL spectroscopy was performed that produced large red-shifts of the dominant F8BT PL maxima with little change in apparent energy transfer efficiency and no emergent exciplex emission at higher pressures. These trends indicate appreciable phase separation of both components into relatively pure nanodomains that are similar for both nanoparticle sizes.

3.2 Results and Discussions

Figure 3.1a shows the chemical structures of PFB and F8BT (D/A, respectively) components that comprise the blend nanoparticles. Particle sizes were characterized by AFM techniques and Figure 3.1b,d show representative AFM micrographs of nanoparticles dispersed on glass. Figure 3.1c,e show the size distributions of large (~100±19 nm) and small (~58± 10 nm) nanoparticles that were corrected for tip broadening effects assuming a spherical particle shape. However, we cannot entirely rule out the possibility that deviations from this ideal shape occur (i.e., cylindrical distortions) when particles are deposited on substrates. The widths of the particle size distributions likely reflect polydispersity effects and each particle is expected to consist of a wide range of molecular weights.

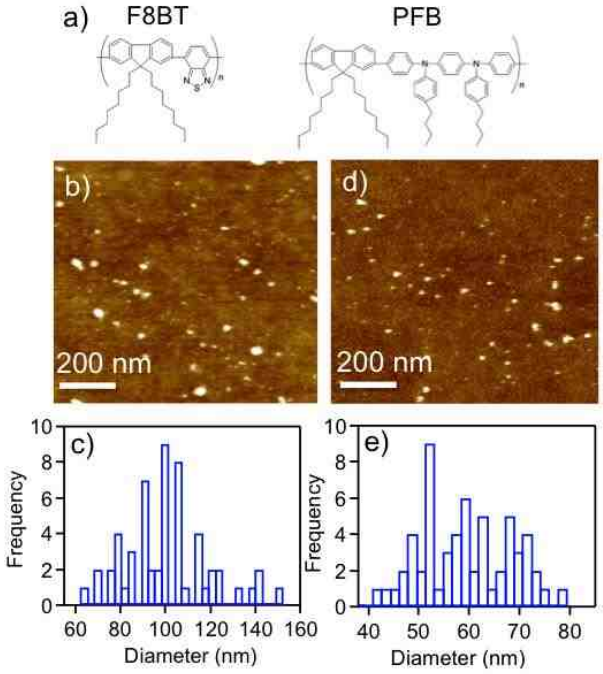

Figure 3.1 Chemical structures for a) F8BT and PFB, and AFM images and diameter histograms of F8BT/PFB blend nanoparticles, (b,c) for large particles (~100 nm) and (d,e) for small particles (~58 nm).

Optical properties of PFB/F8BT nanoparticle suspensions were next studied by PL and absorption spectroscopy. Figure 3.4a shows absorption spectra of ~100 nm and ~58 nm blend nanoparticle samples and single component nanoparticles. Absorption features of blend nanoparticles can be reproduced as linear combinations of single component spectra indicating no new ground state transitions upon blending due to either aggregation or charge transfer interactions. ~100 nm particles show broader linewidths and onsets possibly due to increased scattering of excitation light arising from the larger particle sizes. Small batch-to-batch variations were observed in absorption spectra where absorption spectra showed discernible changes (±10%) indicating variations in the

particle compositions (Figure 3.2). PL spectra of PFB/F8BT nanoparticles are shown in Figure 4.4b and appear virtually identical for both particle sizes and showed no batch-to-batch variation effects (Figure 3.3).

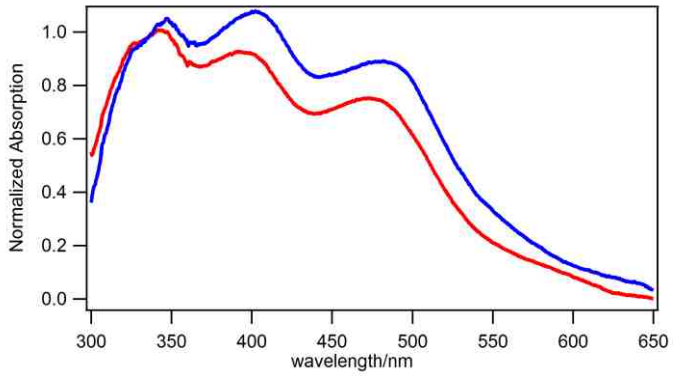

Figure 3.2 Absorption spectra for different batches of PFB/F8BT blend nanoparticles.

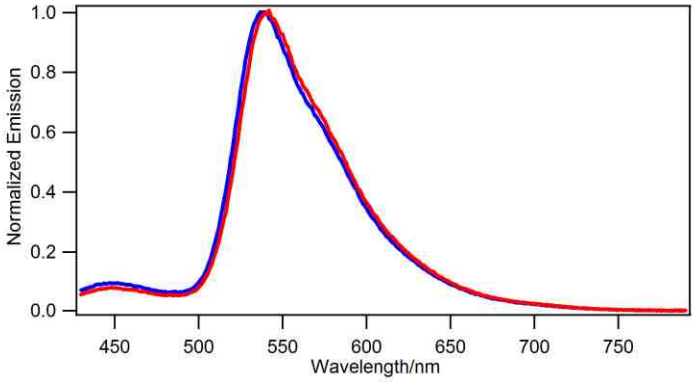

Figure 3.3 PL spectra for different batches of PFB/F8BT blend nanoparticles using 405 nm excitation.

The dominant feature in these lineshapes closely resembles the F8BT component (~15000-20000 cm^{-1}) with a small contribution from the PFB component on the high-energy onset of this transition. Importantly, PL spectra of blend nanoparticle dispersions showed no evidence of exciplex emission. Based on previous spectroscopic and scanned

probe studies of PFB/F8BT blend thin films cast from low- and high-boiling point solvents, blend nanoparticle PL spectra more closely resemble the latter where both components are highly phase segregated. In this regime, PL spectra should exhibit a dependence on excitation wavelength since preferential excitation of the acceptor should not result in energy transfer to the donor. Indeed, PL generated with >450 nm (~22000 cm^{-1}) light show no contribution from the PFB component which is expected since the absorption transition onset for this component is ~24000 cm^{-1}. On the other hand, excitation wavelengths <450 nm showed minor contributions from PFB likely due to excitation energy transfer.

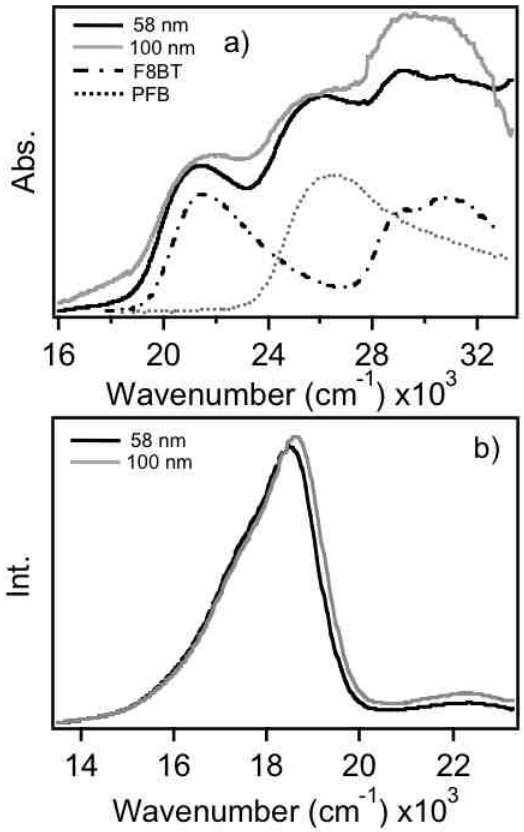

Figure 3.4 a) Absorption spectra of F8BT/PFB blend nanoparticles: black lines for smaller blend particles (~58 nm), gray lines for bigger blend particles (~100 nm), dashed black and gray lines are the absorption spectra for pure F8BT and PFB nanoparticles, their concentrations are roughly the same. b) F8BT/PFB blend nanoparticle ensemble PL spectra for ~58 nm particles (black) and ~100 nm particles (gray).

For comparison, PL spectra were measured by blending single component PFB and F8BT nanoparticles in equal proportions in aqueous solution (assuming similar extinction coefficients). Excitation of single component blend solutions at 405 nm produced spectra with a substantially larger contribution from the PFB component which reflects the relative PL yields of both polymers at this wavelength in the absence of Förster-type energy transfer (Figure 3.5). These results demonstrate that efficient excitation energy transfer occurs in blend nanoparticles suggesting a phase-segregated nanomorphology. We now use single particle spectroscopy to investigate energy transfer one particle at a time and uncover the extent of morphological heterogeneity present.

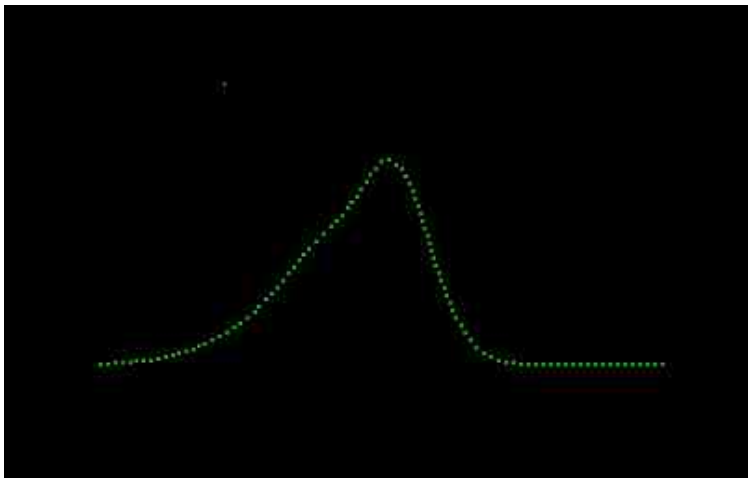

Figure 3.5 Single component F8BT (green dotted) and PFB (black dash-dot) nanoparticle PL spectra. A PL spectrum of a pure nanoparticle solution blend (black solid trace) is included for comparison.

Based on the size distributions shown in Figure 3.1, we likewise expect similar variations in composition and, hence, interface morphologies in PFB/F8BT nanoparticles. We first investigate the PL properties of single PFB/F8BT nanoparticles for ~100 nm and ~58 nm particles and representative images, linescans and transients are shown in Figure 3.6. Nanoparticles exhibit strong PL emission and are well-dispersed in the image field-of-view. Typical areal densities of these films were ~0.075 particles/μm^2 and no apparent agglomeration within the PVA matrix was observed. Linescan analyses (Figure 3.6b,d) revealed that spot sizes are diffraction-limited for both nanoparticle samples and the limit of resolution was estimated to be ~210 nm with 405 nm excitation light; close to the theoretical limit predicted by the Abbe rule. Furthermore, the average PL counts observed from both ~100 nm and ~58 nm particles were consistent with the size estimates determined from AFM for the same excitation power densities. From the volume ratio of these two particle sizes (assuming spherical shapes), the average amount of F8BT/PFB copolymers in ~100 nm particles should be ~4.6 that of ~58 nm particles. This is more apparent in PL transients (Figure 3.6c,f) recorded from single blend nanoparticles where PL counts from ~100 nm particles are ~3× higher than that of ~58 nm particles. Nanoparticles also exhibit extraordinary photostability with no apparent flickering or bleaching within the shot noise of the experiment. The high photostability and PL yields are similar to previous observations in related blend and single component

polymer nanoparticles and further demonstrate the potential of these systems as fluorescent reporters for imaging and sensing applications.[181,184,185]

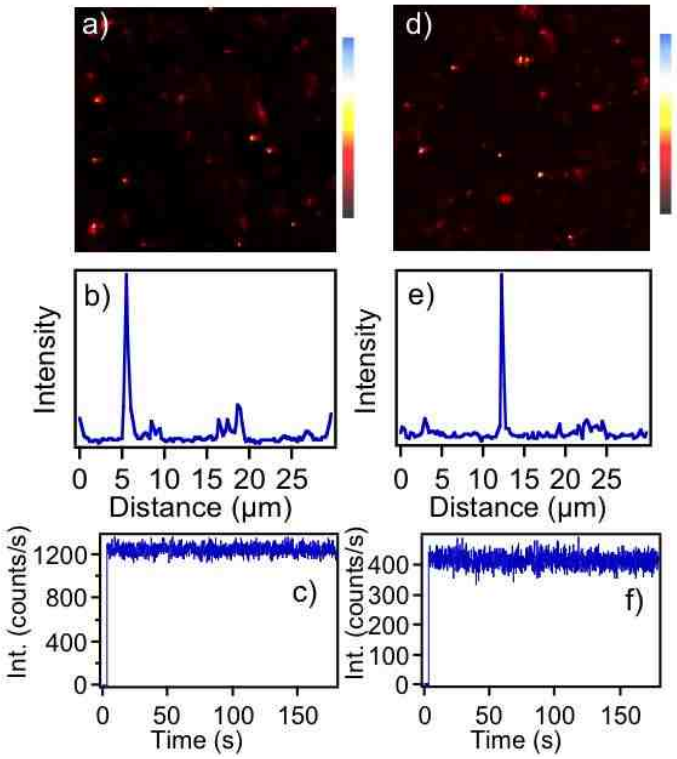

Figure 3.6 PL images, linescan and PL transients of F8BT/PFB blend nanoparticles, for ~100 nm particles (a, b, c) and ~58 nm particles (d, e, f). Scan range for images: 20×20 μm.

Because the heterogeneous nature of these nanoparticles, i.e., size and composition, is often masked in ensemble PL spectra (Figure 3.4b), we perform single particle PL spectroscopy to determine the extent of particle-to-particle heterogeneity. PL spectra of PFB/F8BT nanoparticles were recorded for over 50 particles. Figure 3.7a shows representative PL spectra of single PFB/F8BT nanoparticles for both sizes. PL lineshapes for both particle sizes are similar with the dominant contribution coming from the F8BT component and a smaller contribution from PFB. The size independent PL

lineshapes suggests similar nanomorphologies that likely arise from suppressed solvent evolution during nanoparticle formation. This feature leads to phase separation by spinodal decomposition into discrete nanodomains of PFB and F8BT. Similar nanomorphologies have been proposed in polymer/fullerene nanoparticles prepared from repricipitation methods where TEM images show distinct features from both components.[184]

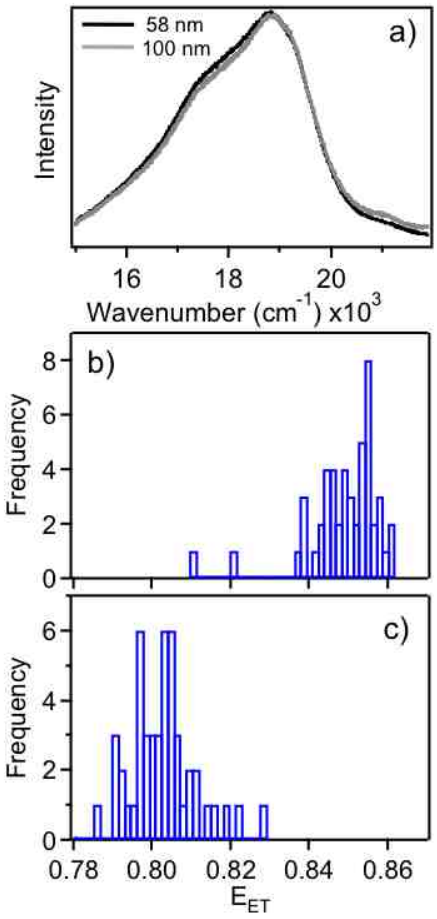

Figure 3.7 a) Representative single particle spectra of ~58 nm (black) and ~100 nm (gray) PFB/F8BT nanoparticles. Energy transfer efficiency (ETE) histograms for ~58 nm (b) and ~100 nm (c) nanoparticles.

Based on ensemble and single particle spectroscopy of the PFB/F8BT nanoparticles, efficient energy transfer occurs from the PFB (donor) component to the F8BT (acceptor) component which should be strongly dependent on the particle nanomorphology. We now analyze single particle PL lineshapes to estimate energy transfer efficiencies by fitting blend nanoparticle spectra with the PL lineshapes generated from pure PFB and F8BT particles (see Figure 3.8). Importantly, PL spectra shown in Figure 3.7 were generated using 405 nm excitation that excites both PFB and F8BT components nearly equally.

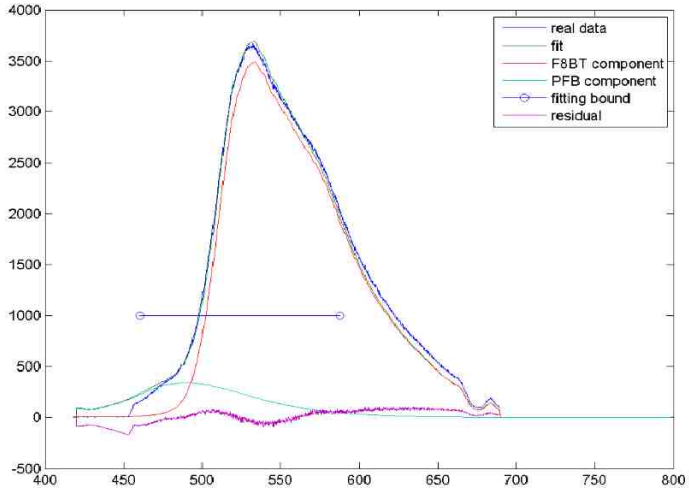

Figure 3.8 Deconvolution of single PFB/F8BT nanocomposite PL spectrum using pure F8BT and pure PFB lineshapes. The solid blue line defines the fit bounds.

Therefore, PL lineshapes represent contributions from both direct excitation of the F8BT component as well as energy transfer from the PFB component. These are accounted for using the following expression to estimate energy transfer efficiencies from PL spectra:

$$E_{ET} = \frac{I_A}{I_A + \frac{\phi_A}{\phi_D} I_D} \qquad (4\text{-}1)$$

where $I_{A,D}$ are the integrated PL intensities of the acceptor and donor components and $\phi_{A,D}$ are the intrinsic quantum yields, respectively. Experimental integrated intensities of single component PFB and F8BT nanoparticles of equal concentrations (estimated using optical densities) excited at 405 nm were used to estimate, which was found to be ~1.6 (Figure 3.5). This value is comparable to that expected from ratios of the known absolute PL quantum yields of F8BT and PFB (~0.5 and ~0.3, respectively). PL lineshape functions of single component PFB and F8BT particles were then fitted to blend nanoparticle PL spectra to determine both I_A and I_D. Figures 3.7c,d show energy transfer efficiency histograms for ~58 nm (a) and ~100 nm (b) size particles that show average efficiency values of ~0.85 ± 0.10 and 0.81 ± 0.08 for ~58 nm and ~100 nm size particles, respectively. The overall similarity of energy transfer efficiencies between both particle sizes is consistent with ensemble PL spectra results and further supports similar nanomorphologies for both particle sizes.

PL lifetimes of PFB/F8BT nanoparticles were also measured (Figure 3.9a,b) to better understand the nanomorphology picture borne out from ensemble and single particle PL spectra. Nanoparticle PL decay profiles were fit using iterative convolution techniques and found to be single exponential with average lifetimes of 800 ps ±60 ps for ~58 nm particles and 770 ps ±100 ps for ~100 nm particles. PL lifetimes were generated with 445 nm pulsed laser excitation which preferentially excites the F8BT component and contributions from the PFB component should be small (<5%). Previous PL lifetime measurements of pristine F8BT films yielded values of ~2 ns which are considerably

larger than those found in the blend nanoparticles. Since PFB emission cannot be excited, it is not possible to obtain reliable estimates of energy transfer efficiencies using lifetime data. However, PL decays can provide valuable insights into exciton dissociation at the PFB/F8BT interface and its dependence on particle nanomorphology. For example, Cadby et al. performed PL intensity and lifetime mapping studies of PFB/F8BT blend thin films cast from xylene that show micron scale phase separation.[186] These authors found that excitation of the blend film with 440 nm light resulted in PL lifetimes of ~340 ps indicating that F8BT exciton dissociation is larger in thin films probably due to lower phase purity. The longer average lifetimes in PFB/F8BT nanoparticles indicate that F8BT exciton dissociation is ~2× smaller possibly due to higher phase purity resulting in lower overall interface area.

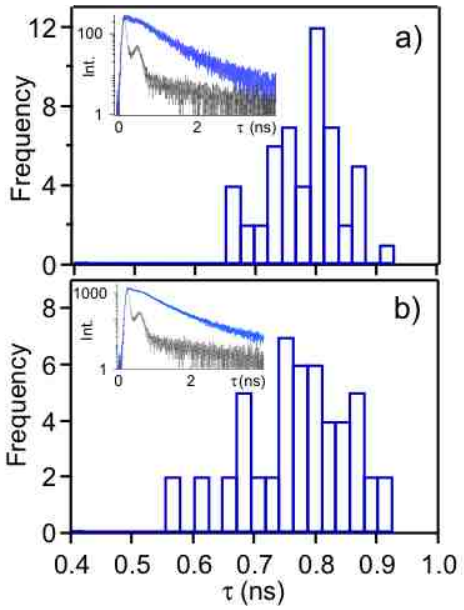

Figure 3.9 PL lifetime histograms of a) ~58 nm and b) ~100 nm PFB/F8BT nanoparticles. Insets show representative decay profiles (blue solid trace) and instrument response function (black dotted) for each type of particle.

Based on PL and lifetime trends, the morphologies of nanoparticles more closely resemble thin films cast from high boiling point solvents, such as p-xylene, where both components show appreciable phase segregation. In this case, lower interfacial area results in a loss of characteristic exciplex emission observed in films cast from low boiling point solvents and PL spectra are dominated by F8BT emission arising from efficient long-range energy transfer. However, the phase purities of both PFB and F8BT domains in phase segregated films are not 100% as seen from studies of film topographies.[187] To test our hypothesis of nanoparticle morphology and phase purity, we perform pressure-dependent PL spectroscopy to tune the morphology and packing within particles. If particles consist of intimately mixed D/A components then increasing pressure should favor greater interactions possibly leading to an exciplex emission. Figure 3.11 shows pressure-dependent PL spectra of PFB/F8BT nanoparticles excited with 405 nm light. A substantial red-shift of ~80 cm^{-1}/kbar was observed for the primary F8BT exciton emission and was independent of excitation wavelength (see Figure 3.10).

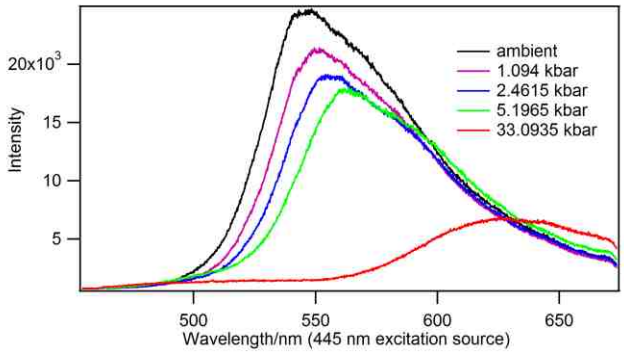

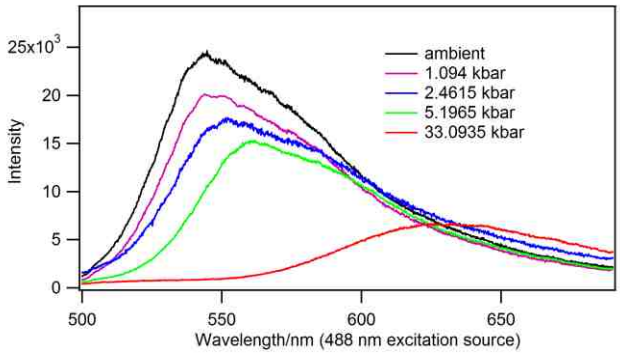

Figure 3.10 PL spectra for F8BT/PFB blend nanoparticles under hydrostatic pressure using 445 nm and 488 nm as excitation sources.

PL lineshapes also show considerable broadening at higher pressures which arises from increased inhomogeneity.[188,189] Importantly, no evidence of exciplex emission is observed at higher pressures indicating that both PFB and F8BT components are phase segregated and the phase purity of nanodomains is high. Similar to recent pressure-dependent PL studies on F8BT, increased pressure promotes efficient energy funneling to low energy sites although the maximum working pressure in this study was much higher (75 kbar) than used here. F8BT chains also become highly planarized with pressure resulting in greater delocalization of excitons and increased dielectric constants.[189] Based on the PL data from Figure 3.4-3.11, it is apparent that PFB and F8BT chains are nearly completely phase separated where planarization of F8BT chains is mostly unobstructed by the presence of interpenetrating PFB chains or nanodomains.

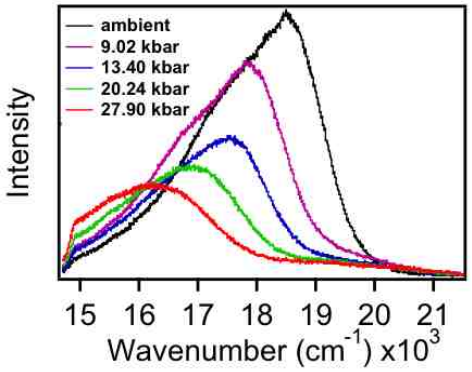

Figure 3.11 Pressure-dependent PL spectra of PFB/F8BT nanoparticles (λexc =405 nm).

3.3 Conclusion

PFB/F8BT nanoparticles were found to exhibit efficient and size-independent energy transfer. The PL lineshapes are similar to those published previously for PFB/F8BT films cast from high boiling point solvents where large scale phase segregation dominates. It is also apparent that the phase purity of each component within the nanoparticle is high which is confirmed by pressure-dependent PL spectroscopy. Based on energy transfer efficiency estimates for each candidate nanomorphology shown in Figure 1.1A, we propose that PFB/F8BT exist in partially phase segregated morphologies with domains in the size range of ~20-40 nm (see Figure 3.12). However, these estimates were generated using the simple point-dipole approximation of Förster theory which is not strictly valid for describing energy transfer in conjugated polymers. Nonetheless, the lack of size-dependent energy transfer strongly suggests identical nanomorphologies for both particle sizes (i.e., nanodomains of the same size). These results have implications for potential uses of polymer nanoparticles in optoelectronic

applications. For example, because particle nanomorphology is independent of size, reproducibility of material properties from batch-to-batch is ensured.

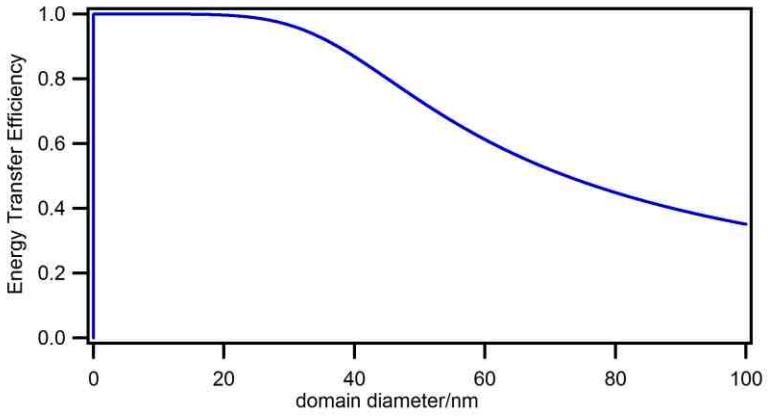

Figure 3.12 Energy transfer efficiency as a function of nanodomain size.

Chapter 4

Encapsulation of Poly(3-hexylthiophene) J-Aggregate Nanofibers with an Amphiphilic Block Copolymer

(This chapter is based on the previously published article, *Langmuir,* 2012, 28, 16401-16407.)

4.1 Introduction

Understanding the delicate interplay between intrachain order and interchain exciton coupling in π-stacked conjugated polymer aggregates is crucial for optimizing their performance in devices, such as solar cells.[153,159,190-192] This relationship manifests in aggregates of the conjugated polymer, poly(3-hexylthiophene) (P3HT), where subtle changes in chain conformation and packing can translate into large changes in exciton coupling characteristics.[193] Because aggregates promote efficient charge and energy (exciton) transport,[9,194-197] it is advantageous to understand the specific structural factors regulating electronic coupling in the close-packed chains comprising the aggregate. However, this is complicated in thin films due to the stochastic nature of solution processing techniques (i.e., spin-coating) and polydispersity effects resulting in randomly oriented aggregates, varying sizes, lower crystallinity and aspect ratios.

Solution-based self-assembly techniques have recently emerged as a promising strategy for effectively managing the order-disorder boundaries in P3HT aggregates by fractionating molecular weights.[160,198-201] Fractionation effectively lowers the polydispersity index (PDI) and allows aggregates to grow into nanofibers (NFs) with

large aspect ratios and a smaller amount of stacking faults. Furthermore, this approach permits fine-tuning of chain conformation and order which determine exciton coupling characteristics of P3HT aggregates. Spano and co-workers demonstrated that optical spectra of P3HT aggregates can be used to infer correlations between chain conformation (intrachain order, or, planarity of monomers) and packing characteristics on the type and strength of exciton coupling.[121,202] For example, comparison of 0-0 and 0-1 vibronic ratios provides a facile means to estimate the type and strength of exciton coupling where 0-0/0-1<1 and 0-0/0-1>1 indicate H- and J-aggregation, respectively.[121] The appearance of either aggregate type is determined primarily by intrachain order where low intrachain order results in increased interchain coupling and optical spectra resemble H-aggregates. Conversely, high intrachain order favors larger intrachain coupling and lower interchain coupling and spectra resemble J-aggregates.[121,203,204] Deposition of P3HT thin films by solution spin casting techniques does not promote molecular weight fractionation and, consequently, aggregate optical lineshapes appear predominantly H-like.[205,206] J-aggregate character is much more elusive in P3HT aggregates and usually only appears in samples with low polydispersity, high regio-regularity (>95%) and, most importantly, high intrachain order.[207] P3HT NF's self-assembled in toluene show pronounced J-aggregate character (i.e., 0-0/0-1 >1) originating from highly elongated P3HT chains with high intrachain order.[127] Temperature- and pressure-dependent spectroscopy studies of J-type NF's also demonstrated a high sensitivity of intrachain order to minor structural perturbations of the NF packing. For example, Niles et al. applied external pressures of up to ~20 kbar on NF's dispersed in solid solutions and pressure-dependent photoluminescence (PL) spectra showed a distinct change from J- to H-aggregate

behavior. This effect was attributed to a repacking of P3HT alkyl side groups from a type I to a type II arrangement, which causes the observed transition from J- to H-type behavior. Baghgar et al. also demonstrated that single P3HT NF's assembled in anisole can exhibit both H- and J-type emission suggesting multiple domains.[208] We now further investigate the influence of minor structural perturbations on the sensitive relationship between intrachain order and exciton coupling characteristics by encapsulating J-type P3HT NF aggregates using an amphiphilic block co-polymer (BCP), poly(3-hexyl-thiophene)-block-poly(ethylene-glycol), (PHT_{20}-b-PEG_{108}).

Kamps et al. recently used this BCP system to encapsulate H-type NF's of P3HT prepared from anisole solutions.[161] Unlike NF's assembled in toluene, anisole is a poor solvent and molecular weight fractionation is minimal. Intrachain order in these aggregates is correspondingly low, hence, the appearance of predominantly H-type character. Upon encapsulation by the BCP system, NF's retained H-aggregate character suggesting interactions between the NF and BCP molecules are minor and do not appreciably affect interchain exciton coupling.[161] Furthermore, it was demonstrated the encapsulated NFs assemble into secondary superstructures and take on branched and bundled morphologies depending on the choice of surrounding medium. Compared to variable pressure techniques, encapsulation of J-type NF's by BCP molecules represents a milder structural perturbation and thus provide an excellent means to explore the extent to which intrachain order can be tuned.

A key goal of this work is to ascertain whether interactions between the NF and BCP coating alter chain packing, intrachain order and, hence, exciton coupling in J-type NF's using optical spectroscopy and single particle PL spectroscopy. Additionally,

resonance Raman spectroscopy is performed on encapsulated NF superstructures to uncover changes to the structural integrity of the aggregate. Raman spectra reveal detailed overtone and combination transitions rarely observed in conjugated polymers that expose valuable insights into excited state geometry changes normally masked in optical spectra of P3HT aggregates. For example, non-zero exciton coupling leads to distortions of the optical lineshapes (i.e., attenuated or enhanced 0-0 transitions in H- or J-type couplings, respectively).[121] A time-dependent analysis of Raman intensities (fundamentals and overtones) is used to generate estimates of vibrational mode-specific excited state geometrical displacements (Huang-Rhys factors) independent of exciton coupling effects. This approach yields a more complete picture of the multi-mode excited state structural deformations of aggregated P3HT chains masked in conventional optical spectra.

4.2 Results and Discussions

We first begin by comparing nanoscale structural features of P3HT NF displaying H- and J-aggregate signatures in optical spectra that will later prove useful for correlating changes in exciton coupling upon encapsulation by the BCP system. Figure 4.1a shows a TEM image of NF's prepared from anisole and Figure 4.1b are assembled from toluene. The former consisted of P3HT chains with ~200 monomers whereas those assembled in toluene were fabricated from molecules with ~350 monomers, however, this difference in molecular weight has little impact on the type of aggregate formed. NF's formed in anisole are narrower (~20 nm widths) and have larger aspect ratios whereas those formed in toluene are considerably wider (~40 nm widths) with smaller aspect ratios. From

previous work, the former possess H-aggregate character with substantially smaller 0-0/0-1 ratios in absorption spectra and the latter exhibit pronounced J-aggregate character.[162,198] These results support the previously proposed structural attributes favoring J-type behavior in these NF aggregates whereby P3HT chains are much more elongated than in H-aggregates thus favoring increased intra-chain order.[127,152]

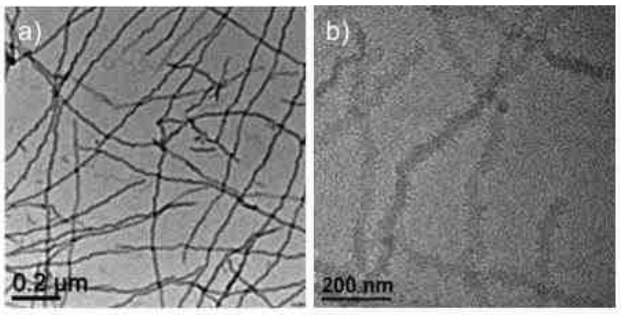

Figure 4.1 TEM images of pristine a) H- and b) J-aggregate NF's. H- and J-type NF's were prepared from anisole and toluene with average widths of ~20 nm and ~40 nm, respectively.

Figure 4.2 shows representative TEM images of encapsulated J-aggregate P3HT NF structures dispersed in methanol and water and cast onto TEM grids. Similar to previous work, two distinct types of secondary structures are observed, namely, branched and bundled.[161] Bundled assemblies of encapsulated NF are mostly observed for samples dispersed in methanol whereas branched structures are obtained for those dispersed in water. However, comparison of the structures shown in Figure 4.2 to those obtained by Kamps et al. for H-aggregate type NF's show smaller aspect ratios which may arise from instability of the J-aggregate structure in the NF growth direction (i.e., in the direction of the π-stack). To test this hypothesis, solution dispersions of J-type NF's were subjected to

sonication treatments that resulted in smaller aspect ratios (Figure 4.3) but retained J-aggregate character. Similar findings were obtained by Niles et al., namely, aspect ratios of J-aggregate NF's decrease upon dilution into inert host matrices but J-type behavior is preserved. Although TEM studies are helpful for understanding basic packing characteristics of NF's within the secondary superstructures, they cannot reveal how intra-chain order and inter-chain coupling are affected by encapsulation.

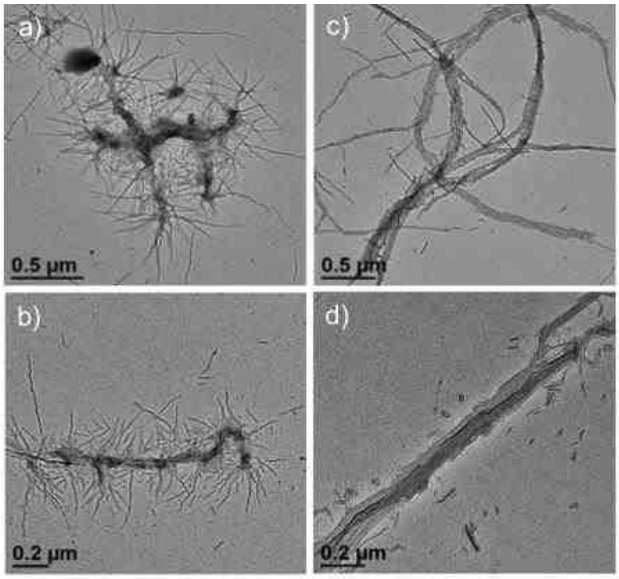

Figure 4.2 TEM images of branched (a,b) and bundled (c,d) encapsulated P3HT NF superstructures.

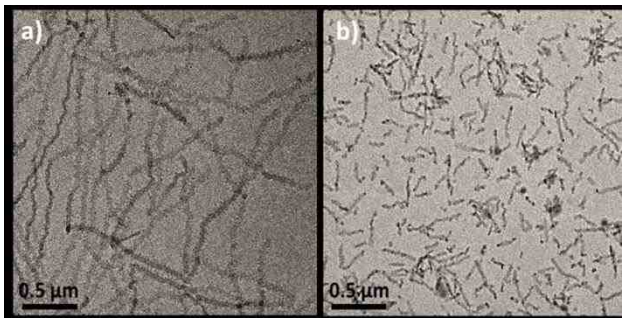

Figure 4.3 TEM images of toluene NF's a) before sonication and b) after sonication.

Optical absorption and PL spectroscopy are used to estimate exciton coupling characteristics of encapsulated NF's through the partially resolved vibronic transitions. Figure 4.4a shows optical absorption spectra of pristine P3HT NF J-aggregates (red dotted trace) and aggregates of the amphiphilic BCP (blue solid trace). The absorption lineshapes of the NF's appear identical to those published previously and those of the BCP resemble H-aggregates.[127,161,208] Figure 4.4b shows absorption spectra upon encapsulation for both water and methanol dispersions. Lineshapes display predominant H-type tentatively indicating intrachain order is lower in the encapsulated NF's. Spectral linewidths also become larger in encapsulated samples suggesting increasing inhomogeneity.

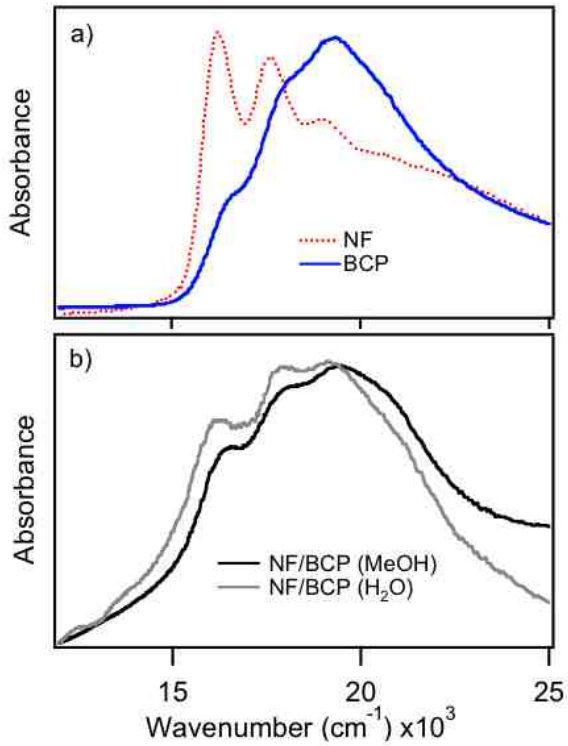

Figure 4.4 a) Absorption spectra of pristine P3HT NF (red dotted trace) in toluene and BCP in methanol (blue solid trace). b) Absorption spectra of encapsulated NF dispersed in methanol (black) and water (gray).

Despite distinctly different absorption lineshapes of encapsulated NF's from their pristine spectra, it is difficult to quantify the change in exciton coupling since BCP molecules also aggregate when coating the NF's. Absorption vibronic intensity ratios, therefore, are not reliable for determining changes in exciton coupling strength in the encapsulated NF's. Ensemble solution phase PL measurements were performed on both types of encapsulated superstructures but yields are very small making it difficult to obtain reliable estimates from analysis of ensemble optical lineshapes. This result suggests that NF emission is probably quenched by efficient excitation energy transfer to the BCP coating which exhibits weak PL signals (Figure 4.5).

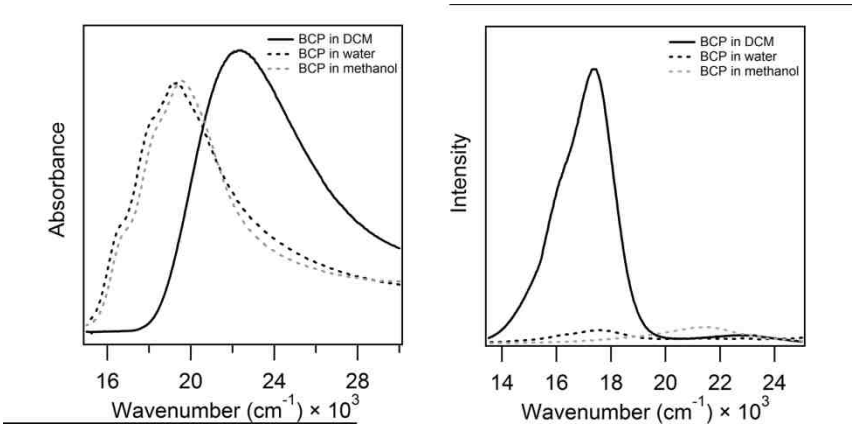

Figure 4.5 UV (left) and PL (right) for BCP in dichloromethane (black line), water (black dash line) and methanol (grey dash line) at same concentrations.

We overcome the issue of weak PL yields of encapsulated NF's by using confocal PL imaging capable of single photon detection with far greater sensitivity than ensemble PL measurements. Figure 4.6 shows representative PL spectra and images from both branched and bundled encapsulated NF superstructures generated with 488 nm excitation. PL and optical images are displayed in Figure 4.6a,b demonstrating evidence for both diffraction-limited and larger (>1 μm) particle sizes. PL spectra of bright spots show higher energy and broad lineshapes resembling amorphous (disordered) P3HT chains (Figure 4.6c inset). Since these types of lineshapes do not appear in solution phase ensemble PL spectra, we suspect that BCP molecules agglomerate during spin casting which is reasonable due to the large excess used in the encapsulation process. Corresponding optical images demonstrate that weaker PL spots correspond to the encapsulated NF's that appear to agglomerate when cast on bare substrates. Representative PL spectra of these individual superstructures are shown in Figure 4.6c for branched (blue dotted) and bundled (blue solid) structures. Compared to pristine J-aggregate NF lineshapes, encapsulated NF's from both dispersions appear H-like where the 0-0 intensity is slightly smaller than the 0-1 sideband. We estimate that PL yields are ~10-20% of that of pristine NF's from comparison of PL images generated under the same excitation conditions. This unexpected reduction in J-type NF PL intensity confirms efficient energy transfer to non-emissive traps probably on the BCP coating.

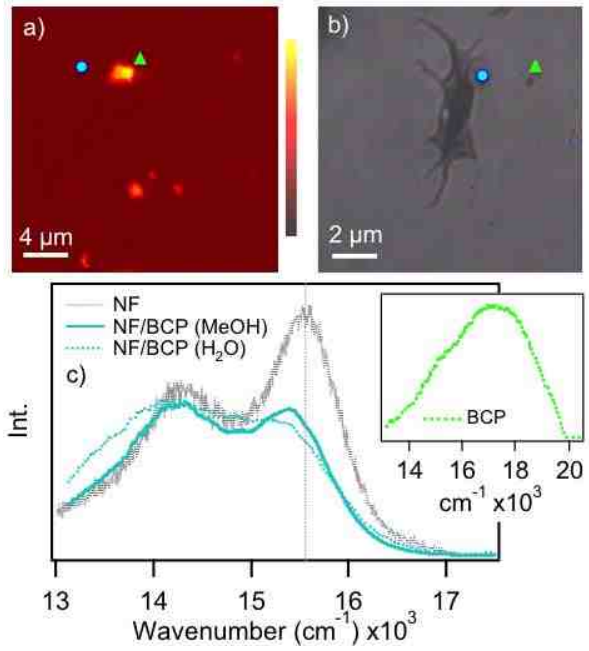

Figure 4.6 a) PL and b) optical images of encapsulated NF samples. Green triangles and blue circles denote amorphous BCP agglomerates and NF superstructures, respectively. c) Ensemble averaged PL spectra of branched (dotted blue trace) and bundled (solid blue trace) NF superstructures. A representative PL spectrum of pristine NF's is shown for comparison (black dotted trace). Inset: PL spectrum of amorphous BCP particles.

Based on absorption lineshapes of encapsulated NF's, it is tempting to infer a change from J- to H-aggregate behavior which would suggest that indeed encapsulation induces a small perturbation of NF intrachain order. However, closer inspection of the encapsulated NF PL lineshapes reveals discrepancies in the vibronic intervals, namely, a non-constant progression frequency across the lineshape. This effect is most apparent when comparing lineshapes between pristine and encapsulated NF's where the 0-0 maximum of the latter appears ~100-200 cm^{-1} lower in energy. The low energy regions

of both branched and bundled NF superstructures, on the other hand, overlap well with the pristine NF PL lineshapes. We attribute the discrepancy of the 0-0 transition to self-absorption that is especially problematic for J-aggregate emitters due to their smaller Stokes shifts and normally higher PL yields. The chief reason for this effect lies in the fact that encapsulated NF's are in very close proximity (see Figure 4.2) leading to effective high local concentrations. Similar effects were also reported in recent spectroscopic and scanned probe imaging studies of oligothiophene aggregates that show a range of both H- and J-type PL lineshapes.[209] PL lineshape distortions from self-absorption occurs in ~80% of all particles studied, making it difficult to reliably estimate changes in exciton coupling using the PL 0-0/0-1 vibronic peak intensity ratios. Additionally, the appearance of an amorphous PL component in images and spectra (Fiure 4.6a) may indicate a loss of NF structural integrity (aggregated P3HT chains) or excess BCP. To better understand possible changes in the NF structure upon encapsulation, we use resonance Raman spectroscopy which is highly sensitive to local (molecular-level) structure and packing of P3HT chains.

Previously, Gao et al. demonstrated the usefulness of resonance Raman spectra to discern the relative amounts of aggregated (i.e., well-ordered π-stacked chains) and amorphous (i.e., disordered or, solution-like) chains in P3HT systems.[152] Namely, Raman bands of the C=C symmetric stretching mode of the P3HT backbone show contributions from both aggregated and amorphous chains with characteristic frequencies of ~1450 cm^{-1} and ~1470 cm^{-1}, respectively. Because of the linear relationship between Raman intensity and concentration of scatterers, the relative integrated intensities of both species reveal their relative amounts in the sample. Despite the inconclusive nature of

changes in exciton coupling from both absorption and PL spectra, the significant loss of PL intensity in encapsulated NF's permits the measurement of resonance Raman spectra without large PL background interference normally encountered in P3HT J-aggregates.[127] If the amorphous PL signal observed in confocal imaging originates from increased amorphous regions in NF structures or partial dissociation then it should be apparent in resonance Raman spectra, i.e., lower relative intensity from the aggregated contribution and increase in the amorphous component.

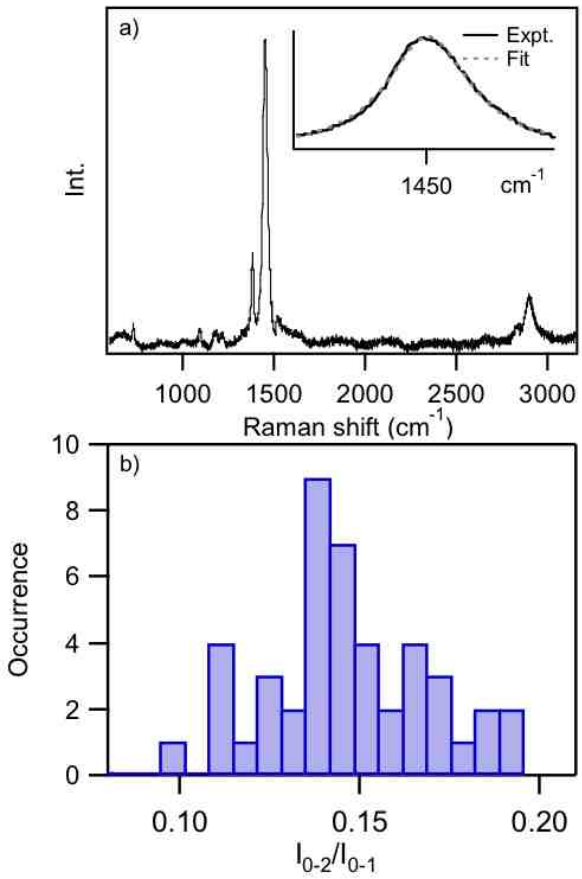

Figure 4.7 a) Resonance Raman spectrum of encapsulated NF superstructures showing the first overtone region. Inset: C=C stretching band of P3HT with Lorentzian fit. b) Histogram of first overtone (0-2) and fundamental (0-1) intensities of the C=C mode.

Figure 4.7a shows a representative Raman spectrum from an encapsulated NF superstructure and spectra from either branched or bundled structures yielded similar patterns. This result is expected since Raman is not capable of discerning exciton coupling but, rather, only changes in polarizabilities of chemical bonds due to changes in local environments (i.e., aggregation) of P3HT chains. Inspection of the dominant C=C lineshapes shows no evidence for an amorphous contribution at ~1470 cm^{-1} and can be reproduced well with a single Lorentzian function indicating only aggregated P3HT chains from NF. We conclude that contributions from amorphous P3HT in PL images and spectra originates from free BCP molecules not participating in the encapsulation of NF's. Moreover, the Raman scattering cross-sections of the BCP molecules are significantly smaller than P3HT at the excitation wavelength used (488 nm) which eliminates the possibility of substantial cross-talk in the measured Raman intensities (Figure 4.8).

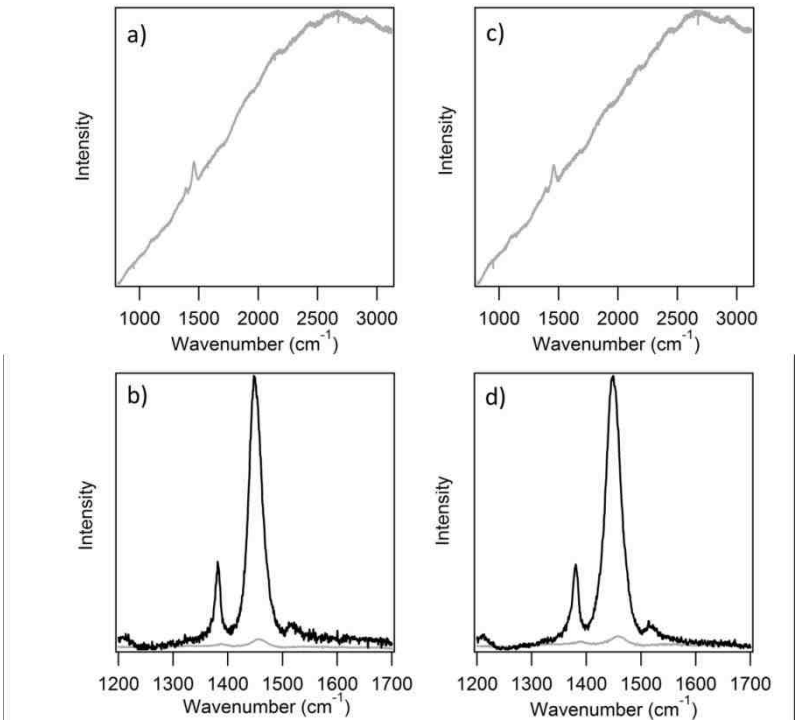

Figure 4.8 Comparison for the Raman spectra of BCP (grey lines) with the encapsulated NFs (black lines), a) and b) for BCP bulk film from water solution, c) and d) for BCP bulk film from methanol solutions. The experiments ran under the same condition and same setup in order to measure the effect of BCP to encapsulated NFs. The Raman signal for BCP is mainly taken over by the PL signal and it is much weaker than that of encapsulated NFs (~20 times weaker). Therefore, we can treat the Raman signal we got from encapsulated NFs only come from the P3HT NFs.

Perhaps the most noteworthy aspect of Raman spectra is the appearance of overtones and combination bands of the dominant C=C mode in the high frequency region. These features are rarely reported in conjugated polymers of this class and reveal important insights into the excited state geometries of aggregated P3HT chains. More importantly, Raman spectra are not susceptible to lineshape distortion effects encountered

in steady-state PL and absorption spectra due to exciton coupling effects and energy transfer. From Figure 4.7a, the first overtone of the C=C mode appears at ~2900 cm^{-1} and a combination band corresponding to one quantum of the C=C and C-C (~1380 cm^{-1}) modes at ~2840 cm^{-1} lower in intensity. Fundamentals of thiophene ring C-H stretches are also expected in this region (~2900-3000 cm^{-1}) but their activities are expected to be small since they do have significant displacements in the excited state (i.e., not resonantly enhanced). Indeed, comparison of resonance Raman spectra in Figure 4.7 with IR and off-resonance Raman spectra of encapsulated NF's showed no overlap or similarity in intensity patterns as the overtone-combination bands in Figure 4.7a (Figure 4.9).

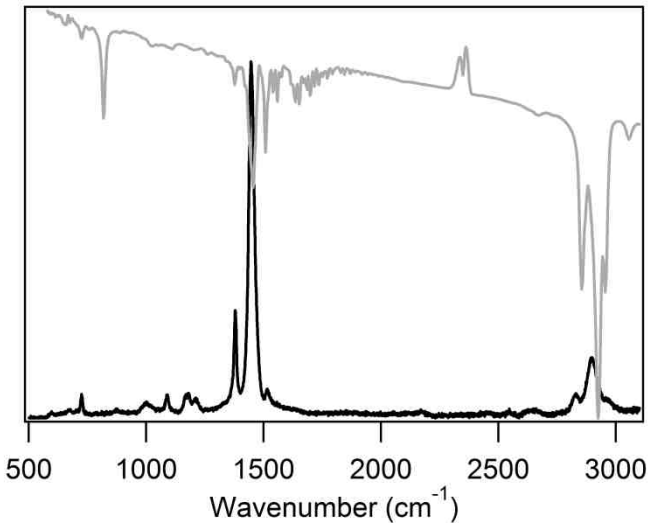

Figure 4.9 IR spectra (grey line) and the Raman spectra (black line) for BCP encapsulated NFs.

Because nonzero exciton coupling in aggregate structures results in non-Poissonian optical lineshapes, it is often difficult to determine how much vibrational displacements are affected by electronic delocalization within the π-stacks, i.e., exciton

bandwidths.[121] It is typically assumed that these displacements do not change significantly from ideal values determined from single oligothiophenes which can be been difficult to corroborate from optical absorption and PL spectra of P3HT aggregates.[121] Moreover, the low resolution of vibronic structure in optical spectra conceals contributions from other displaced modes and only the high frequency C=C mode is included in lineshape analysis procedures which can lead to overestimation of its actual displacement. To first gain a qualitative understanding of how much overtone features change between superstructures, we estimate the ratio of overtone (0-2) and fundamental intensities (0-1) of the dominant C=C Raman band which is related to its displacement.[130,132] Figure 4.7b shows a histogram of the 0-2/0-1 integrated intensity ratios for the dominant C=C stretch from individual encapsulated NF superstructures. The 0-2/0-1 values change by almost a factor of two indicating excited state geometrical deformations are sensitive to variations in local environments. However, there was also no appreciable difference in 0-2/0-1 values between branched and bundled structures demonstrating insensitivity to longer range interactions between neighboring NF's and the BCP coating.

Raman intensities in Figure 4.7 can now be analyzed to quantitatively estimate mode-specific vibrational displacements with the aid of the overtone-combination bands. We use the time-dependent theory of Raman spectroscopy developed by Heller, Zink and co-workers to calculate Raman intensities in Figure 4.7a.[130,132,210] Only modes with nonzero displacements contribute to the resonance Raman spectrum and the relative intensities reveal the slope, or, horizontal displacement of the potential minima between the ground and excited states. Nonzero displacements along high frequency vibrations

result in faster wavepacket motion on the excited state potential energy surface and larger Raman intensities. The Raman intensity, I_{i-f}, for each frequency can be calculated using Equation 1-6 and Equation 1-7, as discussed in Chapter 1. The scattering cross-section can be calculated analytically from the following assumptions: (i) no change in force constants between ground and excited states, (ii) harmonic potential energy surfaces, (iii) no dependence of the transition moment on normal coordinates, (iv) no coupling between normal coordinates. Under these assumptions, the autocorrelation is described by Equation 1-8 can be used to fit the experimental intensities by adjusting parameters for each mode until a good fit.

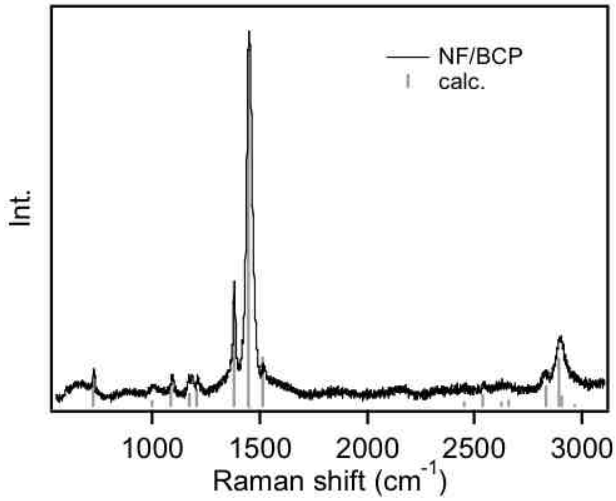

Figure 4.10 Experimental and calculated Raman spectrum of encapsulated P3HT NFs.

Figure 4.10 shows a representative fit with an experimental Raman spectrum of encapsulated NF's. The calculation reproduces experimental intensities very well including the overtone and combination bands. Calculated values of Δ_k and their standard deviations are included in Table 4.1 along with Γ and $E_{0\text{-}0}$ values, which can be verified

from optical lineshapes. Determination of multi-mode Δ_k values from resonance Raman intensity calculations now provides a more complete view of the excited state geometry changes in P3HT aggregates. For example, in calculations of P3HT aggregate optical lineshapes to extract exciton coupling strength it is typically assumed that the total Huang-Rhys factor ($S_k = \frac{1}{2}\Delta_k^2$) is ~1.0 (a typical value observed in large oligothiophenes) and does not change significantly when the chains form π-stacked aggregates. Furthermore, it is assumed that only the C=C mode is displaced (generally a good assumption) because this high frequency progression-forming mode usually dominates vibronic lineshapes. However, in delocalized electronic structures such as aggregates, the amount of nuclear displacement should decrease because sharing of electron density over a greater number of bonds. This is especially important for J-aggregates where increased delocalization along the individual chains implies the nuclear framework does not feel a change in electronic structure as much as in a localized system (i.e., oligomer or a single polymer chain). As shown in Table 4.1, estimates of Δ_k for the C=C mode are smaller than the typical reported value of ~1.4 which can be mostly explained by the inclusion of more displaced modes. In the typical single mode model analysis of aggregate optical spectra, linewidths must be arbitrarily increased to 'fill in' valleys between vibronic transitions. The validity of resonance Raman intensities to determine mode-specific Δ_k values can be appreciated from the relative timescales of PL and Raman processes. Namely, two-photon Raman transitions are virtually instantaneous thus producing a snapshot of the excited state geometry (Franck-Condon state) before the system relaxes into the emitting state geometry. Therefore, complementary optical and Raman spectroscopy measurements could, in principle, allow for accurate estimates of both

exciton and vibronic coupling which has been impossible owing to substantial exciton coupling-induced lineshape distortion effects. The only drawback to this approach is the possibility of overlapping states where interference can cause resonance de-enhancement effects, which would affect our Δ_k estimates. Because weakly resolved absorption spectrum corresponds to transitions from primarily aggregated P3HT chains, we assume interference effects are minor. Further exploration involving the generation and calculation of Raman excitation profiles is required to determine if the presence of close-lying excited states affect Δ_k values of the aggregate.

Table 4.1 Frequencies ($\hbar\omega_k$) and fitted mode-specific vibrational displacements (Δ_k) used to calculate Raman spectra including overtone-combination bands.

P3HT NF/BCP		
mode (k)	$\hbar\omega_k$	Δ_k
ν_1	726	0.45
ν_2	996	0.19
ν_3	1087	0.27
ν_4	1170	0.21
ν_5	1207	0.23
ν_6	1378	0.50
ν_7	1448	0.78
ν_8	1513	0.27

$E_{0\text{-}0}$ = 15540 cm^{-1}; Γ = 400 cm^{-1}; ω_I = 20492 cm^{-1}

4.3 Conclusion

Encapsulation of P3HT NF J-aggregates by amphiphilic BCP molecules results in the formation of hierarchical superstructures, similar to previous work involving encapsulation of H-type NF's. J-aggregate behavior is mostly preserved although distortions in optical spectra make it difficult to quantify changes in exciton coupling. The primary evidence for this claim comes from single particle emission spectra of encapsulated NF superstructures that, in the absence of self-absorption effects, yield similar lineshapes as pristine J-type NF's. This is further supported by resonance Raman spectra of encapsulated BCP-NF structures which indicate no loss of the structural integrity of the NF (i.e., aggregation state). Overtone and combination band transitions appearing in resonance Raman spectra are observed and analysis of intensities using the time-dependent theory of Raman spectroscopy permit estimations of vibrational mode-specific normal coordinate displacements, Δ_k. This result demonstrates that combinations of optical and Raman spectroscopic tools can be used to independently determine exciton and vibronic coupling terms of conjugated organic aggregates.

Chapter 5

Spatially Resolving Ordered and Disordered Conformers and Photocurrent Generation in Intercalating Conjugate Polymer/Fullerene Blend Solar Cells

(This chapter is based on the manuscript that is submitted.)

5.1 Introduction

The mixing of fullerene acceptors with conjugated polymer donors used for thin film BHJ solar cells has significant implications for determining morphologies and overall device performance.[97,211] Blends of PBTTT and PCBM are an ideal BHJ system for understanding molecular mixing characteristics and its implications on determining the outcomes of photovoltaic processes.[43,212,213] PBTTT chains readily assemble into well-ordered π-stacked lamellar crystalline structures,[214] essential for establishing multi-dimensional charge and energy transfer pathways. Extensive X-ray scattering and diffraction,[52,213-217] solid-state NMR spectroscopy,[213] differential scanning calorimetry (DSC),[212] and IR spectroscopy studies on PBTTT/PCBM blends have demonstrated the preponderance of fullerene intercalation into the polymer alkyl side groups resulting in bimolecular co-crystals.[217,218] PBTTT packing arrangements in blends are similar to pristine materials although lattice spacing and paracrystalline disorder in the π-stacking direction increase with fullerene intercalation that is marked by broadening in X-ray diffraction peaks and increased amounts of the gauche alkyl side group conformation.[213]

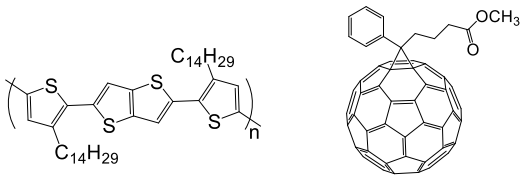

Figure 5.1 PBTTT (left) and PCBM (right) structures.

The PBTTT/PCBM system is especially useful as a model for predicting optimal blend stoichiometries and morphologies based on its tendency to form bimolecular crystals following a short annealing treatment of blend thin films. However, solar cell power conversion efficiencies are <4%,[219,220] well below current benchmarks.[221-223] This result is unexpected considering the high intrinsic charge mobilities of pristine PBTTT (>0.1 $cm^2/A/s$),[224-228] yet it underscores the need to better understand how ground state structure and interactions impact excited state photophysical processes.[21] Ultrafast pump-probe transient absorption spectroscopy (TAS) of PBTTT/PCBM blends has been used for this purpose and transients exhibit signatures of charge separation on timescales <1 ps followed by efficient geminate recombination of separated charge carriers occurring on timescales of ~200 ps.[229] These results are consistent with a well-mixed phase favoring efficient charge generation but separated carriers lack sufficient transport pathways and cannot escape Coulomb attractions thus recombining.[229,230] Importantly, X-ray spectromicroscopy studies of PBTTT/PCBM blends produced estimates of acceptor miscibility of 42 wt.%[216] implying that TAS dynamics are dominated by the mixed phase but contributions from other phases usually cannot be reliably filtered by this technique. Furthermore, spectroscopic and charge transport studies have shown compelling evidence of structurally similar PBTTT conformational polymorphs (conformers) with energy

differences of ~0.1 eV.[21,229] Intercalation-induced modulation of PBTTT conformers in PCBM blends undoubtedly impacts overall material performance but direct correlations between ground state structure and interactions with excited state charge transfer dynamics and material performance are more elusive.

In this paper, we identify new spectroscopic markers of structurally distinct PBTTT conformers in PCBM blends and spatially map their contributions to local material performance in solar cells. Resonance Raman spectroscopy and imaging of model PBTTT/PCBM solar cells reveal that intensities of the PBTTT alkyl-thiophene symmetric C=C stretching vibration (~1490-1500 cm^{-1}) vary with PCBM content as well as excitation energy. Two components are discernable and assigned as ordered (lower energy, "1"; $\hbar\omega_{C=C}$ = 1489 cm^{-1}) and disordered (higher energy, "2"; $\hbar\omega_{C=C}$ = 1500 cm^{-1}) PBTTT conformers. The 1489 cm^{-1} variant most likely corresponds to chains with greater backbone and side group order as expected for PBTTT chains in bimolecular crystals. Density functional theory (DFT) simulations and excitation energy dependent Raman spectra also indicate that alkyl-thiophene rings are more twisted in the disordered form. Disordered species are proposed to originate from well-mixed PBTTT/PCBM molecules but not as bimolecular crystals. Well-resolved overtone and combination transition intensities (up to 4 quanta) – chiefly involving the dominant PBTTT symmetric skeletal vibrations (~1400-1600 cm^{-1}) – are also apparent and intensities show much smaller sensitivity to PCBM loading indicating PBTTT excitations are electronically localized in nature for both species.

Spatial correlations between specific PBTTT structural forms, local composition and photocurrent production in functioning solar cell devices were established using

combined resonance Raman spectroscopic and photocurrent imaging techniques. A significant fraction of ordered PBTTT chains ("1") reside in PCBM-rich regions (i.e., crystallites) indicating these are indeed bimolecular crystals. However, corresponding photocurrent images show substantial losses in these regions likely caused by increased non-geminate charge recombination. This assignment is supported from intensity modulated photocurrent spectroscopy (IMPS) experiments and ensemble IMPS scans of annealed PBTTT/PCBM devices display signatures of non-geminate charge recombination, namely, positive phase shifts at low modulation frequencies (i.e., photocurrent leads the modulation frequency).[230,231] IMPS images of PBTTT/PCBM solar cells are reported for the first time showing that this process is most prevalent at ordered/disordered PBTTT boundaries. Overall, our combined Raman and photocurrent spectroscopy and imaging approach yields insights far beyond what is currently available from traditional characterization approaches by establishing new links between structural attributes of intercalation dependent conformers and their contributions to local material performance.

5.2 Data results and Discussions

5.2.1 Optical and Raman Spectroscopy

In general, conjugated polymers become more disordered as fullerene loading increases due to disruption of packing arrangements and reduced planarity between monomers.[164,232] In crystalline polymers, such as the archetype poly(3-hexylthiophene) (P3HT) system, addition of PCBM breaks up π-stacked lamellar chains in aggregates leading to increases in a solution-like amorphous component with higher energy and

featureless absorption lineshapes.[165,166] The ability of PCBM to intercalate into PBTTT chains presents an intriguing case and challenges traditional views of order/disorder transitions since PBTTT chains can form bimolecular crystals following an annealing step. Here, spectroscopic and electrical imaging approaches are used to; i) identify spectroscopic markers of intercalated and non-intercalated PBTTT chains in PCBM blends, ii) assess the structural and electronic properties in excited states, and iii) spatially correlate local composition and order/disorder characteristics to material performance in functioning solar cells.

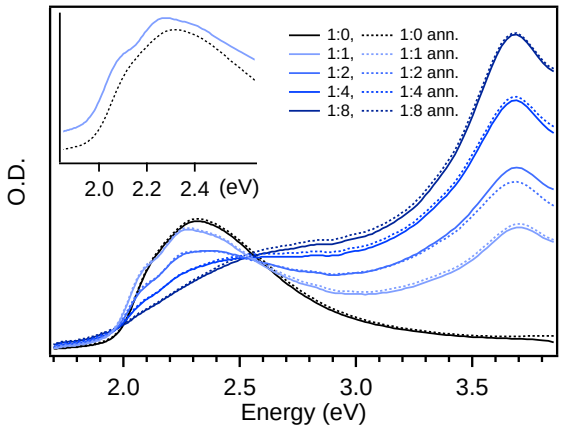

Figure 5.2 Optical absorption spectra of as-cast (solid traces) and annealed (dotted traces) PBTTT/PCBM blend thin films at several PCBM loadings. Inset: comparison of pristine PBTTT and a 1:1 w/w PCBM blend (offset for clarity).

We begin by re-examining the effect of variable PCBM content in PBTTT blend thin film absorption spectra which will be useful later for selection of resonance Raman excitation schemes (vide infra). Figure 5.2 displays as-cast (solid traces) and annealed (dotted traces) PBTTT/PCBM blend thin films with 1:1, 1:2, 1:4 and 1:8 w/w ratios. Improved spectral resolution of vibronic structure near the PBTTT absorption onset is

observed in addition to a slight red-shift (~0.04 eV) relative to the pristine PBTTT lineshape (see Figure 5.2 inset). As PCBM loading increases, the PBTTT contribution decreases concomitantly with an increase of a broad and overlapping higher energy component consistent with the PCBM absorption lineshape. Annealed blend spectra show relatively small change compared to as-cast films suggests that conversion from a disordered mixed (as-cast) phase to the bimolecular crystal phase is not as prominent as reported previously for higher annealing temperatures (i.e., approaching the liquid crystalline transition of PBTTT). Optical images of annealed blends, however, do show microscopic PCBM-rich crystallites (Figure 5.3).

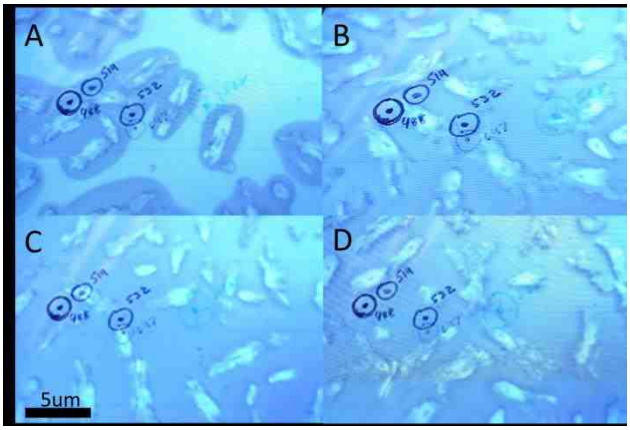

Figure 5.3 Optical images for PBTTT/PCBM blend films A) 150 ℃, 10 min, B) 150 ℃, 20 min, C) 150 ℃, 40 min, D) 150 ℃, 60 min.

PBTTT/PCBM blend absorption spectra in Figure 5.2 resemble previously published spectra in the singlet exciton onset region[213,215] but differ from other reports that show considerably lower PBTTT linewidths. The improvement of vibronic resolution upon PCBM addition and annealing has been attributed to bimolecular crystal formation constituting the bulk of the material. Although absorption spectra of our

PBTTT/PCBM thin films do show linewidth narrowing and red-shifts, the amount of bimolecular crystals is probably not as large as obtained by other groups. Gasperini and Sivula also recently showed that higher molecular weight PBTTT (>40 kDa) leads to entanglement of chains and rougher film textures that may inhibit bimolecular crystal formation in PCBM blends.[233] We speculate that the relatively larger molecular weight and PDI as well as lower annealing temperatures and other unintended variations in processing result in lower amounts of PBTTT/PCBM bimolecular crystals and, hence, lower resolution of absorption vibronic structure. Single molecule images and spectra of PBTTT diluted into a polystyrene host matrix were also recorded to verify if PBTTT chains were pre-associating in solution prior to blending with PCBM. Images show well-isolated, diffraction-limited spots and areal densities scale linearly with concentration (see chapter 8), which are not obtainable when agglomeration and gelling occurs. Importantly, the amounts and quality of bimolecular crystals in PBTTT/PCBM systems will vary depending on batch quality and processing conditions. Here, we seek to determine the range of PBTTT conformations accessible when PCBM intercalates which requires materials not completely converted to bimolecular crystals. Evidence of adverse intercalation-induced disorder effects on electrical properties in PBTTT/PCBM blends manifest as over an order of magnitude decrease of charge mobilities.[92,234] This dramatic decrease is believed to originate from twisted PBTTT backbones and side group disorder due to intercalated fullerenes. Solid-state NMR studies of PBTTT/PCBM blends support this view and found that ^{13}C and ^{1}H signals from the less-ordered gauche alkyl side group conformer, a minority species in pristine PBTTT (<10%), increase with PCBM loading.[213] Charge mobility studies of pristine PBTTT films predicted the energy

difference between the Fermi level and mobility edge to be ~0.1 eV.[229] A Franck-Condon analysis of pristine PBTTT absorption lineshapes also showed evidence of two distinct transitions with electronic origin transitions separated by ~0.1 eV,[21] in good agreement with electrical studies. The relatively small difference in energy between apparent intrinsic PBTTT structures complicates the use of absorptive spectroscopies for quantifying amounts and properties of these species since lineshapes strongly overlap and are more congested in PCBM blends. Consequently, PBTTT/PCBM structure/function relationships are incomplete owing to the mutually exclusive nature of ground state structural characterization and ultrafast excited state spectroscopies. Resonance Raman spectroscopy approaches potentially overcome these issues using selective resonant excitation schemes to target specific electronic excited states corresponding to distinct and PCBM-dependent PBTTT conformers and their populations. This feature permits sensitive investigations of ground state structure and interactions as well as exposing vibrational mode specific geometrical rearrangements incurred in optically accessible excited states directly involved in photovoltaic processes.

Figure 5.4 presents representative resonance Raman spectra of PBTTT/PCBM blend thin films excited with 514.5 nm (2.41 eV) light corresponding to the maximum of the PBTTT absorption lineshape. Resonance excitation usually leads to large enhancements ($\sim 10^5$-10^{10}) in Raman scattering cross-sections of the resonant chromophore. Contributions from PCBM in the excitation wavelength range used are absent demonstrating that PBTTT Raman cross-section enhancements overwhelm PCBM despite that it is usually present in larger concentrations (e.g., >1:1 w/w). Well-resolved progressions of overtone and combination bands, mainly involving the dominant PBTTT

C-C and C=C skeletal vibrations, are apparent. Comparison to IR absorption spectra of PBTTT/PCBM blends in the first overtone/combination band region (0-2) as well as the appearance of multiple progressions confirm these are not fundamentals of high frequency modes (i.e., C-H stretches).[213] Table 5.1 lists mode assignments of both fundamental and overtone/combination bands (for only the 0-2 region).

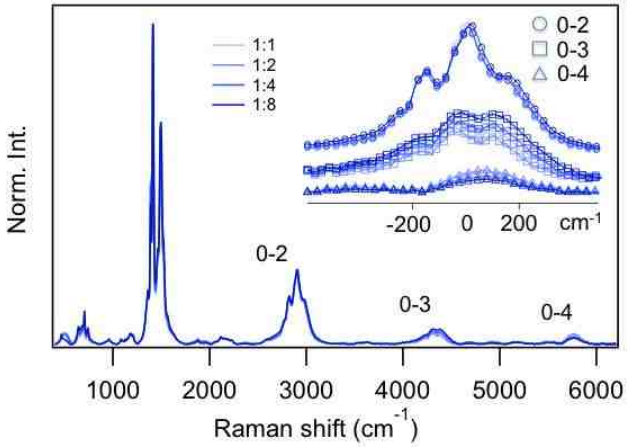

Figure 5.4 Resonance Raman spectra of PBTTT/PCBM blend thin films (excitation energy = 2.41 eV) with overtone/combination band transitions highlighted (inset).

Table 5.1 Assignments of main backbone Raman bands from PBTTT/PCBM blends in the fundamental (0-1) and first overtone (0-2) regions.

peak	frequency (cm^{-1})	Assignment
ν_1	1340	
ν_2	1365	
ν_3	1391	thiophene C-C stretch [a]
ν_4	1415	thienothiophene C=C stretch [a]
ν_5	1467	inter-ring thiophene C-C stretch [a]
ν_6	1489	thiophene C=C stretch [a]
ν_7	1500	
ν_8	1523	

ν_9	1563	
	2771	$2\nu_3$
	2804	$\nu_3 + \nu_4$
	2831	$2\nu_4$
	2876	$\nu_4 + \nu_5$
	2908	$\nu_4 + \nu_6$
	2934	$2\nu_5$
	2977	$2\nu_6; \nu_5 + \nu_7$
	3013	$\nu_6 + \nu_8$

[a]Determined from DFT simulations (see below) and Ref.[126]

We note that only the C-C and C=C symmetric stretches of the thiophene and thienothiophene backbone rings display pure overtone transitions. Higher order (>0-2) overtone/combination band clusters show greater broadening probably due to dispersion effects (i.e., wavepacket broadening) due to coupling between nuclear motions. Weak combination bands of multiple low frequency vibrations, likely corresponding to thiophene-thienothiophene ring bends and librations, are also apparent before the 0-2 region (~1700-2500 cm^{-1}). The appearance of multiple apparent progression forming modes suggests that vibrational displacements are large (i.e., large Huang-Rhys factors, $S = \sum_i^n \frac{1}{2}\Delta_i^2$, where Δ_i is the displacement for mode, i). However, PBTTT absorption linewidths (FWHM) are not significantly different than P3HT or other crystalline polymers (S~1.0)[235] meaning that the total vibrational displacements are probably similar. Raman lineshapes in Figure 5.4 also offer useful insights into PBTTT absorption features. Namely, the weakly resolved vibronic interval can be explained by the Franck-Condon displacement of multiple low frequency modes causing the 'valleys' between dominant mode progressions (i.e., the PBTTT CC backbone symmetric stretches, $\nu_{3\text{-}7}$) to become

filled in. Conversely, increased inhomogeneous broadening might also explain larger absorption vibronic linewidths but overtone/combination band intensities show very little sensitivity with increased PCBM loading meaning that either disorder is not important until longer times (several vibrational periods, >100 fs) or Raman chromophores are spatially localized (i.e., short coherence lengths). Typically, in large molecules with many displaced modes, overtone/combination intensities are usually extinguished before the first overtone (0-2) region due to destructive interference caused by rapid damping (dephasing) from strong coupling to the bath or amongst chromophores of different energies (inhomogeneous broadening).[236] This effect is suppressed in PBTTT systems and we speculate the persistence of the multi-mode overtone/combination band transitions in PBTTT/PCBM blend Raman spectra arises from weak coupling to the phonon bath and small contributions from inhomogeneous broadening effects.

5.2.2 Identifying Ordered and Disordered PBTTT Conformers

The qualitative picture emerging from Raman trends reported in Figure 5.4 is that the multi-dimensional excited state wavepacket survives for longer times allowing sufficient build up of overlap and overtone/combination intensities. This scenario is most consistent with localized excitations despite the relatively high order of PBTTT (even in PCBM blends) that intuitively suggest delocalized electronic structures. The implications of localization/delocalization in polymeric solar cells are significant and have been the subject of recent investigations of ultrafast charge separation.[121,130,237] For example, Jamieson et al. highlighted the importance of fullerene crystallites in promoting charge separation while simultaneously suppressing geminate in several polymer/fullerene

systems that show varying degrees of mixing.[237] We consider these aspects for interpreting Raman/photocurrent images described below.

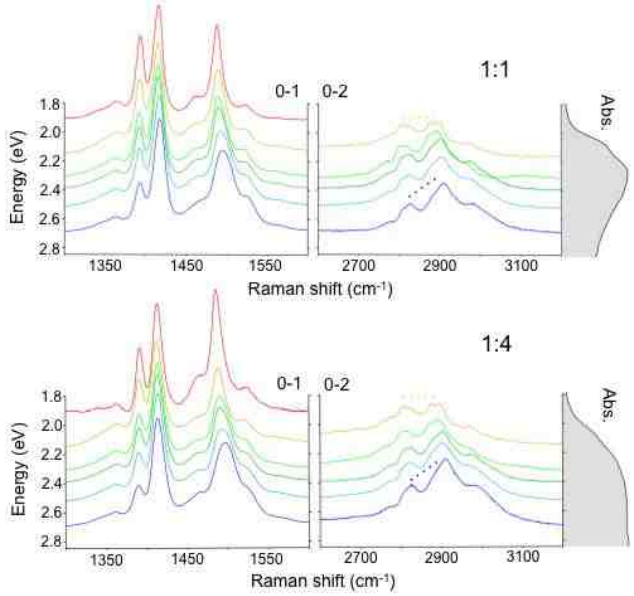

Figure 5.5 PBTTT/PCBM (1:1 and 1:4 w/w loadings) resonance Raman spectra as a function of variable excitation energies dis-played in the fundamental (0-1) and first overtone (0-2) regions of the main PBTTT backbone stretching modes. Corresponding optical absorption spectra are shown and dotted lines indicate changes in 0-2 intensity distributions.

Further insights into the nature of PBTTT chromophores PBTTT/PCBM blends can be obtained from resonance Raman spectra as a function of excitation energy spanning the PBTTT optical absorption lineshape (~1.9-2.7 eV) Figure 5.5 displays variable excitation energy Raman spectra and are normalized to the thienothiophene ring C=C symmetric stretch (1415 cm^{-1} mode, ν_4) for comparison. Raman patterns show significant changes with excitation energy consistent with resonant excitation of distinct PBTTT chromophores. In the 0-1 region, the relative intensity of the symmetric C-C

stretch of the thiophene rings (1391 cm^{-1}) decrease and the ~1489-1500 cm^{-1} band region of the symmetric C=C thiophene ring stretch gains in intensity in addition to apparent blue-shifting and broadening with increased excitation energies. Chromophore specific resonance enhancement is more obvious in the first overtone (0-2) region where increasing excitation energy causes intensity redistributions towards higher frequencies. Residual fluorescence masks overtone/combination bands in the background noise at the lowest excitation energy (647 nm, 1.92 eV) and these spectra were not included.

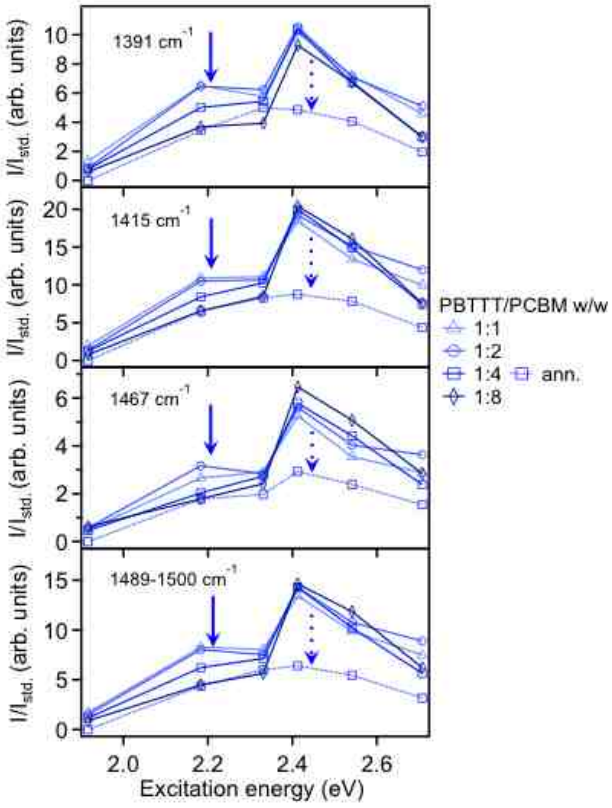

Figure 5.6 Raman excitation profiles (REPs) of the PBTTT back-bone symmetric stretching fundamental (0-1) region from variable PBTTT/PCBM loadings.

We propose that observed lineshape (intensity) changes with excitation energy reflect the presence of both ordered and disordered PBTTT conformations whose

populations are modulated by PCBM loading. Raman excitation profiles (REPs) are now constructed to test this hypothesis that reveal vibrational mode-specific views of the excited state potential energy landscape. Figure 5.6 shows REPs from as-cast PBTTT/PCBM films (solid traces) for all backbone skeletal vibrations showing appreciable intensity in resonance Raman spectra in Figure 5.4 and 5.5 (ν_{3-7}) and intensities are reported relative to a non-absorbing external standard (i.e., sapphire). Generally, REPs bear similarity to absorption lineshapes provided that Raman and absorption transitions involve only a single excited state (i.e., single absorber). REP lineshapes in Figure 5.6 show noticeable deviations from one-photon absorption spectra (Figure 5.2) confirming contributions from multiple states. In particular, a pronounced dip around ~2.35 eV is observed as well as increased activity (cross-sections) in the higher energy region of the main PBTTT absorption lineshape. As PCBM concentration increases, the relative intensities of the lower energy feature decrease for all mode-specific REPs reported. The dip at 2.35 eV results from the crossing of excited state potential energy surfaces of two states leading to destructive quantum interference and intensity de-enhancements.[238]

Based on the trends observed here and from previous studies, it is relatively straightforward to assign the low (high) energy REP feature to ordered (disordered) PBTTT chains. We do note that because of the amounts of PCBM used, PBTTT should always exist in a mixed phase owing to large cohesive energy densities between these molecules.[97,239] To verify if the PCBM loading dependent REP lineshapes originate from morphology-dependent PBTTT conformers, we measured REPs of an annealed 1:4 w/w PBTTT/PCBM blend and compare these to as-cast REP lineshapes (dotted traces, Figure

5.6). A pronounced decrease of the higher energy REP component is apparent indicating conversion to PBTTT chains with improved backbone and side group order consistent with intercalated bimolecular crystals. This result highlights the greater sensitivity of Raman techniques to chromophore environments compared to one-photon absorption spectroscopy (Figure 5.2) which can obscure contributions from closely overlapping states.

We now focus on the ~1489-1500 cm^{-1} region assigned to the C=C symmetric stretch of the thiophene rings ($\nu_{6,7}$, Table 5.1) that are particularly sensitive to PCBM loading and excitation energy (Figure 5.5). Figure 5.7a presents resonance Raman spectra generated from a PBTTT/PCBM blend thin film of a 1:2 w/w ratio in the thiophene C=C symmetric stretching fundamental region generated. Excitation at the PBTTT red absorption onset (i.e., 1.92 eV) selects the 1489 cm^{-1} (ν_6) component that subsequently blue-shifts and coalesces into the ~1500 cm^{-1} mode (ν_7) at higher excitation energies (i.e., 2.71 eV). These trends have been explained previously from theoretical studies of oligothiophenes where lower energy chromophores (viz. longer conjugation lengths) show red-shifted Raman-active backbone vibrations.[149] According to trends in REP lineshapes, the 1500 cm^{-1} mode derives intensity from disordered PBTTT C=C thiophene component due to fullerene intercalation-induced disorder among the alkyl side groups causing twisting of the backbone thiophene rings and paracrystalline disorder. Likewise, the 1489 cm^{-1} component of the symmetric thiophene C=C stretch is proposed to originate from ordered PBTTT chains in bimolecular crystals where side group and backbone order is improved. Linewidths of both PBTTT C=C thiophene forms are also consistent with their proposed structural origins, namely, ordered conformers are ~15 cm^{-}

[1] compared to ~25 cm^{-1} for disordered chains due to conformational heterogeneity. The relative amounts of these two PBTTT conformers (denoted as "1" and "2" for ordered and disordered PBTTT conformers, respectively) are estimated by deconvoluting the C=C thiophene band using two lineshape functions corresponding to the ν_6 and ν_7 bands (Table 5.1). We do not attempt to obtain absolute cross-sections for each species but it is expected that these values are similar owing to the structural similarity of ordered and disordered forms (i.e., energy difference of ~0.1 eV), which is much subtler than in P3HT. In this description, the total C=C thiophene Raman band is a linear combination of both components and we use this simple model to assess how the amounts of disordered PBTTT conformers, ($\frac{I_2}{I_1 + I_2}$), change with blend film processing conditions. The disordered component is effectively the precursor species to the ordered form in bimolecular crystals, which allows us to better understand the evolution which has not received much attention in the PBTTT/PCBM system. Figure 5.7b presents estimates of the disordered PBTTT content ("2") in as-cast blends, which increases with PCBM content and excitation energies. For comparison, ($\frac{I_2}{I_1 + I_2}$) values were determined for an annealed blend (1:4 w/w) and displayed in Figure 5.7b which has significantly less of the disordered PBTTT due to conversion into bimolecular crystals which is consistent with REP trends in Figure 5.6

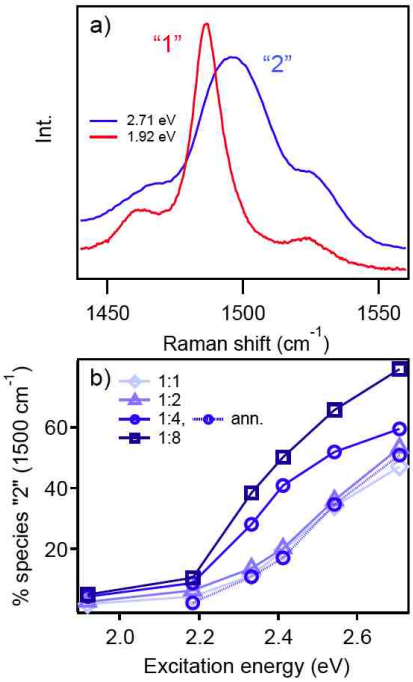

Figure 5.7 a) Resonance Raman spectra of as-cast PBTTT/PCBM blend thin films (1:2 w/w) showing lineshapes of the two distinct PBTTT forms; ordered ("1") and disordered ("2") PBTTT chains. b) Percent of species 2 present in all blend ratios as a function of excitation energy.

5.2.3 Theoretical Raman Simulations

DFT Raman simulations of a planar and twisted PBTTT model monomer system (PBTTT-C_2) are next performed to validate our proposed model and are shown in Figure 5.8 with their respective structures. Calculated DFT Raman lineshape trends agree very well with experiment although non-resonant conditions are used in simulations and a scaling factor of 0.95 must be applied to calculated frequencies in order to compare with experiment. The C-C symmetric stretch appearing at 1461 cm^{-1} for the planar conformation undergoes a blue shift of ~7 cm^{-1} in the twisted variant. Most notably, intensity redistributions occur between the inter-ring C=C symmetric stretch (1541 cm^{-1})

and the thiophene C=C stretch (1594 cm^{-1}) depending on backbone planarity. For example, the latter increase in intensity for the twisted PBTTT variant (2) whereas the former dominate in the planar monomer (1). Previous DFT simulations of planar and twisted PBTTT trimer structures show similar trends as presented in Figure 5.8[126] confirming that modulation of two PBTTT conformer populations occurs in PCBM blends. Moreover, calculated frequencies and intensities of trimers were very similar to experimental Raman spectra, suggesting that excitations are probably localized to a few monomer units.

Thus far we have shown that the ability of the two species model to decompose key Raman bands into separate contributions from morphology-dependent PBTTT conformers offers a much simpler means to assess order/disorder transitions in this system. Although the DFT simulations correctly predict experimental behavior, they do not allow us to incorporate side group disorder and paracrystallinity. It is also important to note that ordered PBTTT chains in bimolecular crystals are also twisted but side group and paracrystalline disorder is diminished. Most importantly, our approach now enables us to establish direct spatial correlations between the type and amounts of these specific conformers and their performance attributes in-situ within functioning devices.

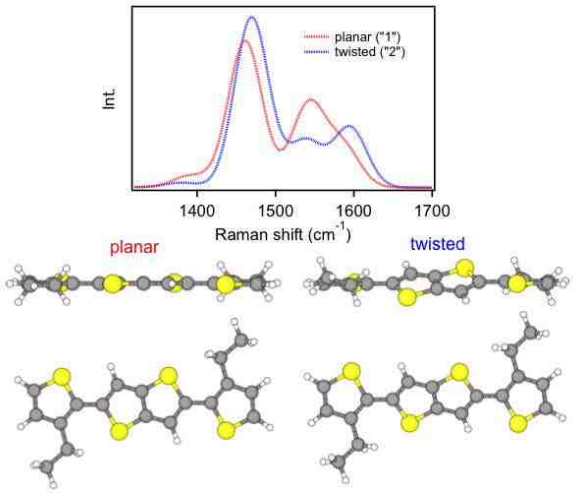

Figure 5.8 Simulated Raman spectra of the PBTTT-C2 monomer and structures.

5.2.4 Spatially Mapping Order-Disorder and Photocurrent Generation in Solar Cells

Resonance Raman spectroscopic and photocurrent imaging techniques are employed to spatially resolve how ordered and disordered PBTTT chains impact local device performance in model solar cell devices. For these experiments, as-cast and annealed PBTTT/PCBM blends in 1:4 w/w ratios (the optimal blend ratio reported for solar cells)[221,222] were prepared to compare morphology-dependent order/disorder spatial distributions. We emphasize annealed devices owing better material performance in addition to better contrast in Raman and photocurrent images. As seen from absorption and Raman spectra, we do not attain complete conversion to bimolecular crystals, which is advantageous spatially correlating the structure-function characteristics of the ordered/disordered structural variants present.

Figure 5.9 shows representative resonance Raman and photocurrent images of a 1:4 w/w annealed device and appreciable microscopic phase segregation is apparent

within the active layer. Raman images represent the ~1489-1500 cm^{-1} spectral region of the thiophene C=C stretches (indicated on the PBTTT structure diagram) and are generated using 458 nm (2.71 eV) excitation light. This excitation regime was specifically chosen to selectively interrogate disordered PBTTT chains (2) thereby directly assessing the role of morphology-dependent intercalation on local material performance (i.e., morphology-dependent charge transfer and recombination processes).[240,241] A tolerance of ±5% of the center frequencies is allowed for both species in our fitting procedure to obtain a good fit to morphology-dependent dispersion effects which become significant with greater phase separation (i.e., annealed devices). Figure 5.9a presents the total integrated intensity of the $\nu_{6,7}$ (1,2, respectively) modes and corresponding photocurrent over the same area is shown in Figure 5.8b. Lower PBTTT intensity represents PCBM-rich areas, but an appreciable amount of PBTTT still exists in these regions. Photocurrent images (Figure 5.9b) show much lower output in PCBM crystallites than the rest of the film probably originating from unbalanced charge transport.[242,243] The PBTTT C=C stretch can now be decomposed into contributions from the ordered and disordered components discussed previously. Figure 5.9c,d show fractional composition images of each PBTTT form revealing that PBTTT chains in PCBM-rich regions exists predominantly in the ordered form consistent with bimolecular crystals.

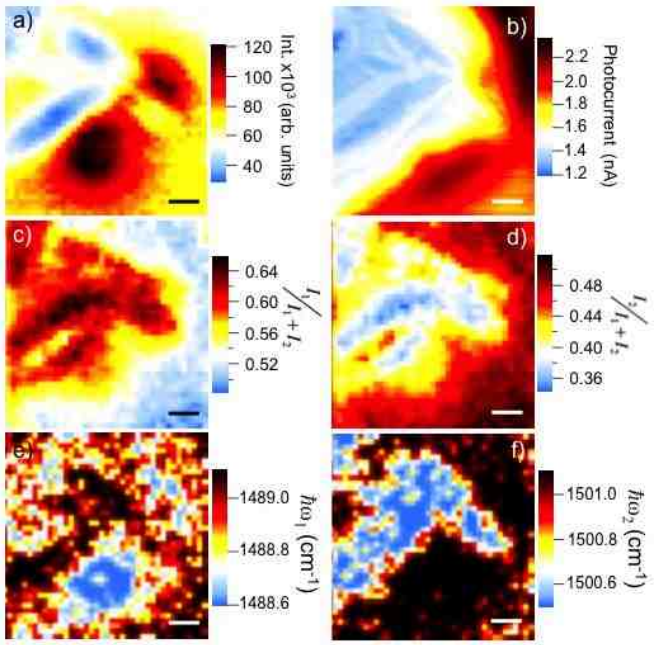

Figure 5.9 a) Total integrated Raman intensity of C=C symmetric stretching mode ($\nu_{6,7}$) and b) corresponding photocurrent images of annealed PBTTT/PCBM (1:4 w/w) device (excitation energy = 2.71 eV). (c, d) Ratios, and (e, f) frequency dispersion, of ordered (ν_6) and disordered (ν_7) PBTTT species, respectively. Scale bar = 2 μm.

Because of high PCBM loadings (1:4 w/w) it is unlikely that PBTTT completely phase separates and the entire film corresponds to ordered and disordered mixed phases. We propose that PCBM-rich regions are indeed bimolecular crystals and PBTTT chain planarity is restored from the initial kinetic disordered mixed phase. This result is consistent thiophene rings becoming more ordered probably due to small rearrangements of the pendant alkyl side groups upon annealing. REP plots (Figure 5.6) are also in agreement with this picture where the higher energy feature corresponding to disordered chains decreases significantly with annealing. Comparison of morphology-dependent frequency dispersion characteristics of ordered and disordered species (Figure 5.9e,f,

respectively) show slight red-shifts for the disordered PBTTT chains in the vicinity of PCBM crystallites, suggesting a coalescence with the ordered variant. However, photocurrent production regions of bimolecular crystals are lower than the surroundings which might originate from the large scale phase separation in our model devices. It is also noteworthy that the excitation energy used (2.71 eV) can excite PCBM although its cross-section is still substantially lower than PBTTT. For comparison, photocurrent images are generated using 488 nm (2.54 eV) light closer to the absorption maximum of PBTTT but these images show identical behavior as photocurrent images in Figure 5.9b albeit with improved output and contrast (Figure 5.10). The effects of excitation intensity and PCBM crystal size (annealing time) on local photocurrent production were also investigated and no significant differences were found (Figure 5.10).

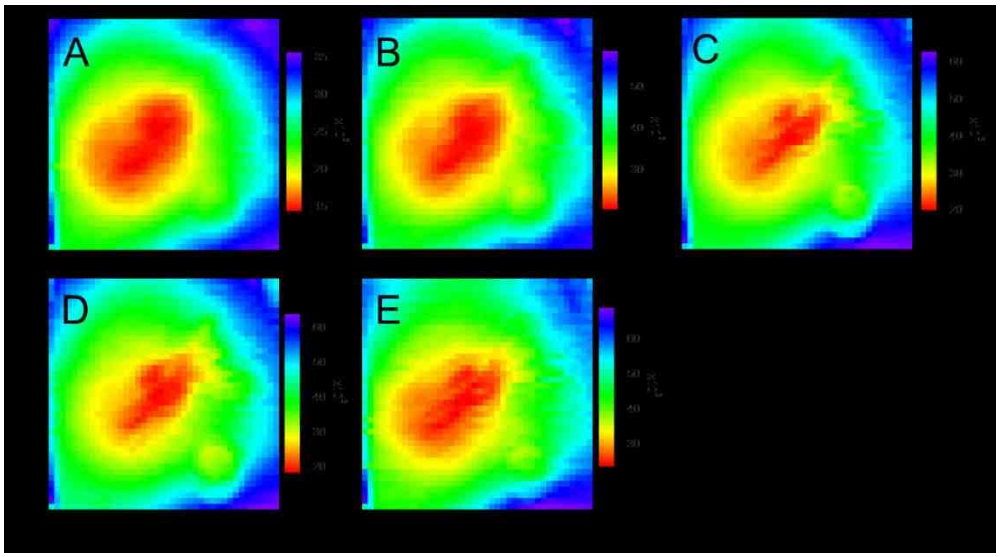

Figure 5.10 Photocurrent images of annealed PBTTT/PCBM (1:4 w/w) device (excitation energy = 2.54 eV) for same area under different excitation intensities: A) 0.5 kW/cm^2, B) 1 kW/cm2), C) 2 kW/cm^2, D) 2.5 kW/cm^2, E) 3 kW/cm^2, respectively. All image size is 10×10 μm.

Raman and photocurrent images of as-cast PBTTT/PCBM (1:4 w/w) devices were also measured under the same conditions as annealed devices (see Figure 5.11). These devices generally show nearly uniform morphological features and photocurrent is at least an order of magnitude smaller than annealed devices when illuminating with a diffraction-limited laser spot. Additionally, PBTTT exists predominantly in the disordered conformer (>60%) and, altogether, these results are consistent with a well-mixed PBTTT/PCBM phase and efficient geminate recombination.

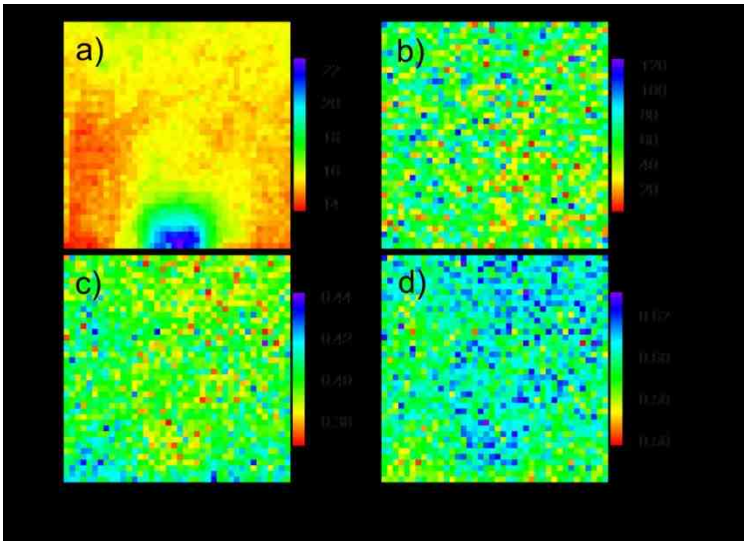

Figure 5.11 a) Total integrated Raman intensity of C=C symmetric stretching mode and b) corresponding photocurrent images of as-cast PBTTT/PCBM (1:4 w/w) device (excitation energy = 2.71 eV). (c, d) Ratios of ordered and disordered PBTTT species, respectively.

Resonance Raman and photocurrent images have so far demonstrated that morphology-dependent variations in material performance are determined not only from the amounts of PBTTT conformers but also their spatial distributions in the device active layer. Intensity modulated photocurrent spectroscopy (IMPS) and imaging is now used

to expose how specific conformers and morphologies impact loss mechanisms in PBTTT/PCBM devices, namely charge recombination.

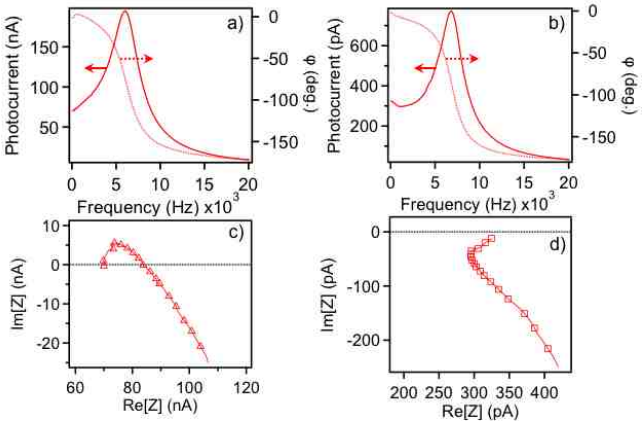

Figure 5.12 IMPS spectra (photocurrent and phase shift, φ) and Nyquist (complex) plots of annealed (a,c) and as-cast (b,d) PBTTT/PCBM (1:4 w/w) solar cells, respectively.

IMPS uses a small (~10%) sinusoidal modulation of the excitation source and the frequency is swept over several decades (typically, ~0.1 Hz up to ~1 MHz). Figure 5.12 shows IMPS ensemble spectra from annealed (Figure 6.12a,c) and as-cast (Figure 5.12b,d) PBTTT/PCBM (1:4 w/w) solar cells recorded by using a widefield configuration that illuminates the entire device active area (~20 mm^2). Ensemble IMPS sweeps show similar behavior as reported previously in related polymer/fullerene solar cells and a characteristic maximum is observed in photocurrent sweeps and the phase decreases significantly in this region towards its maximum (-180 °). Photocurrents in the low frequency regime (<1 kHz) are positive and entirely real and phase shifts are positive (<10 °) for annealed devices indicating that charge carriers lead the modulation frequency. On the other hand, as-cast films show significantly lower photocurrents and phase shifts

start at ~0 °. At larger modulation frequencies, both devices show increasingly negative phase shifts due to charge carriers lagging behind the modulation frequency.

Seminikhin and co-workers first reported positive phase shifts at low modulation frequencies or, a component in the 1st quadrant of the complex (Nyquist) IMPS plot from P3HT/PCBM devices.[156] This feature has been attributed to non-geminate charge recombination processes that become more pronounced as the device ages. Luther and co-workers recently advanced this understanding by systematically studying device aging and preparation conditions and tracking IMPS responses.[157] These authors showed that 1st quadrant photocurrent contributions in Nyquist plots, result from the formation of deep traps and introduced a drift-diffusion model to account for this behavior. The observation of positive phase shifts in the low frequency modulation regime demonstrates that non-geminate recombination processes become operative in annealed devices indicating suppression of geminate recombination. The lack of this signature in as-cast devices (either fresh or aged), suggests that faster geminate processes dominate which occur on timescales beyond what is currently accessible by IMPS techniques but, it is possible to now directly spatially correlate non-geminate recombination sites and zones to specific PBTTT conformers and larger scale morphological features using a hybrid IMPS imaging approach.

IMPS images were generated using the same high NA objective used for Raman and quasi-DC photocurrent images and are shown in Figure 5.13. Scan ranges were expanded to 20×20 μm and laser modulation frequencies were held fixed throughout the scans using similar power densities as the quasi-DC photocurrent images shown in Figure 5.9. Several modulation frequencies were selected representing different charge transport

and recombination regimes observed in ensemble IMPS spectra, namely, low frequency (e.g., 1 and 3 kHz), near the maximum frequency photocurrent (~7 kHz) and at the high frequency regime (~9 kHz). PBTTT/PCBM blends were annealed for longer times in order to achieve greater phase separation that allows us to better resolve distinct phase boundaries. Similar to quasi-DC Raman and photocurrent images shown in Figure 5.9, PCBM-rich (bimolecular crystal) regions in Figure 5.13 produce lower photocurrent output than the surrounding mixed phase. From the IMPS phase shift (φ) images, positive phase shift accumulates on the periphery of these regions. As the modulation frequency increases past the resonance maximum, IMPS images lose contrast owing to carriers lagging significantly behind the modulation and the technique no longer very sensitive to morphology. We infer regions of positive phase shift (or, relative positive phase shift at higher modulation frequencies) represent recombination zones for non-geminate processes since separated electron-hole carriers can diffuse away from the interface before becoming trapped. In this case, trap sites are likely located at phase boundaries between ordered and disordered PBTTT regions or, partially and fully intercalated regions, which is consistent with the current and phase maps (Figure 5.13). Despite loss of resolution at higher modulation frequencies, these results, in general, show that lateral diffusion effects are probably not significant since features of size scales comparable to the diffraction limit are resolvable.

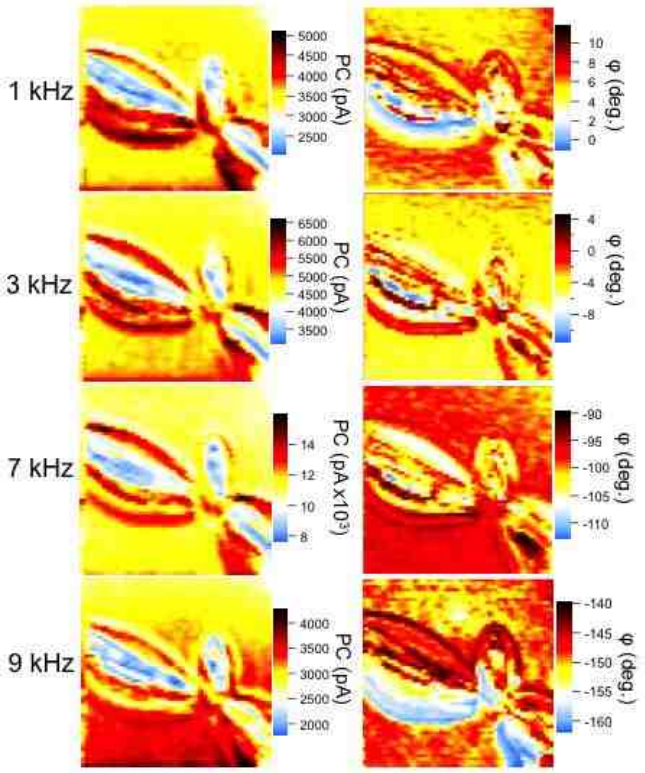

Figure 5.13 IMPS photocurrent (left) and phase shift (φ, right) im-ages of same area at 1 kHz, 3 kHz, 7 kHz, 9 kHz laser modulation frequency of annealed PBTTT/PCBM (1:4 w/w) device (excitation energy = 2.54 eV). Image scan area = 400 μm^2.

It is also interesting to note that Troisi and co-workers found that so-called 'self-healing' phenomena can de-trap charges owing to the structural similarity between ordered transport sites and disordered shallow traps.[228] However, it remains to be seen if a similar mechanism is conceivable in PBTTT/PCBM solar cells but, Raman spectra clearly demonstrate that inter-conversion between PBTTT conformers is possible although new molecular-level strategies to spatially control order/disorder boundaries are needed.

5.3 Conclusion

We have shown that resonance Raman spectroscopy of PBTTT/PCBM blends can be used in a straightforward manner to extract the relative amounts of ordered and disordered PBTTT conformers. Both ordered and disordered components exist in a mixed phase but, the former are found in bimolecular crystals whereas the latter correspond to precursors of the ordered forms. The larger frequency and linewidth of disordered chains likely originate from greater side group disorder and twisted monomer thiophene rings. DFT simulations and excitation energy dependent Raman spectra supported this assignment although we point out that previous studies have shown that PBTTT chains in the bimolecular crystals tend to twist around the intercalated fullerene. This common structural trait shared between ordered and disordered PBTTT chains localizes excitations, hence, the invariance of Raman overtone-combination intensities with PCBM loading. Resonance Raman and photocurrent images next exposed the morphology dependence of intercalation-induced order/disorder and its influence on local current generation. IMPS spectra and images showed evidence for increased non-geminate recombination at the boundaries between bimolecular crystals and disordered mixed zones. This comes at the expense of geminate processes which are much more detrimental to performance owing to the faster timescales of recombination in well-mixed blends. Overall, these experiments help bridge the gap in understanding of how ground state structure and interactions influence the outcomes of excited state photovoltaic processes.

Chapter 6

Effect of 2,3,5,6-Tetrafluoro-7,7,8,8-tetracyanoquinodimethane Charge Transfer Dopants on the Conformation and Aggregation of Poly(3-hexylthiophene)

(This chapter is based on a previously published article, *Journal of Materials Chemistry C* 2013, 1, 5638-5646.)

6.1 Introduction

Charge transfer dopants are effective for tuning electronic properties of organic semiconductors.[244,245] Doping of polymer/fullerene solar cell blends has resulted in significant improvements in power conversion efficiencies arising from better charge generation and transport.[246,247] While electrical properties have been well-studied and mechanistic aspects of charge transfer doping are emerging,[51,244,245,248] the understanding of changes in polymer structure and morphology have lagged behind. This aspect is important in crystalline polymers where charge transport efficiency depends on the ability of the polymer to form well-packed domains (i.e., aggregates). Moreover, fullerenes limit the ability of the polymer to aggregate that may have unforeseen impacts on material performance.

We study the effect of doping using the strong electron acceptor, 2,3,5,6-tetrafluoro-7,7,8,8-tetracyanoquinodimethane (F_4-TCNQ), with regio-regular poly (3-hexylthiophene) (P3HT) system with blends of [6,6]-phenyl-C_{61}-butyric acid methyl ester

(PCBM). Various spectroscopic techniques and chemical mapping via electron energy loss spectroscopy (EELS) in a scanning transmission electron microscope (STEM) are used to ascertain the effect of doping on P3HT aggregation and overall morphology.

Efficient doping occurs when the LUMO of the acceptor is deeper than the HOMO of the polymer donor and a hole is injected onto the former.[46,244,248] Doping is generally believed to be a two-step process for organic semiconductors where the donor is first ionized followed by dissociation of the charge transfer pair. Charge transfer doping is readily achieved in P3HT (HOMO ~5.0 eV) using the F_4-TCNQ acceptor with its LUMO lying at ~5.2 eV.[46,56,249-252] Formation of a charge transfer complex in P3HT/F_4-TCNQ systems was predicted by Aziz et al.[253], but the manner in which the complex dissociates into free charges is still actively debated.[51,248] Pingel and Neher most recently reported that integer charge transfer occurs upon contact of P3HT and F_4-TCNQ as opposed to the more commonly accepted partial (hybrid) charge transfer description.[51] These authors show that a large fraction of charges remain bound thus explaining the lower than expected amounts of free charge carriers.[46]

Doping P3HT with F_4-TCNQ has recently seen use in solar cell applications and large improvements in device power conversion efficiency are possible. Most notably, improvements of the power conversion efficiency >1% have been obtained for the prototypical P3HT/PCBM blend for small amounts of F_4-TCNQ (<3%).[252] This improvement has been attributed to the increase in intrinsic carriers that modifies the effective Fermi level.[252] Enhanced charge percolation by stabilization of separated charges (increased permittivity) and increasing charge generation pathways thereby suppressing charge recombination have also been proposed.[248]

In P3HT/PCBM blends, the current view is that the volume fraction of aggregated P3HT chains increases due to the presence of F_4-TCNQ.[252] Duong et al. recently performed X-ray scattering studies on P3HT/F_4-TCNQ and showed compelling evidence for two different concentration dependent mixed phases.[254] These authors also confirmed that P3HT/F_4-TCNQ interactions are decided in the solution phase prior to thin film deposition, which is especially important since polymer conformation and aggregation are affected by solvent-solute interactions. Theoretical simulations have proved useful in exposing the nature of charge transfer interactions and a partial charge transfer of ~0.5 e^- was recently predicted between an oligothiophene to F_4-TCNQ.[255] However, further work is required to determine how dopants interact with the distinct morphological forms of P3HT (i.e., amorphous and aggregated regions) which are regulated by PCBM content as well as processing conditions.

We measure resonance Raman and optical spectra of P3HT and P3HT/PCBM blend thin films doped with varying amounts of F_4-TCNQ that help expose the nature of interactions between P3HT aggregates and dopants. We find that the amounts of pristine type P3HT aggregates decrease with increased dopant loading but complexed P3HT chains are more planar relative to their pristine state. This charge transfer induced planarity enhancement is apparent at low dopant loading (<10%) and gives rise to greater J-aggregate character in optical spectra where high intrachain order reduces interchain exciton coupling.[121,127] We speculate that F_4-TCNQ dopants interact with dangling or looping chains on the periphery of nascent P3HT aggregates according to the integer charge transfer description. Subsequent charge separation (doping) is facilitated by the ordered π-stacked regions that permit intrachain charge delocalization. Hole injection

into aggregated P3HT chains increases their backbone planarity and rigidity possibly from increased quinoidal character.[256-259] DFT simulations using a similar model as reported corroborate our experimental findings and we propose that the greater rigidity of complexed P3HT chains destabilizes the pristine-type aggregate π-stacks leading to the previously proposed mixed phase possessing different packing characteristics.[254] STEM images with EELS detection show that doped P3HT chains tend to cluster together leading to increased phase segregation in the presence of PCBM.

6.2 Data results and Discussions

6.2.1 Optical Spectroscopy

This paper is primarily concerned with understanding the nature of dopant interaction with crystalline and amorphous P3HT species. The relative amounts of each are regulated by PCBM acceptors[234] and processing conditions to help determine whether F_4-TCNQ dopants exhibit preferential interactions towards either form. We focus on dopant loadings commonly encountered in solar cell device applications (i.e., <10%) which typically have limited P3HT aggregate content.

Optical spectroscopy is an excellent tool to assess not only the amount of P3HT aggregates in various environments but also the type and strength of aggregate exciton coupling.[126,260] Figure 6.1 shows absorption and PL spectra of pristine P3HT (A, B) and P3HT/PCBM blend (C, D) thin films with varying amounts of F_4-TCNQ. Previous optical spectroscopy lineshape analyses demonstrate that P3HT aggregates comprise ~50% or greater of the total P3HT chains in pristine films,[126,260] which is reduced substantially when PCBM is added. Absorption and PL 0-0/0-1 vibronic intensity ratios of the

characteristic P3HT aggregate lineshapes show gradual increases upon addition of F_4-TCNQ up to 10%. Absorption and PL electronic origin energies ($E_{0\text{-}0}$) slightly red- and blue-shift, respectively, in this doping range causing a reduction in the Stokes shift. The greater sensitivity of PL to the presence of a dopant is expected because PL occurs from minority low energy sites at the bottom of energy funnels corresponding to aggregates. These trends are highlighted in Figure 6.2 for both pristine P3HT (A) and P3HT/PCBM blends (B). As F_4-TCNQ content increases, signal-to-noise ratios decrease indicating a reduction in pristine-type P3HT. At F_4-TCNQ concentrations greater than 10%, the characteristic aggregate and amorphous absorption lineshapes diminish and transitions from the anion form of F_4-TCNQ[51,254] become dominant (see insets of Figure 6.1A,C).

We now consider P3HT/PCBM blends doped with F_4-TCNQ to understand how F_4-TCNQ affects P3HT when it is mostly in its amorphous or, unaggregated, form. Figure 6.1C,D present optical spectra of these doped blends that show similar trends as pristine P3HT films albeit larger linewidths due to greater disorder and fewer aggregates absorbing/emitting. The effect of F_4-TCNQ is more pronounced in PCBM blends suggesting that fullerenes accentuate the ground state charge transfer interaction between P3HT and F_4-TCNQ. We speculate that this effect appears from the smaller amounts of aggregates present in PCBM blends. PL spectra of doped blends show nearly quantitative quenching when F_4-TCNQ loadings are larger than 3% that are consistent with lower aggregate content. Importantly, there is no change in the vibronic interval (~1450 cm^{-1}) in either pristine and blend samples, demonstrating that changes in lineshapes are not due to self-absorption or artefacts.

A particularly noteworthy feature of optical spectra in Figure 6.1 is the increase in 0-0/0-1 vibronic intensity ratios with F_4-TCNQ content. PL spectra of pristine P3HT films show ~30% increase of the 0-0/0-1 ratios at 5% F_4-TCNQ doping but the amount of change is comparatively smaller for P3HT/PCBM blends. The increase of 0-0/0-1 vibronic ratios is consistent with increased J-aggregate character of P3HT chains meaning greater intrachain order or, planarity between monomers.[127] The fact that the aggregate portion of optical lineshapes are most affected indicates a stronger interaction with F_4-TCNQ. The observed transition to J-aggregate character requires a significant enhancement in P3HT planarity which could be realized by injection of a hole carrier resulting in greater quinoidal character. This distortion increases chain rigidity and planarity[261] which has been observed in previous redox doping and spectro-electrochemistry of polythiophene derivatives.[259,262] Although our optical spectra suggest that intrachain order increases in P3HT chains (for low doping amounts), it is not clear how the amounts of aggregated or unaggregated P3HT chains are affected.

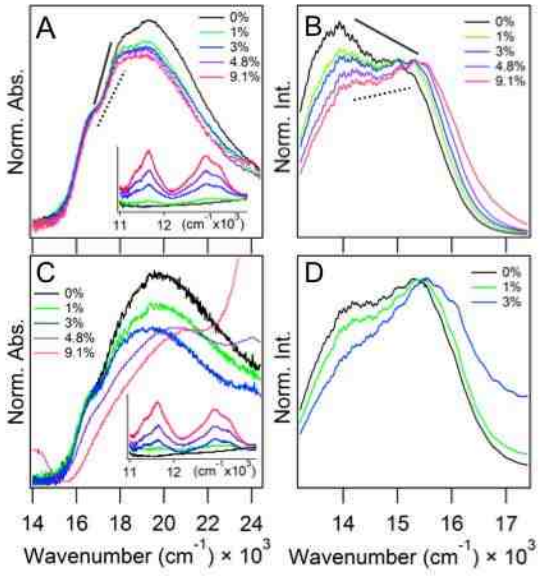

Figure 6.1 Absorption and PL spectra for A, B) P3HT films and C, D) P3HT/PCBM blend films with F_4-TCNQ doping (w/w %), respectively. Spectra were normalized at their 0-0 maxima. Sloping lines in A) and B) are included as a guide for the eye for tracking vibronic intensities with F_4-TCNQ content.

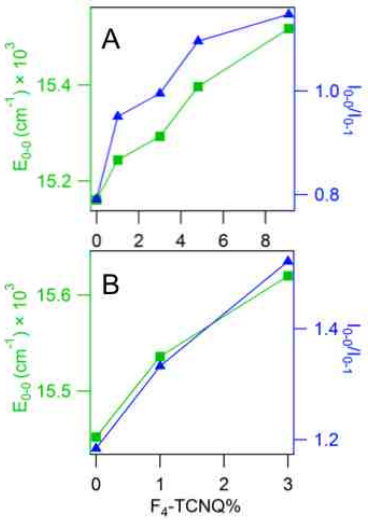

Figure 6.2 Peak positions of 0-0 emission (green) and 0-0/0-1 intensity ratios (blue) for A) P3HT films and B) P3HT/PCBM blend films with F_4-TCNQ doping.

Unfortunately, a detailed lineshape analysis of optical spectra using accepted models, such as the weakly coupled exciton theory developed by Spano and co-workers,[126,260] is complicated by the increased broadening and lower signal-to-noise ratios of the P3HT transitions with doping.

6.2.2 Raman Spectroscopy

We instead turn to resonance Raman spectroscopy which overcomes issues with overlapping lineshapes, etc, typically encountered in optical spectroscopy of conjugated polymers. This technique can be used for assessing aggregate content[152] in addition to

extracting excited state structural properties (i.e., vibrational displacements) and dynamics.[263,264] Figure 6.3 shows resonance Raman spectra of pristine P3HT and P3HT/PCBM blends with varying F_4-TCNQ content using 488 nm excitation. This wavelength probes both aggregated and unaggregated P3HT chains nearly equally and the dominant C=C symmetric stretch of P3HT (~1450-1470 cm^{-1}) can be used to determine the relative amounts of each form as well as changes in structure with doping.

It is first important to note that Raman spectra show resolved overtone transitions (0-n, n>1) of up to two harmonics in the dominant P3HT C=C mode. Overtones are nearly integer multiples of the C=C fundamental demonstrating that ground state potentials are not significantly distorted from an ideal harmonic oscillator description. We find noticeable changes in the intensities and frequencies of both fundamentals and overtones when F_4-TCNQ content is varied, similar to our previous work on poly(phenylene-vinylene)/acceptor charge transfer complexes.[263] The appearance of overtones in doped P3HT systems offers new views into the effects of ground state charge transfer interactions on excited state structural displacements. This is perhaps best understood in the time-dependent framework of resonance Raman spectroscopy where the ground state vibrational wavefunction is projected up to the excited state by absorption of a photon and evolves in time.[130,132] The time-dependent wavepacket follows the path of steepest descent (i.e., largest displaced high frequency modes) and samples the excited state potential surface followed by scattering back to a different ground state vibrational level where this information can be 'read out'. From Figure 6.3, the changes in overtone intensities and lineshapes with F_4-TCNQ doping indicate new excited state potential energy landscapes.

Normally, disorder effects and increased number of displaced modes result in the disappearance of overtones. However, the persistence of these transitions with F_4-TCNQ loading up to 10% demonstrates that the new P3HT/ F_4-TCNQ phase remain ordered as inferred from corresponding optical spectra. Although the excitation energy used to generate resonance Raman spectra in these samples primarily selects P3HT species, complications can arise from the presence of dopants. This feature makes it difficult to analyse Raman intensities with doping to extract quantitative excited state structural vibrational displacements and dyanmics. Instead, we use these spectra in a qualitative fashion to understand the effect of dopant on changes in ground and excited state structure with and without PCBM acceptors.

Increasing F_4-TCNQ content in pristine P3HT films causes gradual broadening of C=C peaks (0-1 and 0-2) particularly toward the lower energy side of the band. Overtones first show increased intensity with addition of F_4-TCNQ up to ~3% followed by a gradual decrease with increased loading (>5%). Red-shifts of these C=C transitions point to increased conjugation lengths or, enhanced planarity. Comparison between pristine and blend doped thin film Raman spectra also show larger 0-2/0-1 ratios in blends consistent with larger structural displacements. Relative overtone intensities initially increase for both sample types with F_4-TCNQ loading (up to ~3%) but then decrease with higher loadings (i.e., >3%), similar to doped P3HT Raman spectra without PCBM. Closer inspection of the fundamental (0-1) and first overtone (0-2) region in PCBM blend film Raman spectra show significant changes when F_4-TCNQ doping increases past ~5%. New transitions emerge in both regions, revealing changes in packing as well as the backbone structure. The maxima of the C=C region also show

significant blue-shifts (~7 cm^{-1}) at ~10% F_4-TCNQ loading consistent with an increase of the unaggregated P3HT form.[152]

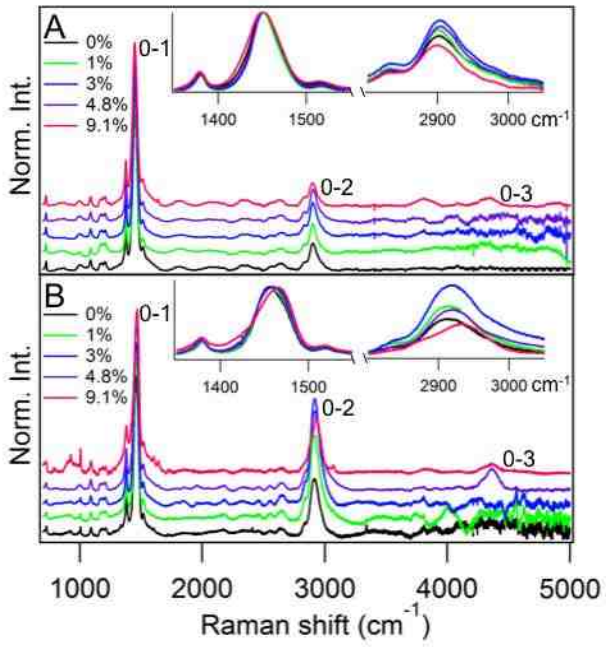

Figure 6.3 Resonance Raman spectra for A) P3HT films and B) P3HT/PCBM films with F_4-TCNQ doping. Insets: blowups of the fundamental (0-1) and first overtone (0-2) regions of C=C symmetric stretching mode.

To better understand the manner in which F_4-TCNQ dopants interact with both P3HT forms, we use a simple two species model to decompose the Raman spectra.[126,260] For example, P3HT aggregates have their C=C maximum at ~1450 cm^{-1} whereas that of the unaggregated form appear at ~1470 cm^{-1}. The C=C fundamental band is fitted with two Lorentzian lineshapes corresponding to the two components of the P3HT C=C band and we emphasize on PCBM blend spectra to since there nearly equal amounts of both P3HT forms unlike pristine samples where more chains exist in the aggregated form. Figure 6.4A shows the two component fits of the total P3HT C=C lineshape in PCBM

blends with varying F_4-TCNQ amounts up to ~10%. Vertical lines are included as a guide for the eye that represent the centre frequencies of the aggregated and unaggregated component maxima in the absence of F_4-TCNQ corresponding to 1452 cm^{-1} and 1468 cm^{-1}, respectively. As F_4-TCNQ content increases, the intensity of the aggregate component decreases indicating a loss of these species which is illustrated in Figure 6.4B with plots of the intensity ratios of aggregated/unaggregated P3HT C=C contributions. Comparison of the centre frequencies of unaggregated C=C maxima show virtually no deviation with F_4-TCNQ content but the aggregate component exhibits a gradual red-shift of up to 5 cm^{-1} and increased broadening between 0% and 10% F_4-TCNQ loadings.

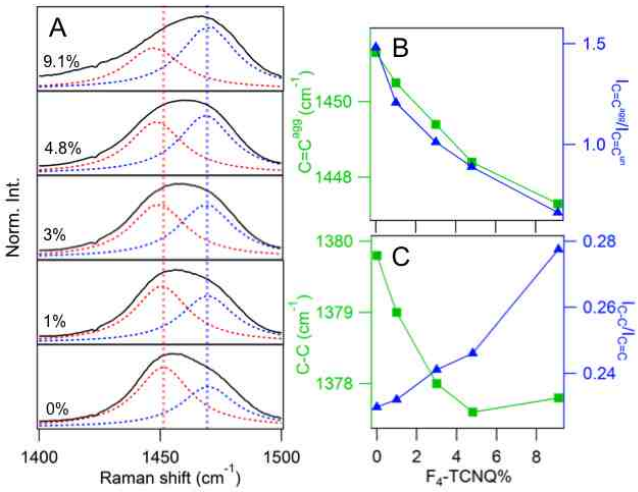

Figure 6.4 A) Fits of P3HT C=C fundamental region of P3HT/PCBM films with varying F_4-TCNQ doping. B) Aggregated C=C component centre frequency (green) and the Raman intensity ratios of aggregated to unaggregated components (blue) with F_4-TCNQ concentration. C) P3HT C-C symmetric stretching Raman center frequency and C-C/C=C intensity ratios.

The ramifications of decreased P3HT aggregate content in PCBM blends with doping are perhaps most apparent from recent studies involving pentacene doped with F_4-TCNQ.[265] Increased dopant loading resulted in reduced crystalline domain size and increase of an amorphous pentacene phase,[265] similar to that observed here. Consequently, charge mobilities decreased due to this phase transition and the loss of P3HT aggregates past typical doping thresholds (~1-3%) may explain why P3HT/PCBM solar cell performance decreases rapidly for higher dopant loadings.

It is also useful to consider other prominent P3HT backbone modes that help illuminate changes in conformation and packing with doping. For example, the P3HT C-C symmetric stretch (~1370 cm^{-1}) is sensitive to chain planarity and comparison with the dominant C=C mode reveals correlations between backbone conformation and aggregation properties.[152,266] Figure 6.4C plots the C-C frequency and C-C/C=C intensity ratios which show red-shifts and increases, respectively, with increased F_4-TCNQ loading. These trends are consistent with increased chain planarity and conjugation lengths (similar to those observed for the dominant C=C stretch).

Based on the trends outlined in Figure 6.1-6.4, the overall pristine-type aggregate population decreases with F_4-TCNQ content and a new phase corresponding to the complex is formed where P3HT chains possess increased planarity and, hence, increased J-aggregate character in optical spectra. Because the unaggregated component shows relative increases with increasing F_4-TCNQ loading up to 10% bit no significant changes in frequency suggests that the dopant interacts preferentially with aggregated P3HT chains.

A possible explanation for the apparent preference of F_4-TCNQ for P3HT aggregates may lie in differences of oxidation potentials for both forms. For example, the measured HOMO level for mostly aggregated P3HT is ~5.0 eV and the LUMO of F_4-TCNQ is ~5.2 eV. Assuming LUMO levels of aggregated and unaggregated forms are similar, the HOMO of the unaggregated form should be slightly deeper than that of the aggregated form by ~0.3 eV based on optical absorption energies.[251] This situation would make charge transfer slightly unfavourable for unaggregated P3HT whereas aggregates spontaneously undergo charge transfer with F_4-TCNQ prior to film deposition in solution. However, current experiment cannot confirm whether or not the oxidation potentials of crystalline and amorphous P3HT forms are substantially different from another.

We also explored whether the particular type of exciton coupling in the aggregate had an effect on doping efficiency. For example, variable F_4-TCNQ doping was performed on self-assembled P3HT NFs displaying either H- or J-type exciton coupling to verify if the intra- and interchain order of P3HT chains in the aggregate affect the nature of interaction with the dopant. It was found that addition of F_4-TCNQ at a level of 5% leads to almost complete quenching of H-type PL and a small, but noticeable, change to J-type behaviour whereas the J-type NFs were quenched to ~50% of their original level with no change in lineshape (Figure 6.5). Because P3HT chains in J-type NFs are already highly planarized in the aggregate π-stack, charge transfer interactions with F_4-TCNQ probably only quench PL by reducing the amount of emitters due to polaron quenching.

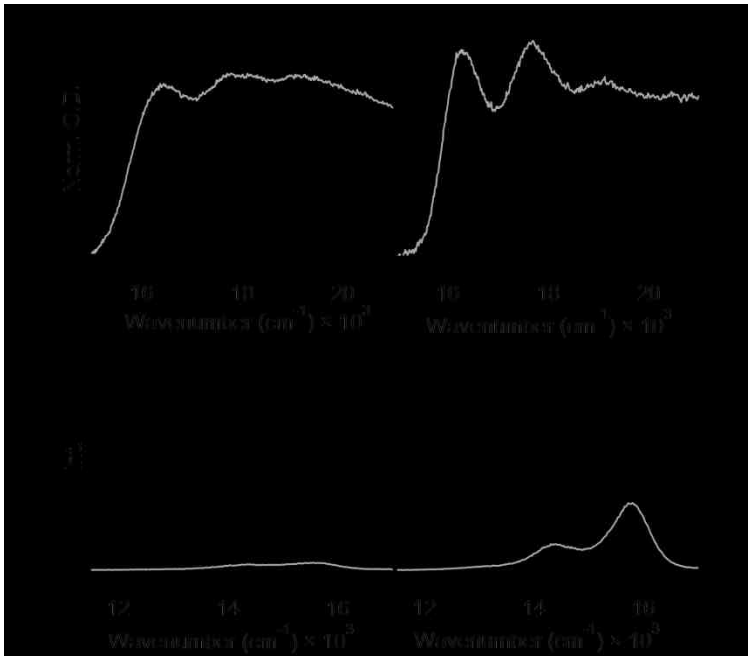

Figure 6.5 Absorption and emission spectra for P3HT NFs made from A, C) anisole and B, D) toluene solvents. Black lines are the spectra from pristine NFs. Grey lines are the spectra from NF with 5% F_4-TCNQ doping. Absorption spectra A, B) are normalized by 0-0 peaks. Emission spectra C, D) were taken from the samples with same O. D. values.

It is also worthwhile to consider that a significant fraction of P3HT exists in an 'amorphous' region on the periphery of an aggregate as dangling or looping chains.[193] We expect that F_4-TCNQ probably interacts with these P3HT segments more readily due to the close-packed nature of the aggregate crystalline region. Following integer charge transfer, the hole can delocalize along chains in the crystalline region thereby doping the polymer. At higher dopant loadings, the pristine aggregate structure becomes unstable due to increased backbone rigidity and charged nature of complexed chains and fewer interaction sites are available. These effects lead to reductions in doping efficiency and

appear exacerbated in blends where the amounts and sizes of aggregates are considerably smaller than pristine samples. We have begun preliminary studies on regio-regular and regio-random P3HT variants in solution to better understand the exact roles of aggregates in determining doping efficiency but these results will have to be published in a future report.

6.2.3 STEM/EELS Imaging

STEM imaging with EELS detection was performed on P3HT/PCBM films with varying F_4-TCNQ loadings to learn about the morphologies in doped samples when there are fewer aggregates present. Figure 6.6 shows STEM/EELS maps with the relative densities of sulphur as the contrast agent. For an aggregated P3HT domain, the sulphur density should increase, and appear as a brighter region. In the regions of mixed amorphous P3HT and PCBM, the sulphur intensity decreases due to decreased sulphur density from interspersed PCBM.[211,267] However, if the PCBM content of the mixed domain decreased, the relative intensity of sulphur would likewise increase and be visible as a brighter region in the sulphur maps. P3HT fibrils can be discerned in all four films corresponding to aggregated P3HT. In the doped samples, fibrils appear to cluster indicated by the increased sulphur intensity, which also increases with increasing F_4-TCNQ content. Comparison of carbon:sulphur ratio maps between undoped and doped samples shows that darker regions in Figure 6.6 correspond to PCBM-rich areas (Figure 6.7). The increase in apparent phase separation in doped samples can simply be attributed to the electrostatic interactions between the charged P3HT chains (and dopants) and their surroundings. The P3HT/F_4-TCNQ mixed phase (i.e., salt) is very polar making

the local environment of the complexes less energetically favourable for PCBM to reside in.

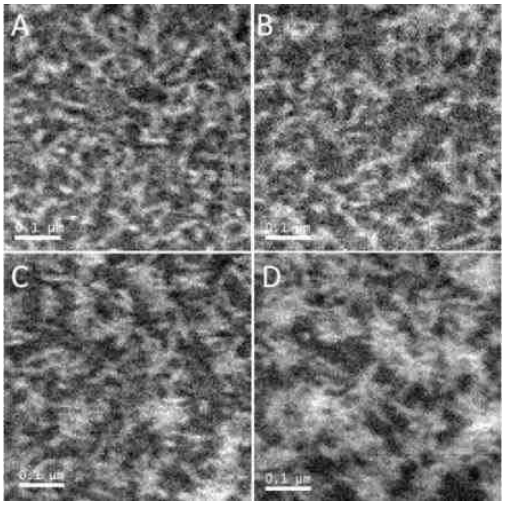

Figure 6.6 Sulfur maps of P3HT/PCBM bulk films with A) 0%, B) 0.5%, C) 2%, D) 5% F4-TCNQ doping concentrations. Scale bar = 0.1 μm.

The images in Figure 6.6 provide a more detailed view of the film morphology characteristics than scanned probe studies mainly owing to the roughness of the surface that may lead to artefacts. The tendency of complexed P3HT chains to cluster with increased dopant concentration gives the impression that aggregation is increasing. However, Raman spectra demonstrate that pristine-type P3HT aggregates decrease with dopant loading suggesting that these features in STEM/EELS images correspond to the new mixed P3HT/F_4-TCNQ phase. Unfortunately, this technique cannot distinguish changes in packing and conformational aspects of P3HT but it does demonstrate the fibril size is similar to pristine aggregates. However, these charged structures tend to cluster with increased dopant amounts making it difficult to reliably estimate their structural attributes.

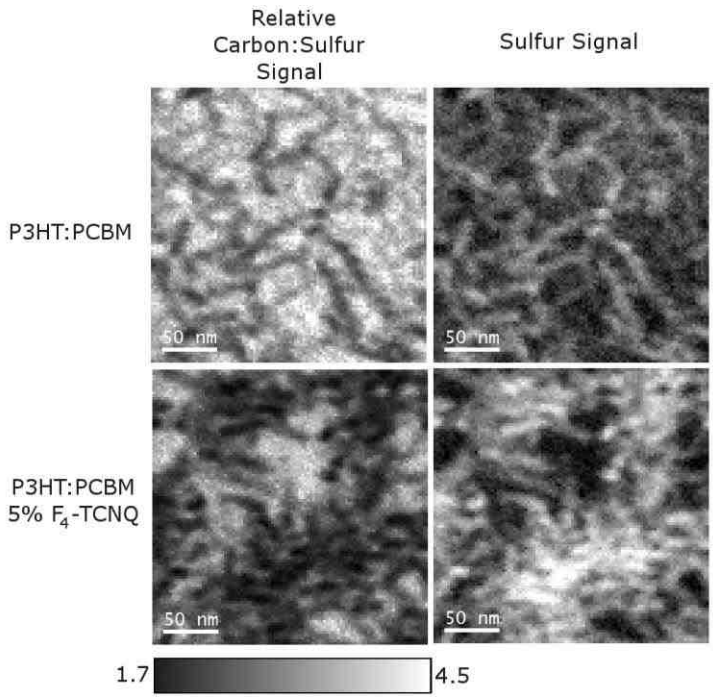

Figure 6.7 STEM/EELS images of P3HT/PCBM films without (top panels) and with 5% F_4-TCNQ doping. Left; relative carbon/sulfur signal, right; sulfur signal.

Using X-ray scattering techniques, Duong et al. demonstrated that this new mixed phase consisting of charged P3HT chains and F_4-TCNQ molecules possesses distinctly different packing characteristics than undoped P3HT aggregates.[254] We attempted to verify that the larger clumps of fibrils in doped films were in fact complexed P3HT, however, the chemical signal from the F_4-TCNQ (nitrogen or fluorine) was not strong enough to map its position. It is also important to stress that any TEM image is a projection through the volume, and three-dimensional information is lost. The reduced amounts of aggregates determined from Raman spectra of doped samples indicate that quantifying aggregation content from these two-dimensional projections results in a poor indication of total aggregation.

The growth of a new mixed phase can shed light on the anomalous trends in Raman spectra in Figure 6.3 where overtones show an initial increase in relative intensity followed by a decrease and broadening at higher dopant concentration. The fact that overtones persist in this new phase indicates that it is still well ordered, as confirmed by Duong et al., but does not remain in the typical aggregate π-stack as originally proposed. The increased broadening of these bands is also consistent with the broadening of the energetic distribution of charge transport sites with larger (>10%) F_4-TCNQ doping.[46]

6.2.4 Theoretical Simulations

Based on the spectroscopic data in Figure 6.1-6.4, P3HT aggregates appear to have a greater sensitivity to the presence of F_4-TCNQ than their unaggregated counterparts. While the dopant interacts with both the crystalline and amorphous regions of the aggregate, the former are better protected due to the close-packing of P3HT chains and we expect that F_4-TCNQ more readily complexes with dangling or looping chains (i.e., amorphous region) on the periphery. Subsequent complex dissociation is realized by hole injection and intrachain delocalization into the nearby crystalline region. Raman spectra in particular indicate increased planarity of P3HT chains, which is consistent with the above hypothesis. Theoretical simulations are now used to help confirm this proposed increase in planarity of complexed P3HT chains from experiment.

DFT calculations are performed on a model oligothiophene representing P3HT and F_4-TCNQ.[253,255] A similar model was used previously by Aziz et al. and more recently by Zhu et al. to determine the amount of charge transfer between P3HT and F_4-TCNQ. These authors vary distance and orientation between the two molecules to assess

the degree of charge transfer using calculated IR spectra as a predictive tool.[255] That work reported changes in characteristic vibrational frequencies on F_4-TCNQ (i.e., CN stretches) as a means to estimate the degree of charge transfer. Here, we wish to understand the effect of F_4-TCNQ interaction on a P3HT chain segment to determine if backbone planarity is significantly affected. Raman spectra of the resultant complexes are then simulated and compared to experiment.

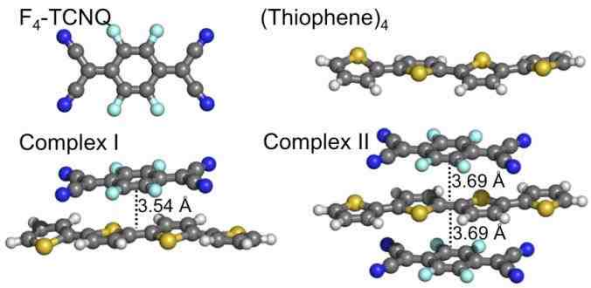

Figure 6.8 Optimized geometries of F_4-TCNQ, $(thiophene)_4$, complex I and complex II.

A thiophene oligomer with four monomer units, $(thiophene)_4$ is used to represent a P3HT segment that interacts with the dopant which is reasonable since the footprint of F_4-TCNQ spans a few thiophene monomer units. In addition, a sandwich type structure is considered where two F_4-TCNQ molecules interact with the $(thiophene)_4$ backbone. Although this structure is not expected at low to modest dopant concentrations (i.e., <10%), it may emerge at higher concentrations. Figure 6.8 shows the optimized $(thiophene)_4$ and F_4-TCNQ structures for the single complex (complex I) and the sandwich structure (complex II). Comparison of both structures reveals a larger $(thiophene)_4$ - F_4-TCNQ separation for complex II over complex I (3.69 Å vs. 3.54 Å, respectively). More importantly, we notice large changes in the planarity of the

(thiophene)$_4$ backbone depending on the nature of the complex interaction. Table 6.1 summarizes calculated dihedral angles for both complexes, which are defined in Figure 6.9.

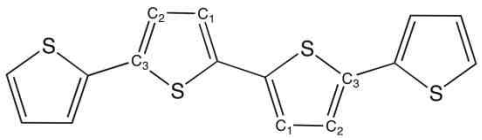

Figure 6.9 Scheme for atomic definition for the (thiophene)$_4$ oligomer.

As shown in Figure 6.8 and Table 6.1, the optimized (thiophene)$_4$ oligomer exists a non-planar geometry but planarizes upon formation of a charge transfer complex with F_4-TCNQ, as evidenced by the smaller dihedral angle, ϕ. An additional F_4-TCNQ in the sandwich structure makes the oligomer even more planar presumably due to increased intermolecular electronic delocalization between the two acceptors and the oligomer backbone.

Table 6.1 Dihedral angles of thiophene monomers from (thiophene)$_4$ for complex I and complex II.

Dihedral angle, ϕ	(Thiophene)$_4$	Complex I	Complex II
S-C-C-S	20.13	9.52	0.001
C1=C-C=C1	19.40	8.33	0.002
C2-C-C-C2	22.83	9.64	0
C3-C-C-C3	13.27	6.61	0

The amount of charge transferred in both configurations is estimated from calculated Mulliken populations with ~0.5 e^- is transferred in complex I compared to ~0.2 e^- in complex II. The smaller amount of charge transferred in the latter is reasonable since charge is delocalized over two acceptors.

These results are consistent with experimental observations demonstrating increased P3HT backbone planarity upon interacting with F_4-TCNQ. Unfortunately, it was not possible at the level of theory used to simulate longer chains and assess the extent of charge delocalization.

Figure 6.10 shows calculated frontier energy levels for complexes I and II. These energy levels are the result of intermolecular orbital mixing between the HOMO of $(thiophene)_4$ and LUMO of F_4-TCNQ. It is clear from Figure 6.10 that the HOMOs of the complexes allow a greater extent of electron delocalization, which is responsible for the planarization of $(thiophene)_4$. Comparison of HOMO-LUMO gaps for both complexes reveals a larger value for complex I (i.e., 1.11 eV vs. 0.869 eV). Calculated Raman spectra for complexes I and II show red-shifts for the dominant C=C peak (Figure 6.11) similar to experiment. However, experimental Raman spectra herein are generated on resonance with P3HT absorption transitions that likewise select specific chromphores that more closely represent pristine P3HT. We are presently pursuing studies using off-resonance Raman scattering to further understand the nature of doping interactions. Nonetheless, DFT simulations do in fact corroborate trends in Raman and optical spectra indicating greater planarity upon doping.

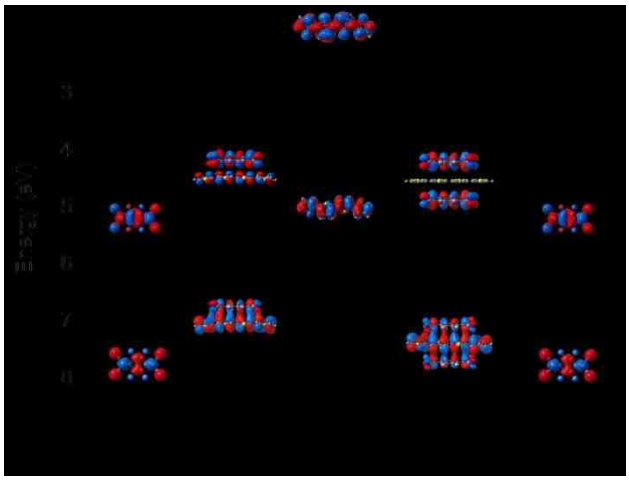

Figure 6.10 HOMO, LUMO orbital energy levels and iso-surfaces (iso-value is 0.01) for F_4-TCNQ, $(thiophene)_4$ and their charge transfer complexes, Complex I and Complex II.

The increase in P3HT chain planarity upon interacting with F_4-TCNQ may have some additional implications for charge transport and recombination. Conformational defects, such as kinks and bends, of the polymer backbone may act as shallow charge traps and lower short circuit current densities in solar cells. Enhanced polymer backbone planarity and rigidity should suppress this mechanism and therefore lead to improved device current densities.

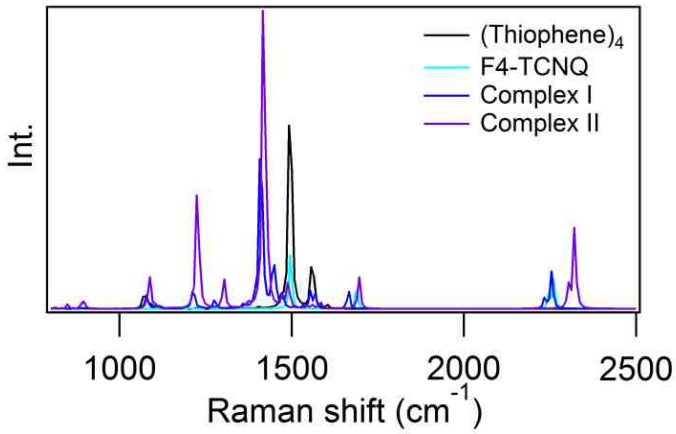

Figure 6.11 Raman spectra for $(thiophene)_4$, F_4-TCNQ, Complex I and Complex II calculated from DFT. The isolated molecules and complex I are calculated at B3LYP/6-311++G*, complex II are calculated at the B3LYP/6-31+G* level.

6.3 Conclusion

We have demonstrated that P3HT aggregates appear to play a key role in determining doping efficiency using F_4-TCNQ acceptors and are susceptible to structural

changes due to doping. A key finding from optical and Raman spectra was that doping increases the planarity of complexed P3HT chains. This was evident from increased J-aggregate character in optical spectra, increased C-C/C=C intensities in Raman spectra as well as DFT simulations. The loss of pristine-type P3HT aggregates with increased dopant concentration arises from the increased rigidity of these charged chains. STEM/EELS images showed that the new P3HT/ F_4-TCNQ phase consists of larger clusters of fibrils that probably result from the charged nature of this phase. The invariance of unaggregated P3HT segments with doping suggests that these species are not capable of delocalizing charge and thus difficult to effectively dope. Overall, ultimate doping efficiency appears to be determined by the ability of the P3HT to form aggregates, which can be seriously limited in PCBM blends. However, careful control of solution processing conditions may help mitigate these effects and increase doping efficiencies for solar cell applications.

Chapter 7

Aggregates Promote Efficient Charge Transfer Doping of Poly(3-hexylthiophene)

(This chapter is based on a previously published article, *The Journal of Physical Chemistry Letters* 2013, 4, 2953-2957.)

7.1 Introduction

Charge transfer doping of conjugated polymers by soluble small molecule acceptors has seen increased use for tuning their electronic properties (i.e., Fermi levels).[244,245,252] An essential criterion for doping is sufficient energetic offset between the polymer highest occupied molecular orbital (HOMO) and the dopant acceptor lowest unoccupied molecular orbital (LUMO) levels.[46,244,248] One of the best studied polymer/dopant systems meeting this criterion is poly(3-hexylthiophene) (P3HT) doped with 2,3,5,6-tetrafluoro-7,7,8,8-tetracyanoquinodimethane (F_4-TCNQ) where the P3HT HOMO lies at ~5 eV compared to the LUMO of F4-TCNQ at ~5.3 eV.[46,56,249-252] Surprisingly, the maximum doping efficiency of P3HT/F4-TCNQ is only about 5%, indicating that charges remain tightly bound or partial charge transfer occurs.[51] Pingel and Neher recently showed compelling evidence for the integer charge transfer model where quantitative charge transfer occurs immediately upon P3HT and F_4-TCNQ contact, but most charges remain in a tightly bound state, hence, lower than expected doping efficiencies.[46,51] The interaction between P3HT and F_4-TCNQ was also shown recently by Duong et al. to result in a new, ordered mixed phase with different packing

characteristics than pristine aggregates.[254] Despite advances toward understanding the basic mechanisms of P3HT doping with F_4-TCNQ, the role of polymer conformation and packing (aggregation) characteristics on doping efficiency remains relatively unexplored.[51,244,245,248] This is especially important for doping solution-processed polymers since solvent−solute interactions regulate the folding and packing of chains that should impact P3HT/F_4-TCNQ charge transfer interactions.[252,254]

We use a combination of electron paramagnetic resonance (EPR), NMR, optical absorption, and Raman spectroscopy on regioregular (r-Re) and regiorandom (r-Ra) P3HT variants doped with F_4-TCNQ to understand how conformation and packing of polymer chains influence charge transfer interactions and doping efficiency. The primary difference between these two P3HT forms is their ability to form π- stacked aggregate structures and adopt ordered conformations, which is only possible in r-Re samples.[128,268] It is proposed that aggregated P3HT chains act as precursors for doped species due to their relatively high intrachain order (planarity) allowing delocalization of hole carriers along the backbone.[269-273] The fact that the amounts and sizes of P3HT aggregates in solution are small could place an upper limit on the maximum attainable doping efficiency.

7.2 Results and Discussions

We begin by evaluating EPR spectra in the X-band range of r-Re and r-Ra P3HT samples in chlorobenzene solutions with varying amounts of F_4-TCNQ (Figure 7.1). Spectra are measured in the dark at 298 K and both types of P3HT had similar molecular weights (~50-60 KDa) and were prepared at the same concentration (1 mg/mL) in a dry

nitrogen environment. Both pristine P3HT and F_4-TCNQ solutions are EPR silent, although a weak signal was observed in aged F_4-TCNQ samples exposed to air for several days (Figure 7.2). A distinct resonance appears at 3346.35 G once both components are combined and EPR spectra of doped P3HT thin film samples show similar features as solution spectra in Figure 7.1 (Figure 7.3).

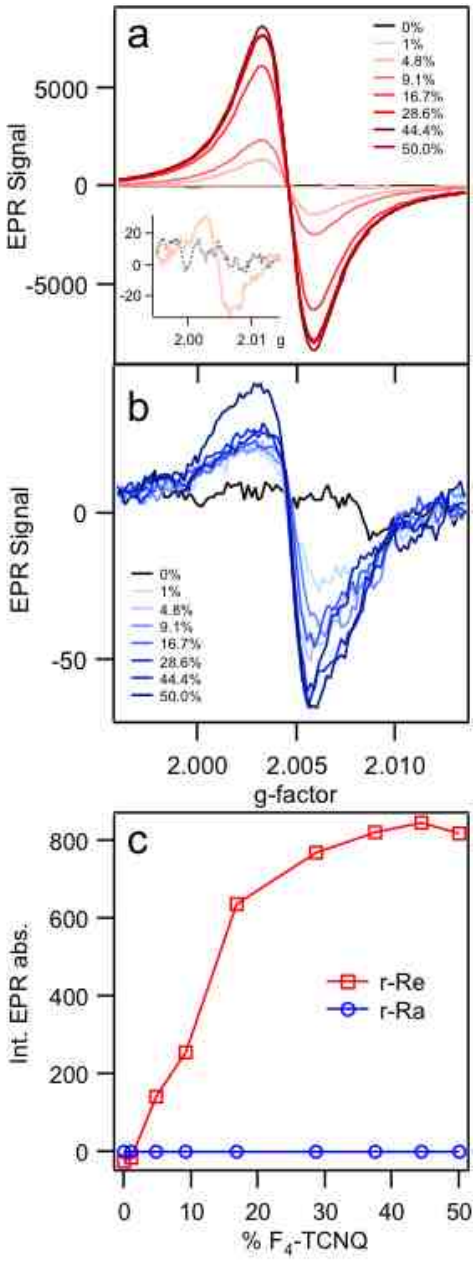

Figure 7.1 X-band EPR spectra of F_4-TCNQ doped P3HT chlorobenzene solutions. a) regio-regular (r-Re), b) regio-random (r-Ra), c) comparison of integrated EPR signals from both forms as a function of dopant concentration.

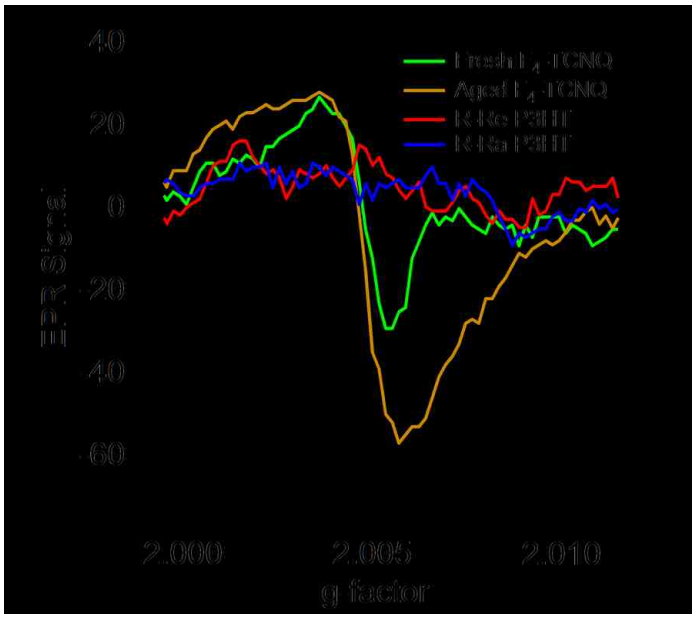

Figure 7.2 Comparison of pristine P3HT and F_4-TCNQ solutions. EPR signals from fresh and aged (over one month exposed to air) F_4-TCNQ chlorobenzene solutions.

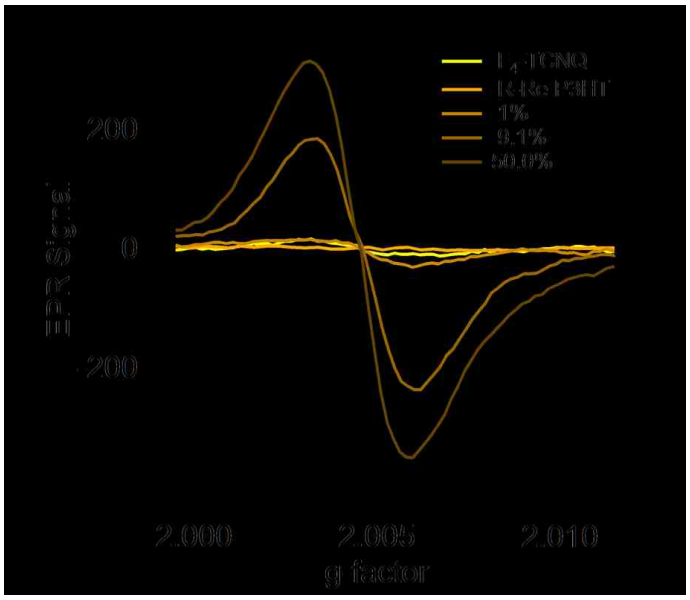

Figure 7.3 X-band EPR spectra of F_4-TCNQ doped regio-regular (r-Re) P3HT thin films.

EPR spectra of r-Re samples (Figure 7.1a) confirm the presence of paramagnetic species at dopant levels as small as ~1%. The signals show little evidence of anisotropy probably from the lack of extended order and correspond to a g-value of ~2.0046 which is slightly larger than that of a free electron (g =2.0023) but within the range commonly observed for organic radicals.[274,275] A rapid increase of the EPR signal was observed for up to ~20% F_4-TCNQ loading followed by gradual increases at larger loadings up to the maximum 50% loading used. In contrast, EPR spectra of r-Ra P3HT show much smaller signals for the same F_4-TCNQ loadings indicating very few paramagnetic species formed, albeit the g-value is similar. Integrated EPR absorption for both P3HT types are shown in Figure 7.1c that better highlight these trends.

Putatively, the rapid increase of the doped r-Re EPR signal for F_4-TCNQ loadings up to 20% corresponds to the dopant filling accessible P3HT sites. The apparent saturation of the EPR signal at F_4-TCNQ loadings higher than ~25% suggests the lack of available dopant binding sites and complete complexation of P3HT chains. Based on these EPR results, it is proposed that efficient doping is facilitated by P3HT aggregates, which only occur in r-Re P3HT.[128,276,277]

A different perspective of polymer/dopant interactions is obtained from ^{19}F NMR spectroscopy to track the signatures of fluorine atoms on F_4-TCNQ using P3HT as the dopant. Starting with neat F_4-TCNQ in deuterated chloroform solutions, a characteristic resonance at -131 ppm is observed that originates from the equivalent fluorine atoms on

F_4-TCNQ (Figure 7.4).[278] Small quantities of r-Ra or r-Re P3HT solutions (1 mg/mL) are added causing a loss of ^{19}F signal due to P3HT/F_4-TCNQ interactions. Integrated spin densities of ^{19}F NMR spectra from F_4-TCNQ solutions with varying amounts of r-Re and r-Ra P3HT are shown in Figure 7.5.

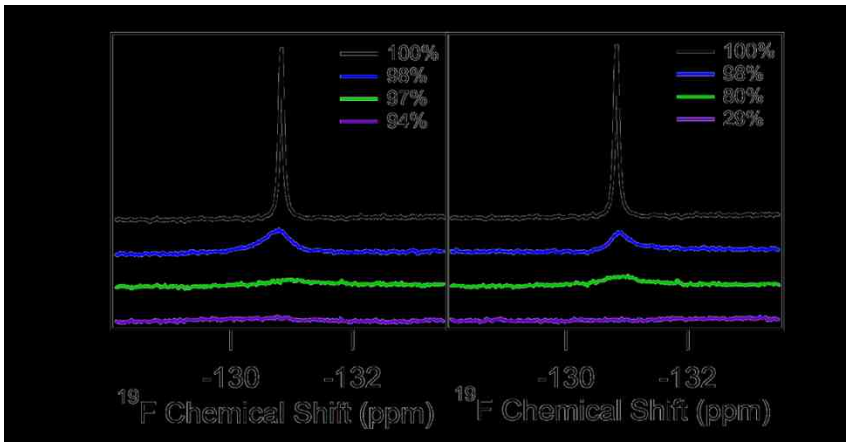

Figure 7.4 ^{19}F NMR spectra of F_4-TCNQ with varying amounts of a) r-Re and b) r-Ra P3HT in deuterated chloroform. The percentage shown in the graphs is F_4-TCNQ by weight with respect to the polymer. Note the larger concentrations of r-Ra P3HT needed to quench the signal to levels comparable to r-Re samples.

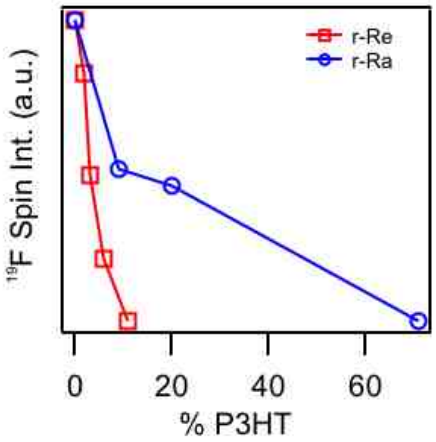

Figure 7.5 Integrated ^{19}F NMR intensities of F_4-TCNQ with varying amounts of r-Re and r-Ra P3HT in deuterated chloroform solutions.

Interestingly, both P3HT types show a similar decrease in signal at P3HT loadings ~1%. However, r-Re samples show rapid decay to background levels at ~10% P3HT loading, whereas r-Ra samples exhibit a more gradual decay to background levels only at much larger P3HT content (~70%). There are two possible origins for the disappearance of the 19F signal that may be operative: (i) reduction in the amount of neutral, diamagnetic F_4-TCNQ, and (ii) minority paramagnetic species acting as a relaxation agent.[279] At low P3HT levels (~1%), both types are expected to behave similarly due to the large excess of F_4-TCNQ, hence, the similar decrease in 19F signals. The rapid loss of ^{19}F signal in r-Re samples is expected to originate from creation of paramagnetic relaxation centers that are much more efficient in quenching the ^{19}F signal of pristine, uncomplexed F_4-TCNQ. The slower decay of the ^{19}F signal for larger r-Ra P3HT loadings suggests that signal loss arises from loss of pristine F_4-TCNQ with little to no contribution from paramagnetic species. EPR and NMR trends indicate that F_4-TCNQ interacts differently with each P3HT form, or integer charge transfer occurs for both forms but efficient doping is only realized when the polymer can adopt ordered structures.

We next turn to optical absorption spectroscopy, which should produce distinctly different lineshapes depending on whether charges remain bound or completely separate following encounter between each P3HT variant and F_4-TCNQ dopants. For example, absorption transitions from F_4-TCNQ anions appear in the NIR region in r-Re P3HT samples that have been successfully explained by the integer charge transfer model.[51] If integer charge transfer is not operative in r-Ra P3HT, a hybrid transition corresponding to

a charge transfer complex between P3HT and F_4-TCNQ should be expected.[51] Absorption spectra of r-Re and r-Ra P3HT in chlorobenzene solutions were recorded at several F_4-TCNQ amounts and displayed in Figure 7.6.

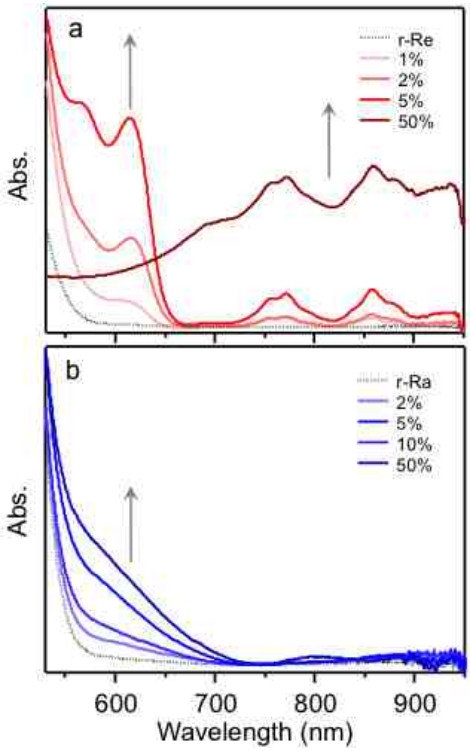

Figure 7.6 Optical absorption spectra of F_4-TCNQ doped a) r-Re and b) r-Ra P3HT thin films normalized to the P3HT maximum.

The characteristic F_4-TCNQ anion absorption transition emerges in the NIR region for r-Re samples from both solution and thin film samples (see Figure 7.6a and Figure 7.7, respectively).[51,254] Similar to trends in EPR spectra, the F_4-TCNQ anion absorption oscillator strength reaches a maximum in the range of ~30−40% dopant concentration and shows only gradual increases past this level. It is also noteworthy that P3HT centered transitions with resolved vibronic structure appear and increase with F_4-TCNQ content. Although this line shape bears similarity to P3HT aggregate absorption

transitions, we do not expect doping by F_4-TCNQ to induce aggregation similar to pristine P3HT. Instead, hole injection should increase P3HT backbone planarity most likely from increased chain rigidity and planarity.[269-272] Prior to dopants filling all available sites, the doping-induced extended chain planarity results in excitons with J-aggregate character, which is apparent from the prominent 0-0 transition at ca. 620nm (Figure 7.6a). In a related study involving doping of P3HT/PCBM blends, we demonstrated that while pristine type P3HT aggregates decrease with increasing F_4-TCNQ loading, their optical spectra show increased J-type exciton coupling indicating increased chain planarity (intrachain order).[127,143]

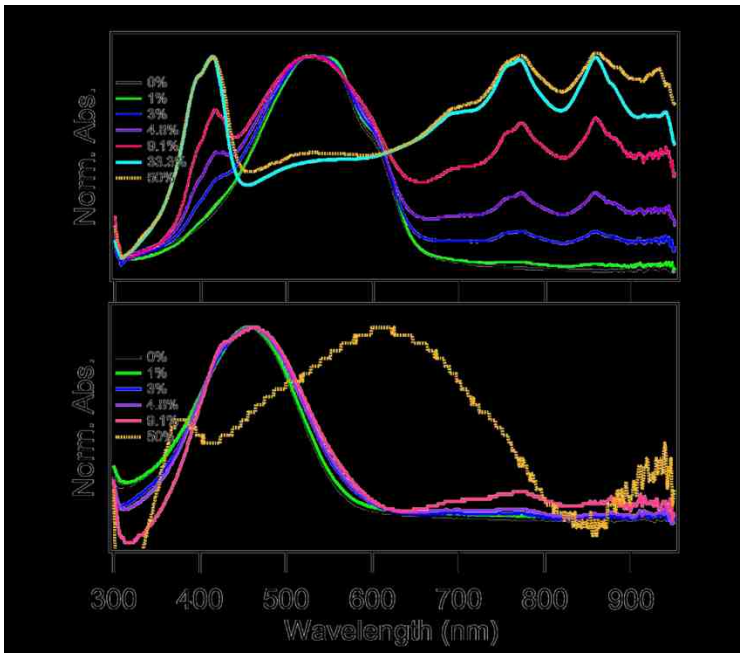

Figure 7.7 Optical absorption spectra of F_4-TCNQ doped a) r-Re and b) r-Ra P3HT thin films normalized to the P3HT maximum.

The emergence of a new, ordered mixed phase reported by Duong et al. at the expense of pristine P3HT aggregates is consistent with this assignment.[254] At larger

dopant loading, all pristine aggregates are converted to this mixed phase and doping efficiency plateaus, as observed in EPR data in Figure 7.1. Conversely, the addition of F_4-TCNQ to r-Ra P3HT samples shows very weak F_4-TCNQ anion transitions barely discernible above backgrounds and noise at the largest dopant loading. A weak and broadened transition does appear on the red onset of the pristine-type r-Ra P3HT singlet exciton transition suggesting a charge transfer complex type absorption band.[280] This feature might suggest that oxidation potentials are different for r-Re and r-Ra P3HT forms with the latter being larger. However, it is also possible that tightly bound, localized charges following integer charge transfer between r-Ra P3HT and F_4-TCNQ could give rise to similar features owing to enhanced overlap between hole and electron wave functions.

Additional insight into the nature of P3HT/F_4-TCNQ interactions and the roles of P3HT conformation and aggregation properties on doping efficiency are obtained from Raman spectroscopy. Figure 7.8 shows Raman spectra of r-Re and r-Ra P3HT solutions with varying amounts of F_4-TCNQ are measured using NIR laser excitation (λexc = 780 nm). This excitation wavelength is off resonance with P3HT optical transitions ensuring that excited state contributions from P3HT are negligible. Both r-Re and r-Ra samples (Figures 7.8a and b, respectively) show significant changes in lineshapes with dopant loading, tentatively suggesting that integer charge transfer occurs in both forms. In particular, large changes in the characteristic P3HT backbone stretching region (~1370-1515 cm^{-1}) are apparent in both samples, namely, splitting of the dominant C=C and C−C symmetric stretches (~1450 cm^{-1} and ~1370 cm^{-1}, respectively) in addition to the appearance of new transitions indicating substantial charge transfer interactions. Doping-

induced changes in Raman spectra are similar to previous reports of polythiophene doped via electrochemically or small molecules (e.g., I_2).[25,281-286]

Comparison of P3HT/F_4-TCNQ spectra with that of pristine F_4-TCNQ demonstrates that these spectral changes do not originate from the simple superposition of polymer and dopant lineshapes (Figure 7.8c).[246,287,288] Closer inspection reveals more drastic changes in doped r-Re spectra at even small dopant loading that we attribute to facile polaron generation. It is also interesting to note that the Raman excitation wavelength is resonant with the F_4-TCNQ anion absorption spectrum observed only in doped r-Re samples (Figure 7.6a). This feature suggests that resonance enhancement contributions from these species may be important and can possibly explain the greater apparent sensitivity to dopant loading observed in r-Re Raman spectra.

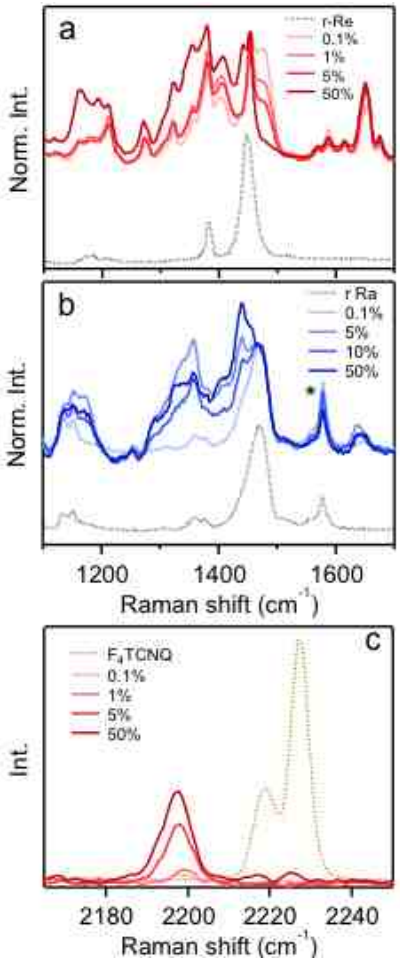

Figure 7.8 Raman spectra of F_4-TCNQ doped a) r-Re and b) r-Ra P3HT chlorobenzene solutions at selected dopant loadings (λ_{exc}=780 nm). Asterisk denotes a chlorobenzene (solvent) Raman peak. c) Raman spectra of doped r-Re P3HT in the region of the CN stretch of F_4-TCNQ.

The data in Figure 7.1-7.8 demonstrate that efficient doping occurs only in r-Re samples although both P3HT variants show evidence for charge transfer interactions with F_4-TCNQ dopants. As mentioned above, only r-Re P3HT chains are capable of assuming ordered conformations and forming well packed aggregated structures that promote hole delocalization along the backbone necessary for efficient doping. The fact that aggregated

P3HT chains are immobilized in relatively ordered (planarized) conformations minimizes torsional reorganizational barriers associated with intrachain charge delocalization.[289] Charge injection into these aggregate precursors results in doped chains that are more rigid and planar leading to increased apparent J-aggregate exciton character in optical spectra. On the other hand, disordered P3HT chains possess large torsional disorder (i.e., r-Ra P3HT) that impede intrachain hole delocalization resulting in tightly bound electrons (F_4-TCNQ) and holes (P3HT). Similar dependences of doping efficiency with P3HT conformation and packing have also been reported in previous EPR studies of heavily doped r-Re and r-Ra P3HT.[286]

The proposed delocalization of holes along aggregated P3HT chains following integer charge transfer can now explain EPR trends from Figure 7.1. For example, this process implies fast relaxation time scales of these carriers causing their signatures to be masked in room temperature EPR spectra. This is supported by previous light-induced EPR studies of hole polarons of conjugated polymer/fullerene blends reporting weak hole polaron signals above ca. 200 K[290] that were attributed to fast spin relaxation processes. Additionally, optical lineshapes of P3HT polarons are broad and featureless extending into the NIR region which is consistent with delocalization over many segments.[196,291] We therefore assign the characteristic EPR signal in Figure 7.1 as originating from F_4-TCNQ anions owing to their localized nature. This assignment was confirmed from EPR studies of F_4-TCNQ reduced by ferrocene that possess a g-value of 2.0047 (see Figure 7.9), virtually identical to that found in P3HT/F_4-TCNQ samples in Figure 7.1.

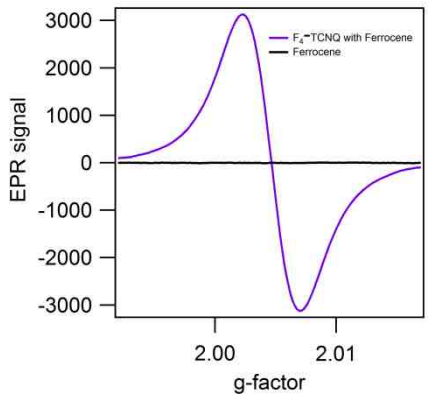

Figure 7.9 X-band EPR spectra of pristine ferrocene (black trace) and F_4-TCNQ doped ferrocene (blue trace).

7.3 Conclusion

Overall, we have shown that charge transfer doping efficiency by F_4-TCNQ in solution depends on the ability of P3HT to form aggregates. Although F_4-TCNQ interacts with both P3HT forms, intrachain hole delocalization is necessary to separate charge and therefore dope the polymer chain. This is a facile process in aggregated P3HT chains owing to their relatively high intrachain order that minimizes torsional reorganization energies. The price for such distortions is too high in r-Ra, or, unaggregated r-Re P3HT chains leading to poor doping efficiency. The dependence of doping efficiency on aggregates can limit maximum attainable doping efficiencies due to the limited amounts of these species in solutions. This limitation may potentially be overcome using solution-based self-assembly methods to fabricate semicrystalline nanofibers[127] that enable reliable control of P3HT aggregation characteristics, such as intrachain order, and possibly doping efficiency.

Chapter 8

Future work

Polymer/fullerene intercalation structures can improve exciton splitting, and also can introduce traps which will increase charge recombination rates. In addition, molecule intercalation can alter some important electronic processes, polymer backbone planarity (as discussed in Chapter 5) and other optical properties. The ability to understand this type of system will play an important role on improving device performance.

There are many questions that need to be answered regarding PBTTT polymers and the intercalation of PBTTT with other molecules. For example, how does the intercalation happen between PBTTT and small molecules, such as F_4-TCNQ? Can we identify and manipulate different electronic transitions in PBTTT and PBTTT/PCBM intercalated structures? This work will be discussed below.

8.1 Multiple Spectroscopic Study of PBTTT/F_4-TCNQ Intercalation

In addition to fullerenes, McGehee and co-workers also observed that PBTTT can form bimolecular crystals with F_4-TCNQ.[92] Ground state charge transfer complexes can be generated in this PBTTT/F_4-TCNQ blend since F_4-TCNQ electron affinity (~5.2 eV) is larger than PBTTT ionization potential (~5.1 eV).[92,220] F_4-TCNQ doping can cause increased electrical conductivity and decreased polymer π-stacking distance in PBTTT systems at relatively low concentration.[92,136] In chapter 5, we have already addressed the PCBM intercalation effects on PBTTT structures and their device performance. In this work, we will use multiple spectroscopic methods to understand the PBTTT/F_4-TCNQ

interactions and how PBTTT conformations and morphologies change upon interacting with F_4-TCNQ.

Different from P3HT absorption, PBTTT has a broad and poor resolved vibronic absorption band, which makes it impossible to identify different types of PBTTT and analyze the type and strength of PBTTT exciton couplings in variable environments. However, optical spectroscopy is still a powerful tool to study the interactions of PBTTT/F_4-TCNQ by tracking F_4-TCNQ anion signals (700-1000 nm). Figure 8.1 shows F_4-TCNQ anion peaks increase linearly with F_4-TCNQ doping concentrations (<10%) and then fluctuate at maximum intensity. Overall, F_4-TCNQ anion signals are stronger in doped PBTTT films than that of solutions at same doping levels, which indicates free charge carriers can be generated in PBTTT/F_4-TCNQ blends and doping efficiency can be affected by PBTTT conformations.

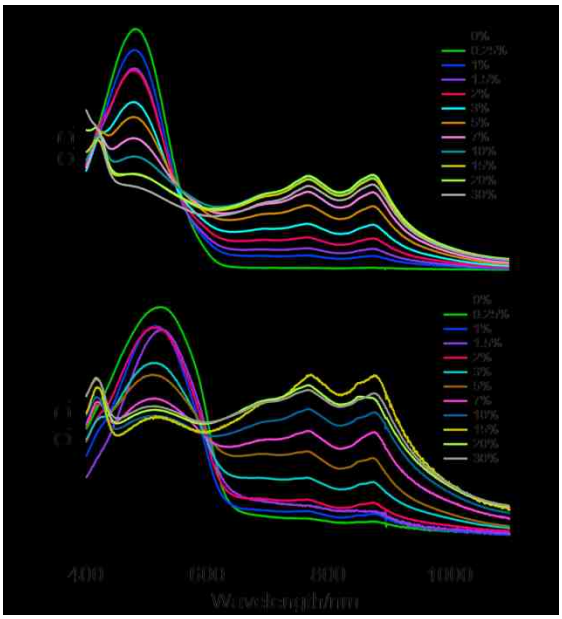

Figure 8.1 Absorption spectra of F_4-TCNQ doped A) PBTTT in o-DCB solutions and B) PBTTT films.

PCBM can accentuate the ground state charge transfer interactions of P3HT and F_4-TCNQ, as discussed in Chapter 6. Therefore, PCBM effect on PBTTT/F_4-TCNQ interactions is also investigated here. Figure 8.2 shows the absorption spectra of F_4-TCNQ doped PBTTT/PCBM solutions and films. F_4-TCNQ anion absorption intensities stay relatively similar no matter whether there is PCBM or not. Since PBTTT adopts high crystallinity form in both solutions and films, minor PBTTT structure changes by PCBM intercalation cannot significantly affect the PBTTT/F_4-TCNQ interactions.

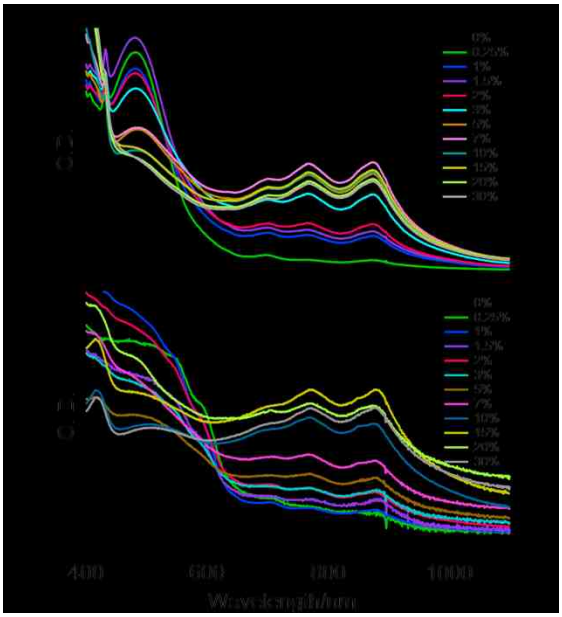

Figure 8.2 Optical absorption spectra of F_4-TCNQ doped PBTTT/PCBM A) in o-DCB solutions, and B) films.

EPR spectroscopy is used to further verify the formation of free charge carriers in F_4-TCNQ doped PBTTT/PCBM systems by detecting absorption signals from paramagnetic spins. Figure 8.3 shows both PBTTT and PBTTT/PCBM solutions have strong EPR signals at F_4-TCNQ doping levels as small as ~0.25%. G-value is ~2.0048, which is slightly larger than that of a free electron (g = 2.0023), but within the range

commonly observed for organic radicals, and stays constant for all solutions at different dopant levels. Integrated EPR absorptions for both doped PBTTT and PBTTT/PCBM solutions follow the same tendency, as shown in Figure 8. 3 C), which indicates PCBM does not have pronounced effects on the interactions of F_4-TCNQ and PBTTT even when PBTTT/F_4-TCNQ mixtures clump together and separate from the solvent at high doping concentrations.

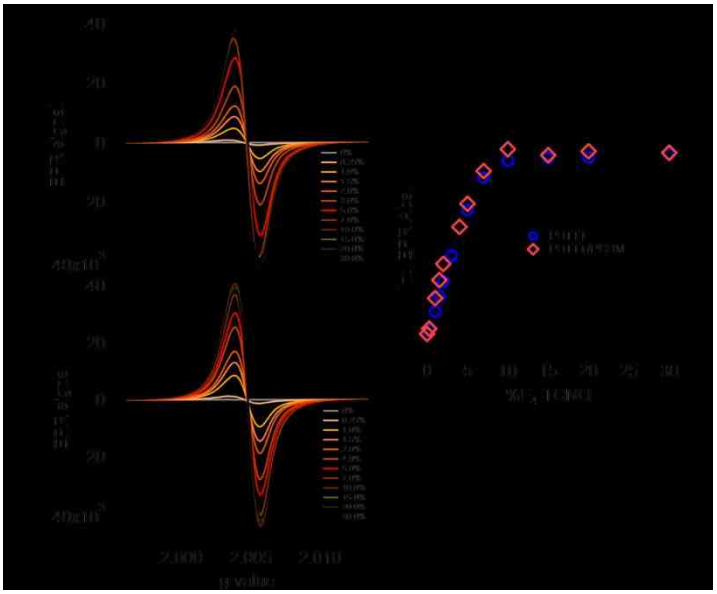

Figure 8.3 X-band EPR spectra of F_4-TCNQ doped A) PBTTT, and B) PBTTT/PCBM o-DCB solutions. C) Comparison of integrated EPR signals from both types of solutions as a function of dopant concentration.

Raman spectroscopy can offer more insights into the interaction nature of PBTTT/F_4-TCNQ and track different species, such as F_4-TCNQ anions, PBTTT polarons and neutral PBTTT in different conformations, by exciting the systems with different excitation energies. It also can address PBTTT structural changes upon interacting with F_4-TCNQ and further understand the role of PBTTT conformation and aggregation on

doping efficiency. Figure 8.4 and Figure 8.5 show the Raman spectra of PBTTT and PBTTT/PCBM solutions at variable F_4-TCNQ doping levels with 780 nm laser as the excitation source. The Raman spectra in typical PBTTT backbone stretching region (~1300-1550 cm^{-1}) for all samples show dramatic changes with F_4-TCNQ doping.

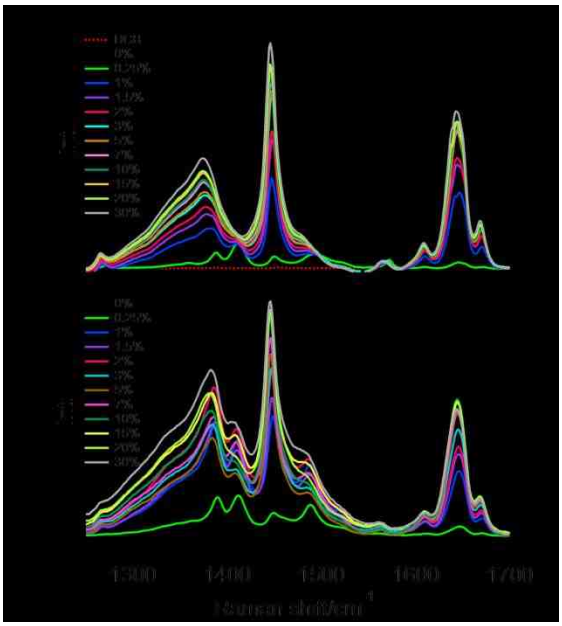

Figure 8.4 Raman spectra of F_4-TCNQ doped PBTTT A) in o-DCB solutions, and B) films (λ_{exc} =780 nm).

Neutral PBTTT and F_4-TCNQ only have minor contributions to the Raman spectra when using 780 nm as the excitation source since it is off-Resonance of PBTTT polymers and F_4-TCNQ. The significant changes in the Raman spectra should be caused by some new transitions, like PBTTT polarons, F_4-TCNQ anions and charge transfer complexes. Characteristic vibrational transitions of F_4-TCNQ anions appear in the range of 1600-1700 cm^{-1} and gain in intensity with increased F_4-TCNQ loadings.

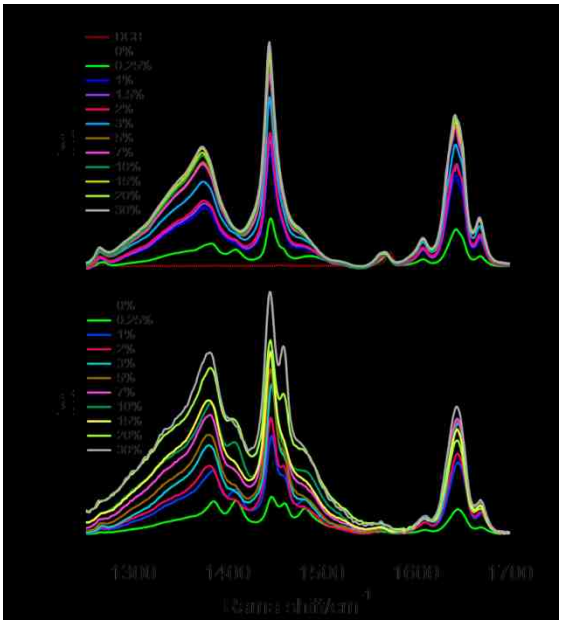

Figure 8.5 Raman spectra of F_4-TCNQ doped PBTTT/PCBM A) in o-DCB solutions, and B) films (λ_{exc} =780 nm).

Raman spectra under 780 nm can output the information of the species that absorb at NIR range, but resonance Raman measurements for PBTTT polymers are still needed in order to study PBTTT structural changes upon interacting with F_4-TCNQ. Therefore, resonance Raman experiment (458 nm to 647 nm) for doped PBTTT will be very important and can track PBTTT backbone changes relative to F_4-TCNQ loadings. Also, DFT calculations for a model of PBTTT monomer or dimers with F_4-TCNQ will produce additional information that serves to gain a better understanding of PBTTT/F_4-TCNQ interactions both structurally and electrically.

Furthermore, F_4-TCNQ might be a good additive for PBTTT/PCBM electronic devices since it can enhance the system conductivity and produce free charge carriers. This might help overcome high charge recombination[30] in PBTTT/PCBM systems and

get better performing devices. Resonance Raman and photocurrent imaging technique will spatially correlate PBTTT structures with local photocurrent efficiency while IMPS will help analyze non-geminate charge recombination and examine whether F_4-TCNQ doping can decrease this type of recombination or not.

8.2 Single Molecule Spectroscopic Study of PBTTT Nanoparticles

Multiple species have been proposed in ensemble spectra of pristine PBTTT thin films but the congested nature of the overlapping lineshapes with similar vibronic patterns casts doubts on the ability to reliably decompose spectra into their respective components.[231] As discussed in Chapter 5, it is very difficult to perform a lineshape analysis and identify different electronic origin transitions since PBTTT absorption spectrum is broad and poorly resolved. Single molecule spectroscopy on isolated PBTTT particles is used to elucidate the structure and nature of the different states that are typically obscured in ensemble spectra. Besides, detailed temperature-, pressure- and polarization-dependent PL measurements on PBTTT nanoparticles will help understand the specific structural factors that can govern exciton coupling and also their susceptibility to change with small perturbations.

Single PBTTT nanoparticle samples are made by diluting PBTTT solutions into a polystyrene matrix and measured under ambient conditions (i.e., unsealed thin films) at room temperature. PBTTT particles are well dispersed and particle sizes are diffraction limited, as shown in Figure 8.6. In addition, there is no evidence of intensity-dependent on/off flickering behavior commonly observed in single conjugated polymer chains. It is important to stress that this phenomenon is most prevalent in cases where polymer chains

fold into collapsed conformations and efficient energy transfer to minority traps leads to single chromophore-like behavior. This effect has been extensively reported in disordered polymers, such as asymmetrically substituted PPV derivatives, at the single molecule level.[292,293]

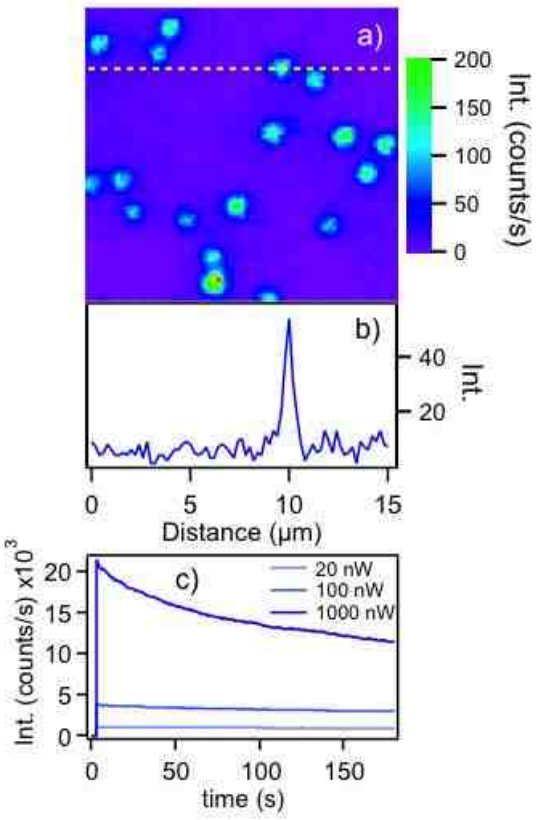

Figure 8.6 a) Single molecule fluorescence image of PBTTT nanoparticles, b) linescan for the dashed line in Figure a), c) power-dependent transients for single PBTTT nanoparticles (λ_{exc} =514 nm, excitation intensities corresponded to ~15 W/cm^2, ~80 W/cm^2, and ~800 W/cm^2).

Conversely, PBTTT is known to adopt elongated conformations thus limiting energy funneling to along the polymer backbone and transients likewise are expected to show gradual or, stepwise, time-dependent photobleaching behavior. Due to the high

crystallinity, PBTTT readily forms aggregates in solution making it difficult to obtain well-dispersed single molecules even at the low concentrations used in this study ($<10^{-9}$ M). Based on the trends found in intensity-dependent transients and known aggregation characteristics, we conclude that PBTTT probably forms nano-aggregates in these diluted solid solutions. Nonetheless, these individual particles represent parcels of larger scale aggregates in bulk films, and aggregate sizes and packing arrangements should vary from particle-to-particle allowing for a determination of the intrinsic heterogeneity present in these structures.

Single molecule spectra of PBTTT are measured to ascertain the presence of multiple emitters possibly originating from different aggregated polymorphs. Typically, brighter (larger) particles show fluorescence maxima around ~2.18 eV with weakly resolved vibronic structure and smaller particles have slightly blue-shifted fluorescence maxima (~2.25 eV) and were significantly broader on the blue edge of the lineshape, as shown in Figure 8. 7a. To determine whether multi-species are present in individual particles, time-dependent photobleaching studies for unsealed thin films are performed.

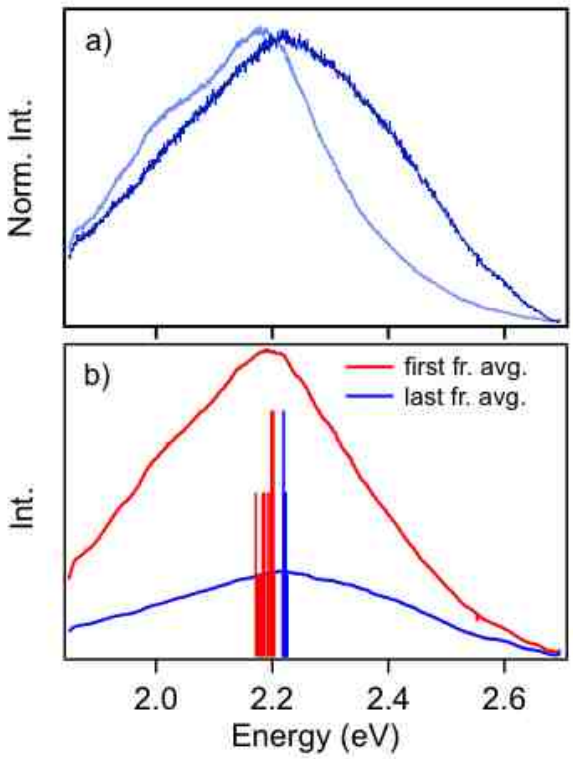

Figure 8.7 a) Fluorescence spectra for brighter (light blue) and darker (dark blue) PBTTT nanoparticles in the fluorescence images; b) time-dependent photobleaching study for PBTTT nanoparticles, red trace is the averaged first frame and blue trace is the averaged last frame of fluorescence spectra during photobleaching. (λ_{exc} =514 nm).

Since PBTTT has a relatively large oxidation potential (~5.1 eV) giving it improved photostability in ambient environments (air), it is necessary to use larger excitation intensities (>1 kW/cm^2) in order to reveal fluorescence emission energy landscapes within reasonable timescales. For each PBTTT particle, 200 spectra are acquired at 5s intervals and the first and last frames in this series are averaged for all particles studied here, as shown in Figure 8.7 b. The results indicate there are two closely-spaced emitters in PBTTT nanoparticles, consistent with previous absorption

lineshape analyses.[231] Peak energy histograms of initial (red) PBTTT emitters span ~0.05 eV then collapse to ~0.02 eV upon photobleaching (blue).

However, the peak energy maxima of each emitter are not significantly different in energy supporting the view that PBTTT aggregate polymorphs have very similar packing characteristics. The results demonstrate that emitting species correspond to at least two distinct aggregates in PBTTT nanoparticles, but the spectra do not allow us to comment on the structural attributes of each emitter (i.e., interdigitated side groups). Therefore, temperature-, pressure- and polarization-dependent experiments on PBTTT nanoparticles are proposed here as the following study to understand structural effects on different electronic transitions, which could reveal useful insights into the role of chain packings on optical properties, and further explore the susceptibility of PBTTT chain to minor perturbations in nano-aggregates.

References

(1) Coffey, D. C.; Ginger, D. S. *Nat Mater* **2006**, *5*, 735.

(2) Clarke, T. M.; Durrant, J. R. *Chemical Reviews* **2010**, *110*, 6736.

(3) Brabec, C. J. *Solar Energy Materials and Solar Cells* **2004**, *83*, 273.

(4) Thompson, B. C.; Fréchet, J. M. J. *Angewandte Chemie* **2008**, *120*, 62.

(5) Lin, C.-F.; Zhang, M.; Liu, S.-W.; Chiu, T.-L.; Lee, J.-H. *International Journal of Molecular Sciences* **2011**, *12*, 476.

(6) Chiang, C. K.; Fincher, C. R.; Park, Y. W.; Heeger, A. J.; Shirakawa, H.; Louis, E. J.; Gau, S. C.; MacDiarmid, A. G. *Physical Review Letters* **1977**, *39*, 1098.

(7) Hertel, D.; Bässler, H. *ChemPhysChem* **2008**, *9*, 666.

(8) Chamberlain, G. A. *Solar Cells* **1983**, *8*, 47.

(9) Carsten, D.; Vladimir, D. *Reports on Progress in Physics* **2010**, *73*, 096401.

(10) Tang, C. W. *Applied Physics Letters* **1986**, *48*, 183.

(11) Heiber, M. C.; Dhinojwala, A. *The Journal of Chemical Physics* **2012**, *137*.

(12) Narayan, M. R.; Singh, J. *physica status solidi (c)* **2012**, *9*, 2386.

(13) Pantoja Enriquez, J.; Mathews, N. R.; Pérez Hernández, G.; Mathew, X. *Materials Chemistry and Physics* **2013**, *142*, 432.

(14) Swanepoel, R. *Journal of Physics E: Scientific Instruments* **1983**, *16*, 1214.

(15) Yu, G.; Gao, J.; Hummelen, J. C.; Wudl, F.; Heeger, A. J. *Science* **1995**, *270*, 1789.

(16) Scharber, M. C.; Sariciftci, N. S. *Progress in Polymer Science* **2013**, *38*, 1929.

(17) Baranovskii, S. D.; Wiemer, M.; Nenashev, A. V.; Jansson, F.; Gebhard, F. *The Journal of Physical Chemistry Letters* **2012**, *3*, 1214.

(18) O'Connor, T.; Panov, M. S.; Mereshchenko, A.; Tarnovsky, A. N.; Lorek, R.; Perera, D.; Diederich, G.; Lambright, S.; Moroz, P.; Zamkov, M. *ACS Nano* **2012**, *6*, 8156.

(19) Frohne, H.; Shaheen, S. E.; Brabec, C. J.; Müller, D. C.; Sariciftci, N. S.; Meerholz, K. *ChemPhysChem* **2002**, *3*, 795.

(20) Singh, R. P.; Kushwaha, O. S. *Macromolecular Symposia* **2013**, *327*, 128.

(21) McGehee, M. D.; Topinka, M. A. *Nat Mater* **2006**, *5*, 675.

(22) Qin, H.; Li, L.; Guo, F.; Su, S.; Peng, J.; Cao, Y.; Peng, X. *Energy & Environmental Science* **2014**, *7*, 1397.

(23) Shivanna, R.; Shoaee, S.; Dimitrov, S.; Kandappa, S. K.; Rajaram, S.; Durrant, J. R.; Narayan, K. S. *Energy & Environmental Science* **2014**, *7*, 435.

(24) Wang, H.; Gomez, E. D.; Kim, J.; Guan, Z.; Jaye, C.; Fischer, D. A.; Kahn, A.; Loo, Y.-L. *Chemistry of Materials* **2011**, *23*, 2020.

(25) Zhang, Y.; Gautam, B. R.; Basel, T. P.; Mascaro, D. J.; Vardeny, Z. V. *Synthetic Metals* **2013**, *173*, 2.

(26) Brabec, C. J.; Durrant, J. R. *Mrs Bulletin* **2008**, *33*, 670.

(27) Feron, K.; Belcher, W.; Fell, C.; Dastoor, P. *International Journal of Molecular Sciences* **2012**, *13*, 17019.

(28) Bakulin, A. A.; Dimitrov, S. D.; Rao, A.; Chow, P. C. Y.; Nielsen, C. B.; Schroeder, B. C.; McCulloch, I.; Bakker, H. J.; Durrant, J. R.; Friend, R. H. *The Journal of Physical Chemistry Letters* **2012**, *4*, 209.

(29) Lou, S. J.; Szarko, J. M.; Xu, T.; Yu, L.; Marks, T. J.; Chen, L. X. *Journal of the American Chemical Society* **2011**, *133*, 20661.

(30) Scarongella, M.; Paraecattil, A. A.; Buchaca-Domingo, E.; Douglas, J. D.; Beaupre, S.; McCarthy-Ward, T.; Heeney, M.; Moser, J. E.; Leclerc, M.; Frechet, J. M. J.; Stingelin, N.; Banerji, N. *Journal of Materials Chemistry A* **2014**, *2*, 6218.

(31) Yang, X.; van Duren, J. K. J.; Janssen, R. A. J.; Michels, M. A. J.; Loos, J. *Macromolecules* **2004**, *37*, 2151.

(32) Min Nam, Y.; Huh, J.; Ho Jo, W. *Solar Energy Materials and Solar Cells* **2010**, *94*, 1118.

(33) Kumar, A.; Lakhwani, G.; Elmalem, E.; Huck, W. T. S.; Rao, A.; Greenham, N. C.; Friend, R. H. *Energy & Environmental Science* **2014**, *7*, 2227.

(34) Street, R. A.; Schoendorf, M.; Roy, A.; Lee, J. H. *Physical Review B* **2010**, *81*, 205307.

(35) Marsh, R. A.; Hodgkiss, J. M.; Albert-Seifried, S.; Friend, R. H. *Nano Letters* **2010**, *10*, 923.

(36) Lyons, B. P.; Clarke, N.; Groves, C. *Energy & Environmental Science* **2012**, *5*, 7657.

(37) Sharenko, A.; Gehrig, D.; Laquai, F.; Nguyen, T.-Q. *Chemistry of Materials* **2014**.

(38) Dou, F.; Zhang, X.-P. *Chinese Physics Letters* **2011**, *28*, 097802.

(39) Morteani, A. C.; Sreearunothai, P.; Herz, L. M.; Friend, R. H.; Silva, C. *Physical Review Letters* **2004**, *92*, 247402.

(40) Scharsich, C.; Lohwasser, R. H.; Sommer, M.; Asawapirom, U.; Scherf, U.; Thelakkat, M.; Neher, D.; Köhler, A. *Journal of Polymer Science Part B: Polymer Physics* **2012**, *50*, 442.

(41) Johnson, C. E.; Boucher, D. S. *Journal of Polymer Science Part B: Polymer Physics* **2014**, *52*, 526.

(42) Lee, C.-K.; Pao, C.-W. *The Journal of Physical Chemistry C* **2012**, *116*, 12455.

(43) Miller, N. C.; Sweetnam, S.; Hoke, E. T.; Gysel, R.; Miller, C. E.; Bartelt, J. A.; Xie, X.; Toney, M. F.; McGehee, M. D. *Nano Letters* **2012**, *12*, 1566.

(44) Liu, F.; Gu, Y.; Jung, J. W.; Jo, W. H.; Russell, T. P. *Journal of Polymer Science Part B: Polymer Physics* **2012**, *50*, 1018.

(45) Sun, J.; Yeh, M. L.; Jung, B. J.; Zhang, B.; Feser, J.; Majumdar, A.; Katz, H. E. *Macromolecules* **2010**, *43*, 2897.

(46) Pingel, P.; Schwarzl, R.; Neher, D. *Applied Physics Letters* **2012**, *100*.

(47) Chan, C. K.; Zhao, W.; Kahn, A.; Hill, I. G. *Applied Physics Letters* **2009**, *94*.

(48) Kröger, M.; Hamwi, S.; Meyer, J.; Riedl, T.; Kowalsky, W.; Kahn, A. *Organic Electronics* **2009**, *10*, 932.

(49) Ki Kang, K.; Alfonso, R.; Yumeng, S.; Hyesung, P.; Lain-Jong, L.; Young Hee, L.; Jing, K. *Nanotechnology* **2010**, *21*, 285205.

(50) Sakamoto, M.; Wasserman, B.; Dresselhaus, M. S.; Wnek, G. E.; Elman, B. S.; Sandman, D. J. *Journal of Applied Physics* **1986**, *60*, 2788.

(51) Pingel, P.; Neher, D. *Physical Review B* **2013**, *87*, 115209.

(52) Meyer, J.; Hamwi, S.; Schmale, S.; Winkler, T.; Johannes, H.-H.; Riedl, T.; Kowalsky, W. *Journal of Materials Chemistry* **2009**, *19*, 702.

(53) Lafalce, E.; Toglia, P.; Lewis, J. E.; Jiang, X. *Journal of Applied Physics* **2014**, *115*.

(54) Trukhanov, V. A.; Bruevich, V. V.; Paraschuk, D. Y. *Physical Review B* **2011**, *84*, 205318.

(55) Zhang, Y.; Zhou, H.; Seifter, J.; Ying, L.; Mikhailovsky, A.; Heeger, A. J.; Bazan, G. C.; Nguyen, T.-Q. *Advanced Materials* **2013**, *25*, 7038.

(56) Han, X.; Wu, Z.; Sun, B. *Organic Electronics* **2013**, *14*, 1116.

(57) Michinobu, T. *Chemical Society Reviews* **2011**, *40*, 2306.

(58) Perez, M. D.; Borek, C.; Forrest, S. R.; Thompson, M. E. *Journal of the American Chemical Society* **2009**, *131*, 9281.

(59) Mukhopadhyay, S.; Narayan, K. S. *Applied Physics Letters* **2012**, *100*, 163302.

(60) Thomas, A.; Elsa Tom, A.; Rao, A. D.; Varman, K. A.; Ranjith, K.; Vinayakan, R.; Ramamurthy, P. C.; Ison, V. V. *Journal of Applied Physics* **2014**, *115*.

(61) Nagata, A.; Oku, T.; Kikuchi, K.; Suzuki, A.; Yamasaki, Y.; Osawa, E. *Progress in Natural Science: Materials International* **2010**, *20*, 38.

(62) Liao, H.-C.; Ho, C.-C.; Chang, C.-Y.; Jao, M.-H.; Darling, S. B.; Su, W.-F. *Materials Today* **2013**, *16*, 326.

(63) Ma, W.; Tumbleston, J. R.; Wang, M.; Gann, E.; Huang, F.; Ade, H. *Advanced Energy Materials* **2013**, *3*, 864.

(64) Karagiannidis, P. G.; Kalfagiannis, N.; Georgiou, D.; Laskarakis, A.; Hastas, N. A.; Pitsalidis, C.; Logothetidis, S. *Journal of Materials Chemistry* **2012**, *22*, 14624.

(65) Walker, B.; Tamayo, A.; Duong, D. T.; Dang, X.-D.; Kim, C.; Granstrom, J.; Nguyen, T.-Q. *Advanced Energy Materials* **2011**, *1*, 221.

(66) Machui, F.; Abbott, S.; Waller, D.; Koppe, M.; Brabec, C. J. *Macromolecular Chemistry and Physics* **2011**, *212*, 2159.

(67) Ruoff, R. S.; Tse, D. S.; Malhotra, R.; Lorents, D. C. *The Journal of Physical Chemistry* **1993**, *97*, 3379.

(68) Troshin, P. A.; Hoppe, H.; Renz, J.; Egginger, M.; Mayorova, J. Y.; Goryachev, A. E.; Peregudov, A. S.; Lyubovskaya, R. N.; Gobsch, G.; Sariciftci, N. S.; Razumov, V. F. *Advanced Functional Materials* **2009**, *19*, 779.

(69) Park, C.-D.; Fleetham, T. A.; Li, J.; Vogt, B. D. *Organic Electronics* **2011**, *12*, 1465.

(70) Lee, K.; Kim, J. Y.; Park, S. H.; Kim, S. H.; Cho, S.; Heeger, A. J. *Advanced Materials* **2007**, *19*, 2445.

(71) Ma, W.; Yang, C.; Gong, X.; Lee, K.; Heeger, A. J. *Advanced Functional Materials* **2005**, *15*, 1617.

(72) Mihailetchi, V. D.; Xie, H.; de Boer, B.; Popescu, L. M.; Hummelen, J. C.; Blom, P. W. M.; Koster, L. J. A. *Applied Physics Letters* **2006**, *89*.

(73) Chu, C.-W.; Yang, H.; Hou, W.-J.; Huang, J.; Li, G.; Yang, Y. *Applied Physics Letters* **2008**, *92*.

(74) Shaheen, S. E.; Brabec, C. J.; Sariciftci, N. S.; Padinger, F.; Fromherz, T.; Hummelen, J. C. *Applied Physics Letters* **2001**, *78*, 841.

(75) Hoppe, H.; Niggemann, M.; Winder, C.; Kraut, J.; Hiesgen, R.; Hinsch, A.; Meissner, D.; Sariciftci, N. S. *Advanced Functional Materials* **2004**, *14*, 1005.

(76) Hoppe, H.; Sariciftci, N. S. *Journal of Materials Chemistry* **2006**, *16*, 45.

(77) Ruderer, M. A.; Guo, S.; Meier, R.; Chiang, H.-Y.; Körstgens, V.; Wiedersich, J.; Perlich, J.; Roth, S. V.; Müller-Buschbaum, P. *Advanced Functional Materials* **2011**, *21*, 3382.

(78) Huangzhong, Y. *Synthetic Metals* **2010**, *160*, 2505.

(79) McNeill, C. R.; Westenhoff, S.; Groves, C.; Friend, R. H.; Greenham, N. C. *The Journal of Physical Chemistry C* **2007**, *111*, 19153.

(80) Dyer-Smith, C.; Benson-Smith, J. J.; Bradley, D. D. C.; Murata, H.; Mitchell, W. J.; Shaheen, S. E.; Haque, S. A.; Nelson, J. *The Journal of Physical Chemistry C* **2009**, *113*, 14533.

(81) Gao, J.; Grey, J. K. *Chemical Physics Letters* **2012**, *522*, 86.

(82) Luzio, A.; Criante, L.; D'Innocenzo, V.; Caironi, M. *Sci. Rep.* **2013**, *3*.

(83) Park, J. H.; Kim, J. S.; Lee, J. H.; Lee, W. H.; Cho, K. *The Journal of Physical Chemistry C* **2009**, *113*, 17579.

(84) Busseron, E.; Ruff, Y.; Moulin, E.; Giuseppone, N. *Nanoscale* **2013**, *5*, 7098.

(85) Xu, Y.; Sheng, K.; Li, C.; Shi, G. *ACS Nano* **2010**, *4*, 4324.

(86) Wang, M.; Wudl, F. *Journal of Materials Chemistry* **2012**, *22*, 24297.

(87) Bedford, N. M.; Dickerson, M. B.; Drummy, L. F.; Koerner, H.; Singh, K. M.; Vasudev, M. C.; Durstock, M. F.; Naik, R. R.; Steckl, A. J. *Advanced Energy Materials* **2012**, *2*, 1136.

(88) Sun, S.; Salim, T.; Wong, L. H.; Foo, Y. L.; Boey, F.; Lam, Y. M. *Journal of Materials Chemistry* **2011**, *21*, 377.

(89) Seidler, N.; Lazzerini, G. M.; Li Destri, G.; Marletta, G.; Cacialli, F. *Journal of Materials Chemistry C* **2013**, *1*, 7748.

(90) Solanki, A.; Wu, B.; Salim, T.; Yeow, E. K. L.; Lam, Y. M.; Sum, T. C. *The Journal of Physical Chemistry C* **2014**, *118*, 11285.

(91) Gao, J.; Kamps, A.; Park, S.-J.; Grey, J. K. *Langmuir* **2012**, *28*, 16401.

(92) Miller, N. C.; Cho, E.; Gysel, R.; Risko, C.; Coropceanu, V.; Miller, C. E.; Sweetnam, S.; Sellinger, A.; Heeney, M.; McCulloch, I.; Brédas, J.-L.; Toney, M. F.; McGehee, M. D. *Advanced Energy Materials* **2012**, *2*, 1208.

(93) Mandoc, M. M.; Veurman, W.; Koster, L. J. A.; de Boer, B.; Blom, P. W. M. *Advanced Functional Materials* **2007**, *17*, 2167.

(94) Rance, W. L.; Ferguson, A. J.; McCarthy-Ward, T.; Heeney, M.; Ginley, D. S.; Olson, D. C.; Rumbles, G.; Kopidakis, N. *ACS Nano* **2011**, *5*, 5635.

(95) Lenes, M.; Morana, M.; Brabec, C. J.; Blom, P. W. M. *Advanced Functional Materials* **2009**, *19*, 1106.

(96) Goris, L. J.; Haenen, K.; Nesladek, M.; Poruba, A.; Vanecek, M.; Wagner, P.; Lutsen, L. J.; Manca, J.; Vanderzande, D.; De Schepper, L. 2004; Vol. 5464, p 372.

(97) Treat, N. D.; Varotto, A.; Takacs, C. J.; Batara, N.; Al-Hashimi, M.; Heeney, M. J.; Heeger, A. J.; Wudl, F.; Hawker, C. J.; Chabinyc, M. L. *Journal of the American Chemical Society* **2012**, *134*, 15869.

(98) Hoppe, H.; Sariciftci, N. S. *Journal of Materials Research* **2004**, *19*, 1924.

(99) Northrup, J. E. *Physical Review B* **2007**, *76*, 245202.

(100) Vukmirovic, N.; Wang, L.-W. *Journal Name: The Journal of Physical Chemistry B* **2008**, Medium: ED; Size: 30.

(101) Li, L.-H.; Kontsevoi, O. Y.; Freeman, A. J. *The Journal of Physical Chemistry C* **2014**, *118*, 10263.

(102) Ohkita, H.; Ito, S. In *Organic Solar Cells*; Choy, W. C. H., Ed.; Springer London: 2013, p 103.

(103) Ohkita, H.; Kosaka, J.; Guo, J.; Benten, H.; Ito, S. *PHOTOE* **2011**, *1*, 011118.

(104) Rost, J. M.; Briggs, J. S. *Journal of Physics B: Atomic, Molecular and Optical Physics* **1990**, *23*, L339.

(105) Hsu, J.-H.; Fann, W.; Meng, H.-F.; Chen, E.-S.; Chang, E.-C.; Chen, S.-A.; To, K.-W. *Chemical Physics* **2001**, *269*, 367.

(106) Shuai, Z.; Peng, Q. *Physics Reports* **2014**, *537*, 123.

(107) Salaneck, W. R.; Friend, R. H.; Brédas, J. L. *Physics Reports* **1999**, *319*, 231.

(108) Magnuson, M.; Guo, J.-H.; Butorin, S. M.; Agui, A.; Såthe, C.; Nordgren, J.; Monkman, A. P. *The Journal of Chemical Physics* **1999**, *111*, 4756.

(109) Kröner, D.; Krüger, H.; Thesen, M. W. *Macromolecular Theory and Simulations* **2011**, *20*, 790.

(110) Stuart, B. H. *Vibrational Spectroscopy* **1996**, *10*, 79.

(111) Edwards, H. G. M.; Johnson, A. F.; Lewis, I. R. *Journal of Raman Spectroscopy* **1993**, *24*, 475.

(112) Aggarwal, R. L.; Farrar, L. W.; Saikin, S. K.; Andrade, X.; Aspuru-Guzik, A.; Polla, D. L. *Solid State Communications* **2012**, *152*, 204.

(113) Li, B.; Myers, A. B. *The Journal of Physical Chemistry* **1990**, *94*, 4051.

(114) Reigue, A.; Auguié, B.; Etchegoin, P. G.; Le Ru, E. C. *Journal of Raman Spectroscopy* **2013**, *44*, 573.

(115) Lee, H. M.; Jin, S. M.; Kim, H. M.; Suh, Y. D. *Physical Chemistry Chemical Physics* **2013**, *15*, 5276.

(116) Le Ru, E. C.; Schroeter, L. C.; Etchegoin, P. G. *Analytical Chemistry* **2012**, *84*, 5074.

(117) Meyer, S. A.; Ru, E. C. L.; Etchegoin, P. G. *The Journal of Physical Chemistry A* **2010**, *114*, 5515.

(118) Walczak, P. B.; Eisfeld, A.; Briggs, J. S. *The Journal of Chemical Physics* **2008**, *128*.

(119) Aquino, G.; Palatella, L.; Grigolini, P. *Brazilian Journal of Physics* **2005**, *35*, 418.

(120) Blaisten‐Barojas, E.; Gadzuk, J. W. *The Journal of Chemical Physics* **1992**, *97*, 862.

(121) Spano, F. C. *Accounts of Chemical Research* **2009**, *43*, 429.

(122) Eisfeld, A.; Briggs, J. S. *Chemical Physics* **2006**, *324*, 376.

(123) Spano, F. C.; Silva, C. *Annual Review of Physical Chemistry* **2014**, *65*, 477.

(124) Perroni, C. A.; Marigliano Ramaglia, V.; Cataudella, V. *Physical Review B* **2011**, *84*, 014303.

(125) Yamagata, H.; Spano, F. C. *The Journal of Chemical Physics* **2012**, *136*.

(126) Clark, J.; Silva, C.; Friend, R. H.; Spano, F. C. *Physical Review Letters* **2007**, *98*, 206406.

(127) Niles, E. T.; Roehling, J. D.; Yamagata, H.; Wise, A. J.; Spano, F. C.; Moulé, A. J.; Grey, J. K. *The Journal of Physical Chemistry Letters* **2012**, *3*, 259.

(128) Jiang, X. M.; Österbacka, R.; Korovyanko, O.; An, C. P.; Horovitz, B.; Janssen, R. A. J.; Vardeny, Z. V. *Advanced Functional Materials* **2002**, *12*, 587.

(129) Myers, A. B. *Journal of Raman Spectroscopy* **1997**, *28*, 389.

(130) Heller, E. J. *Accounts of Chemical Research* **1981**, *14*, 368.

(131) Tannor, D. J.; Heller, E. J. *The Journal of Chemical Physics* **1982**, *77*, 202.

(132) Heller, E. J.; Sundberg, R.; Tannor, D. *The Journal of Physical Chemistry* **1982**, *86*, 1822.

(133) Zink, J. I.; Shin, K.-S. K. In *Advances in Photochemistry*; John Wiley & Sons, Inc.: 2007, p 119.

(134) Beaulac, R.; Lever, A. B. P.; Reber, C. *European Journal of Inorganic Chemistry* **2007**, *2007*, 48.

(135) Gao, J.; Grey, J. K. *The Journal of Chemical Physics* **2013**, *139*.

(136) Lu, G.; Blakesley, J.; Himmelberger, S.; Pingel, P.; Frisch, J.; Lieberwirth, I.; Salzmann, I.; Oehzelt, M.; Di Pietro, R.; Salleo, A.; Koch, N.; Neher, D. *Nat Commun* **2013**, *4*, 1588.

(137) Meyer, J.; Hamwi, S.; Bülow, T.; Johannes, H.-H.; Riedl, T.; Kowalsky, W. *Applied Physics Letters* **2007**, *91*.

(138) Huang, J.; Pfeiffer, M.; Werner, A.; Blochwitz, J.; Leo, K.; Liu, S. *Applied Physics Letters* **2002**, *80*, 139.

(139) Fahlman, M.; Crispin, A.; Crispin, X.; Henze, S. K. M.; Jong, M. P. d.; Osikowicz, W.; Tengstedt, C.; Salaneck, W. R. *Journal of Physics: Condensed Matter* **2007**, *19*, 183202.

(140) Ingrosso, C.; Bianco, G. V.; Corricelli, M.; Corcelli, A.; Lobasso, S.; Bruno, G.; Agostiano, A.; Striccoli, M.; Curri, M. L. *Chemical Communications* **2013**, *49*, 6941.

(141) Deschler, F.; Da Como, E.; Limmer, T.; Tautz, R.; Godde, T.; Bayer, M.; von Hauff, E.; Yilmaz, S.; Allard, S.; Scherf, U.; Feldmann, J. *Physical Review Letters* **2011**, *107*, 127402.

(142) Gao, J.; Niles, E. T.; Grey, J. K. *The Journal of Physical Chemistry Letters* **2013**, *4*, 2953.

(143) Gao, J.; Roehling, J. D.; Li, Y.; Guo, H.; Moule, A. J.; Grey, J. K. *Journal of Materials Chemistry C* **2013**, *1*, 5638.

(144) Sardar, D.; Radcliffe, S. V.; Baer, E. *Polymer Engineering & Science* **1968**, *8*, 290.

(145) Piermarini, G. J.; Block, S.; Barnett, J. D.; Forman, R. A. *Journal of Applied Physics* **1975**, *46*, 2774.

(146) Silvera, I. F.; Chijioke, A. D.; Nellis, W. J.; Soldatov, A.; Tempere, J. *physica status solidi (b)* **2007**, *244*, 460.

(147) Goncharov, A. F.; Zaug, J. M.; Crowhurst, J. C.; Gregoryanz, E. *Journal of Applied Physics* **2005**, *97*.

(148) Yamaoka, H.; Zekko, Y.; Jarrige, I.; Lin, J.-F.; Hiraoka, N.; Ishii, H.; Tsuei, K.-D.; Mizuki, J.; apos; ichiro *Journal of Applied Physics* **2012**, *112*.

(149) Martin, T. P.; Wise, A. J.; Busby, E.; Gao, J.; Roehling, J. D.; Ford, M. J.; Larsen, D. S.; Moulé, A. J.; Grey, J. K. *The Journal of Physical Chemistry B* **2012**, *117*, 4478.

(150) Vogelsang, J.; Lupton, J. M. *The Journal of Physical Chemistry Letters* **2012**, *3*, 1503.

(151) Baghgar, M.; Labastide, J. A.; Bokel, F.; Hayward, R. C.; Barnes, M. D. *The Journal of Physical Chemistry C* **2014**, *118*, 2229.

(152) Gao, Y.; Grey, J. K. *Journal of the American Chemical Society* **2009**, *131*, 9654.

(153) Gao, Y.; Martin, T. P.; Thomas, A. K.; Grey, J. K. *The Journal of Physical Chemistry Letters* **2009**, *1*, 178.

(154) Schlichthörl, G.; Park, N. G.; Frank, A. J. *The Journal of Physical Chemistry B* **1999**, *103*, 782.

(155) Daeneke, T.; Kwon, T.-H.; Holmes, A. B.; Duffy, N. W.; Bach, U.; Spiccia, L. *Nat Chem* **2011**, *3*, 211.

(156) Byers, J. C.; Ballantyne, S.; Rodionov, K.; Mann, A.; Semenikhin, O. A. *ACS Applied Materials & Interfaces* **2011**, *3*, 392.

(157) Set, Y. T.; Heinemann, M. D.; Birgersson, E.; Luther, J. *The Journal of Physical Chemistry C* **2013**, *117*, 7993.

(158) Kietzke, T.; Neher, D.; Kumke, M.; Montenegro, R.; Landfester, K.; Scherf, U. *Macromolecules* **2004**, *37*, 4882.

(159) Wang, X.; Zhang, D.; Braun, K.; Egelhaaf, H.-J.; Brabec, C. J.; Meixner, A. J. *Advanced Functional Materials* **2010**, *20*, 492.

(160) Roehling, J. D.; Arslan, I.; Moule, A. J. *Journal of Materials Chemistry* **2012**, *22*, 2498.

(161) Kamps, A. C.; Fryd, M.; Park, S.-J. *ACS Nano* **2012**, *6*, 2844.

(162) Samitsu, S.; Shimomura, T.; Heike, S.; Hashizume, T.; Ito, K. *Macromolecules* **2008**, *41*, 8000.

(163) Neese, F. *Wiley Interdisciplinary Reviews: Computational Molecular Science* **2012**, *2*, 73.

(164) Neese, F.; Wennmohs, F.; Hansen, A.; Becker, U. *Chemical Physics* **2009**, *356*, 98.

(165) Grimme, S.; Ehrlich, S.; Goerigk, L. *Journal of Computational Chemistry* **2011**, *32*, 1456.

(166) Grimme, S.; Antony, J.; Ehrlich, S.; Krieg, H. *The Journal of Chemical Physics* **2010**, *132*.

(167) Halls, J. J. M.; Walsh, C. A.; Greenham, N. C.; Marseglia, E. A.; Friend, R. H.; Moratti, S. C.; Holmes, A. B. *Nature* **1995**, *376*, 498.

(168) Halls, J. J. M.; Cornil, J.; dos Santos, D. A.; Silbey, R.; Hwang, D. H.; Holmes, A. B.; Brédas, J. L.; Friend, R. H. *Physical Review B* **1999**, *60*, 5721.

(169) Arias, A. C.; MacKenzie, J. D.; Stevenson, R.; Halls, J. J. M.; Inbasekaran, M.; Woo, E. P.; Richards, D.; Friend, R. H. *Macromolecules* **2001**, *34*, 6005.

(170) Chappell, J.; Lidzey, D. G.; Jukes, P. C.; Higgins, A. M.; Thompson, R. L.; O'Connor, S.; Grizzi, I.; Fletcher, R.; O'Brien, J.; Geoghegan, M.; Jones, R. A. L. *Nat Mater* **2003**, *2*, 616.

(171) Morteani, A. C.; Friend, R. H.; Silva, C. *The Journal of Chemical Physics* **2005**, *122*.

(172) Xia, Y.; Friend, R. H. *Advanced Materials* **2006**, *18*, 1371.

(173) Gonzalez-Rabade, A.; Morteani, A. C.; Friend, R. H. *Advanced Materials* **2009**, *21*, 3924.

(174) Kietzke, T.; Neher, D.; Landfester, K.; Montenegro, R.; Guntner, R.; Scherf, U. *Nat Mater* **2003**, *2*, 408.

(175) Ozel, I. O.; Ozel, T.; Demir, H. V.; Tuncel, D. *Opt. Express* **2010**, *18*, 670.

(176) Pecher, J.; Mecking, S. *Chemical Reviews* **2010**, *110*, 6260.

(177) Tuncel, D.; Demir, H. V. *Nanoscale* **2010**, *2*, 484.

(178) Snaith, H. J.; Arias, A. C.; Morteani, A. C.; Silva, C.; Friend, R. H. *Nano Letters* **2002**, *2*, 1353.

(179) Cadby, A.; Dean, R.; Fox, A. M.; Jones, R. A. L.; Lidzey, D. G. *Nano Letters* **2005**, *5*, 2232.

(180) Cadby, A. J.; Dean, R.; Elliott, C.; Jones, R. A. L.; Fox, A. M.; Lidzey, D. G. *Advanced Materials* **2007**, *19*, 107.

(181) Grey, J. K.; Kim, D. Y.; Norris, B. C.; Miller, W. L.; Barbara, P. F. *The Journal of Physical Chemistry B* **2006**, *110*, 25568.

(182) Palacios, R. E.; Fan, F.-R. F.; Grey, J. K.; Suk, J.; Bard, A. J.; Barbara, P. F. *Nat Mater* **2007**, *6*, 680.

(183) Szymanski, C.; Wu, C.; Hooper, J.; Salazar, M. A.; Perdomo, A.; Dukes, A.; McNeill, J. *The Journal of Physical Chemistry B* **2005**, *109*, 8543.

(184) Tenery, D.; Gesquiere, A. J. *Chemical Physics* **2009**, *365*, 138.

(185) Tian, Z.; Yu, J.; Wu, C.; Szymanski, C.; McNeill, J. *Nanoscale* **2010**, *2*, 1999.

(186) Cadby, A.; Khalil, G.; Fox, A. M.; Lidzey, D. G. *Journal of Applied Physics* **2008**, *103*.

(187) Shikler, R.; Chiesa, M.; Friend, R. H. *Macromolecules* **2006**, *39*, 5393.

(188) Schmidtke, J. P.; Kim, J.-S.; Gierschner, J.; Silva, C.; Friend, R. H. *Physical Review Letters* **2007**, *99*, 167401.

(189) Albert-Seifried, S.; Hodgkiss, J. M.; Laquai, F.; Bronstein, H. A.; Williams, C. K.; Friend, R. H. *Physical Review Letters* **2010**, *105*, 195501.

(190) Kim, Y.; Cook, S.; Tuladhar, S. M.; Choulis, S. A.; Nelson, J.; Durrant, J. R.; Bradley, D. D. C.; Giles, M.; McCulloch, I.; Ha, C.-S.; Ree, M. *Nat Mater* **2006**, *5*, 197.

(191) Xin, H.; Ren, G.; Kim, F. S.; Jenekhe, S. A. *Chemistry of Materials* **2008**, *20*, 6199.

(192) Koppe, M.; Brabec, C. J.; Heiml, S.; Schausberger, A.; Duffy, W.; Heeney, M.; McCulloch, I. *Macromolecules* **2009**, *42*, 4661.

(193) Brinkmann, M. *Journal of Polymer Science Part B: Polymer Physics* **2011**, *49*, 1218.

(194) Sirringhaus, H.; Brown, P. J.; Friend, R. H.; Nielsen, M. M.; Bechgaard, K.; Langeveld-Voss, B. M. W.; Spiering, A. J. H.; Janssen, R. A. J.; Meijer, E. W.; Herwig, P.; de Leeuw, D. M. *Nature* **1999**, *401*, 685.

(195) Yang, H.; Shin, T. J.; Yang, L.; Cho, K.; Ryu, C. Y.; Bao, Z. *Advanced Functional Materials* **2005**, *15*, 671.

(196) Brown, P. J.; Sirringhaus, H.; Harrison, M.; Shkunov, M.; Friend, R. H. *Physical Review B* **2001**, *63*, 125204.

(197) Singh, K. A.; Sauvé, G.; Zhang, R.; Kowalewski, T.; McCullough, R. D.; Porter, L. M. *Applied Physics Letters* **2008**, *92*.

(198) Salim, T.; Sun, S.; Wong, L. H.; Xi, L.; Foo, Y. L.; Lam, Y. M. *The Journal of Physical Chemistry C* **2010**, *114*, 9459.

(199) Lee, S. W.; Lee, H. J.; Choi, J. H.; Koh, W. G.; Myoung, J. M.; Hur, J. H.; Park, J. J.; Cho, J. H.; Jeong, U. *Nano Letters* **2009**, *10*, 347.

(200) Chen, J.-Y.; Kuo, C.-C.; Lai, C.-S.; Chen, W.-C.; Chen, H.-L. *Macromolecules* **2011**, *44*, 2883.

(201) Berson, S.; De Bettignies, R.; Bailly, S.; Guillerez, S. *Advanced Functional Materials* **2007**, *17*, 1377.

(202) Spano, F. C.; Clark, J.; Silva, C.; Friend, R. H. *The Journal of Chemical Physics* **2009**, *130*.

(203) Spano, F. C.; Yamagata, H. *The Journal of Physical Chemistry B* **2010**, *115*, 5133.

(204) Yamagata, H.; Spano, F. C. *The Journal of Chemical Physics* **2011**, *135*.

(205) Kanai, Y.; Grossman, J. C. *Nano Letters* **2007**, *7*, 1967.

(206) Lan, Y.-K.; Huang, C.-I. *The Journal of Physical Chemistry B* **2009**, *113*, 14555.

(207) Sandstedt, C. A.; Rieke, R. D.; Eckhardt, C. J. *Chemistry of Materials* **1995**, *7*, 1057.

(208) Baghgar, M.; Labastide, J.; Bokel, F.; Dujovne, I.; McKenna, A.; Barnes, A. M.; Pentzer, E.; Emrick, T.; Hayward, R.; Barnes, M. D. *The Journal of Physical Chemistry Letters* **2012**, *3*, 1674.

(209) Ostrowski, D. P.; Lytwak, L. A.; Mejia, M. L.; Stevenson, K. J.; Holliday, B. J.; Vanden Bout, D. A. *ACS Nano* **2012**, *6*, 5507.

(210) Shin, K. S. K.; Clark, R. J. H.; Zink, J. I. *Journal of the American Chemical Society* **1990**, *112*, 3754.

(211) Collins, B. A.; Gann, E.; Guignard, L.; He, X.; McNeill, C. R.; Ade, H. *The Journal of Physical Chemistry Letters* **2010**, *1*, 3160.

(212) Miller, N. C.; Gysel, R.; Miller, C. E.; Verploegen, E.; Beiley, Z.; Heeney, M.; McCulloch, I.; Bao, Z.; Toney, M. F.; McGehee, M. D. *Journal of Polymer Science Part B: Polymer Physics* **2011**, *49*, 499.

(213) Miller, N. C.; Cho, E.; Junk, M. J. N.; Gysel, R.; Risko, C.; Kim, D.; Sweetnam, S.; Miller, C. E.; Richter, L. J.; Kline, R. J.; Heeney, M.; McCulloch, I.; Amassian, A.; Acevedo-Feliz, D.; Knox, C.; Hansen, M. R.; Dudenko, D.; Chmelka, B. F.; Toney, M. F.; Brédas, J.-L.; McGehee, M. D. *Advanced Materials* **2012**, *24*, 6071.

(214) Chabinyc, M. L.; Toney, M. F.; Kline, R. J.; McCulloch, I.; Heeney, M. *Journal of the American Chemical Society* **2007**, *129*, 3226.

(215) Cho, E.; Risko, C.; Kim, D.; Gysel, R.; Cates Miller, N.; Breiby, D. W.; McGehee, M. D.; Toney, M. F.; Kline, R. J.; Bredas, J.-L. *Journal of the American Chemical Society* **2012**, *134*, 6177.

(216) He, X.; Collins, B. A.; Watts, B.; Ade, H.; McNeill, C. R. *Small* **2012**, *8*, 1920.

(217) Mayer, A. C.; Toney, M. F.; Scully, S. R.; Rivnay, J.; Brabec, C. J.; Scharber, M.; Koppe, M.; Heeney, M.; McCulloch, I.; McGehee, M. D. *Advanced Functional Materials* **2009**, *19*, 1173.

(218) Cates, N. C.; Gysel, R.; Beiley, Z.; Miller, C. E.; Toney, M. F.; Heeney, M.; McCulloch, I.; McGehee, M. D. *Nano Letters* **2009**, *9*, 4153.

(219) Parmer, J. E.; Mayer, A. C.; Hardin, B. E.; Scully, S. R.; McGehee, M. D.; Heeney, M.; McCulloch, I. *Applied Physics Letters* **2008**, *92*.

(220) Sun, Q.; Park, K.; Dai, L. *The Journal of Physical Chemistry C* **2009**, *113*, 7892.

(221) He, F.; Yu, L. *The Journal of Physical Chemistry Letters* **2011**, *2*, 3102.

(222) Li, G.; Zhu, R.; Yang, Y. *Nat Photon* **2012**, *6*, 153.

(223) Heeger, A. J. *Advanced Materials* **2014**, *26*, 10.

(224) DeLongchamp, D. M.; Kline, R. J.; Jung, Y.; Germack, D. S.; Lin, E. K.; Moad, A. J.; Richter, L. J.; Toney, M. F.; Heeney, M.; McCulloch, I. *ACS Nano* **2009**, *3*, 780.

(225) Li, J.; Sun, Z.; Yan, F. *Advanced Materials* **2012**, *24*, 88.

(226) Poelking, C.; Andrienko, D. *Macromolecules* **2013**, *46*, 8941.

(227) Poelking, C.; Cho, E.; Malafeev, A.; Ivanov, V.; Kremer, K.; Risko, C.; Brédas, J.-L.; Andrienko, D. *The Journal of Physical Chemistry C* **2013**, *117*, 1633.

(228) Liu, T.; Troisi, A. *Advanced Functional Materials* **2014**, *24*, 925.

(229) Hwang, I.-W.; Young Kim, J.; Cho, S.; Yuen, J.; Coates, N.; Lee, K.; Heeney, M.; McCulloch, I.; Moses, D.; Heeger, A. J. *The Journal of Physical Chemistry C* **2008**, *112*, 7853.

(230) Banerji, N. *Journal of Materials Chemistry C* **2013**, *1*, 3052.

(231) Wang, S.; Tang, J.-C.; Zhao, L.-H.; Png, R.-Q.; Wong, L.-Y.; Chia, P.-J.; Chan, H. S. O.; Ho, P. K. H.; Chua, L.-L. *Applied Physics Letters* **2008**, *93*, 162103.

(232) Rivnay, J.; Noriega, R.; Northrup, J. E.; Kline, R. J.; Toney, M. F.; Salleo, A. *Physical Review B* **2011**, *83*, 121306.

(233) Woo, C. H.; Thompson, B. C.; Kim, B. J.; Toney, M. F.; Fréchet, J. M. J. *Journal of the American Chemical Society* **2008**, *130*, 16324.

(234) Gao, Y.; Martin, T. P.; Niles, E. T.; Wise, A. J.; Thomas, A. K.; Grey, J. K. *The Journal of Physical Chemistry C* **2010**, *114*, 15121.

(235) Lee, M. J.; Gupta, D.; Zhao, N.; Heeney, M.; McCulloch, I.; Sirringhaus, H. *Advanced Functional Materials* **2011**, *21*, 932.

(236) Cho, E. *Georgia Institute of Technology*.

(237) Giménez-Pinas, S.; Rao, A.; Kumar, A.; Smith, S. L.; Chin, A. W.; Clark, J.; van der Poll, T. S.; Bazan, G. C.; Friend, R. H. *Science* **2014**, *343*, 512.

(238) Kaake, L. G.; Moses, D.; Heeger, A. J. *The Journal of Physical Chemistry Letters* **2013**, *4*, 2264.

(239) Reber, C.; Zink, J. I. *The Journal of Physical Chemistry* **1992**, *96*, 571.

(240) Milani, A.; Brambilla, L.; Del Zoppo, M.; Zerbi, G. *The Journal of Physical Chemistry B* **2007**, *111*, 1271.

(241) Vázquez, H.; Troisi, A. *Physical Review B* **2013**, *88*, 205304.

(242) Savenije, T. J.; Grzegorczyk, W. J.; Heeney, M.; Tierney, S.; McCulloch, I.; Siebbeles, L. D. A. *The Journal of Physical Chemistry C* **2010**, *114*, 15116.

(243) Dante, M.; Peet, J.; Nguyen, T.-Q. *The Journal of Physical Chemistry C* **2008**, *112*, 7241.

(244) Walzer, K.; Maennig, B.; Pfeiffer, M.; Leo, K. *Chemical Reviews* **2007**, *107*, 1233.

(245) Lüssem, B.; Riede, M.; Leo, K. *physica status solidi (a)* **2013**, *210*, 9.

(246) Yim, K.-H.; Whiting, G. L.; Murphy, C. E.; Halls, J. J. M.; Burroughes, J. H.; Friend, R. H.; Kim, J.-S. *Advanced Materials* **2008**, *20*, 3319.

(247) Zhang, Y.; de Boer, B.; Blom, P. W. M. *Advanced Functional Materials* **2009**, *19*, 1901.

(248) Mityashin, A.; Olivier, Y.; Van Regemorter, T.; Rolin, C.; Verlaak, S.; Martinelli, N. G.; Beljonne, D.; Cornil, J.; Genoe, J.; Heremans, P. *Advanced Materials* **2012**, *24*, 1535.

(249) Zhang, Y.; Blom, P. W. M. *Applied Physics Letters* **2010**, *97*.

(250) Fujita, H.; Yuan, Y.; Michinobu, T. *Journal of Photopolymer Science and Technology* **2011**, *24*, 311.

(251) Hu, J.; Clark, K. W.; Hayakawa, R.; Li, A.-P.; Wakayama, Y. *Langmuir* **2013**, *29*, 7266.

(252) Loiudice, A.; Rizzo, A.; Biasiucci, M.; Gigli, G. *The Journal of Physical Chemistry Letters* **2012**, *3*, 1908.

(253) Aziz, E. F.; Vollmer, A.; Eisebitt, S.; Eberhardt, W.; Pingel, P.; Neher, D.; Koch, N. *Advanced Materials* **2007**, *19*, 3257.

(254) Duong, D. T.; Wang, C.; Antono, E.; Toney, M. F.; Salleo, A. *Organic Electronics* **2013**, *14*, 1330.

(255) Zhu, L.; Kim, E.-G.; Yi, Y.; Brédas, J.-L. *Chemistry of Materials* **2011**, *23*, 5149.

(256) Furukawa, Y. *The Journal of Physical Chemistry* **1996**, *100*, 15644.

(257) Łapkowski, M.; Proń, A. *Synthetic Metals* **2000**, *110*, 79.

(258) Casado, J.; Zgierski, M. Z.; Ewbank, P. C.; Burand, M. W.; Janzen, D. E.; Mann, K. R.; Pappenfus, T. M.; Berlin, A.; Pérez-Inestrosa, E.; Ortiz, R. P.; López Navarrete, J. T. *Journal of the American Chemical Society* **2006**, *128*, 10134.

(259) Louarn, G.; Trznadel, M.; Buisson, J. P.; Laska, J.; Pron, A.; Lapkowski, M.; Lefrant, S. *The Journal of Physical Chemistry* **1996**, *100*, 12532.

(260) Clark, J.; Chang, J.-F.; Spano, F. C.; Friend, R. H.; Silva, C. *Applied Physics Letters* **2009**, *94*.

(261) Busby, E.; Carroll, E. C.; Chinn, E. M.; Chang, L.; Moulé, A. J.; Larsen, D. S. *The Journal of Physical Chemistry Letters* **2011**, *2*, 2764.

(262) Furukawa, Y.; Akimoto, M.; Harada, I. *Synthetic Metals* **1987**, *18*, 151.

(263) Wise, A. J.; Grey, J. K. *Physical Chemistry Chemical Physics* **2012**, *14*, 11273.

(264) Myers, A. B. *Accounts of Chemical Research* **1997**, *30*, 519.

(265) Kleemann, H.; Schuenemann, C.; Zakhidov, A. A.; Riede, M.; Lüssem, B.; Leo, K. *Organic Electronics* **2012**, *13*, 58.

(266) Tsoi, W. C.; James, D. T.; Kim, J. S.; Nicholson, P. G.; Murphy, C. E.; Bradley, D. D. C.; Nelson, J.; Kim, J.-S. *Journal of the American Chemical Society* **2011**, *133*, 9834.

(267) Treat, N. D.; Brady, M. A.; Smith, G.; Toney, M. F.; Kramer, E. J.; Hawker, C. J.; Chabinyc, M. L. *Advanced Energy Materials* **2011**, *1*, 82.

(268) Tsoi, W. C.; Spencer, S. J.; Yang, L.; Ballantyne, A. M.; Nicholson, P. G.; Turnbull, A.; Shard, A. G.; Murphy, C. E.; Bradley, D. D. C.; Nelson, J.; Kim, J.-S. *Macromolecules* **2011**, *44*, 2944.

(269) Brédas, J. L.; Thémans, B.; Fripiat, J. G.; André, J. M.; Chance, R. R. *Physical Review B* **1984**, *29*, 6761.

(270) Lopez Navarrete, J. T.; Zerbi, G. *The Journal of Chemical Physics* **1991**, *94*, 965.

(271) Bredas, J. L.; Street, G. B. *Accounts of Chemical Research* **1985**, *18*, 309.

(272) Brédas, J. L.; Wudl, F.; Heeger, A. J. *Solid State Communications* **1987**, *63*, 577.

(273) Zhang, R.; Li, B.; Iovu, M. C.; Jeffries-El, M.; Sauvé, G.; Cooper, J.; Jia, S.; Tristram-Nagle, S.; Smilgies, D. M.; Lambeth, D. N.; McCullough, R. D.; Kowalewski, T. *Journal of the American Chemical Society* **2006**, *128*, 3480.

(274) Miller, J. S.; Krusic, P. J.; Dixon, D. A.; Reiff, W. M.; Zhang, J. H.; Anderson, E. C.; Epstein, A. J. *Journal of the American Chemical Society* **1986**, *108*, 4459.

(275) Niklas, J.; Mardis, K. L.; Banks, B. P.; Grooms, G. M.; Sperlich, A.; Dyakonov, V.; Beaupre, S.; Leclerc, M.; Xu, T.; Yu, L.; Poluektov, O. G. *Physical Chemistry Chemical Physics* **2013**, *15*, 9562.

(276) Park, Y. D.; Lee, S. G.; Lee, H. S.; Kwak, D.; Lee, D. H.; Cho, K. *Journal of Materials Chemistry* **2011**, *21*, 2338.

(277) Mouléé, A. J.; Meerholz, K. *Advanced Materials* **2008**, *20*, 240.

(278) Rainbolt, J. E.; Koech, P. K.; Polikarpov, E.; Swensen, J. S.; Cosimbescu, L.; Von Ruden, A.; Wang, L.; Sapochak, L. S.; Padmaperuma, A. B.; Gaspar, D. J. *Journal of Materials Chemistry C* **2013**, *1*, 1876.

(279) Galya, L. G.; McCord, E. F.; Adamsons, K. *International Journal of Polymer Analysis and Characterization* **1996**, *2*, 293.

(280) Panda, P.; Veldman, D.; Sweelssen, J.; Bastiaansen, J. J. A. M.; Langeveld-Voss, B. M. W.; Meskers, S. C. J. *The Journal of Physical Chemistry B* **2007**, *111*, 5076.

(281) Yong, C.; Renyuan, Q. *Solid State Communications* **1985**, *54*, 211.

(282) Cao, Y.; Guo, D.; Pang, M.; Qian, R. *Synthetic Metals* **1987**, *18*, 189.

(283) Kohji, T.; Yasuhisa, M.; Masamichi, K.; Shigenori, M.; Tsuyoshi, K.; Katsumi, Y. *Japanese Journal of Applied Physics* **1994**, *33*, L1023.

(284) Li, Y.; Qian, R. *Synthetic Metals* **1993**, *53*, 149.

(285) Elsenbaumer, R. L.; Jen, K. Y.; Miller, G. G.; Shacklette, L. W. *Synthetic Metals* **1987**, *18*, 277.

(286) Kanemoto, K.; Muramatsu, K.; Baba, M.; Yamauchi, J. *The Journal of Physical Chemistry B* **2008**, *112*, 10922.

(287) Kuzmany, H.; Stolz, H. J. *Journal of Physics C: Solid State Physics* **1977**, *10*, 2241.

(288) Jin Sun Kim, S. K. L., Ha Jin Lee, Dong Youn Noh *Bulletin of the Korean Chemical Society* **2010**, *31*, 4.

(289) Roncali, J. *Macromolecular Rapid Communications* **2007**, *28*, 1761.

(290) Marumoto, K.; Takeuchi, N.; Ozaki, T.; Kuroda, S. *Synthetic Metals* **2002**, *129*, 239.

(291) Österbacka, R.; An, C. P.; Jiang, X. M.; Vardeny, Z. V. *Science* **2000**, *287*, 839.

(292) Yu, Z.; Barbara, P. F. *The Journal of Physical Chemistry B* **2004**, *108*, 11321.

(293) Mirzov, O.; Cichos, F.; von Borczyskowski, C.; Scheblykin, I. *Journal of Luminescence* **2005**, *112*, 353.